Study on Half-Heusler Compounds for Thermoelectric Power Generation

---

A Dissertation Presented to

the Faculty of the Department of Physics and T_CSUH

University of Houston

In Partial Fulfillment

of the Requirements for the Degree

Doctor of Philosophy

By

Ran He

December 2016

Study on Half-Heusler Compounds for Thermoelectric Power Generation

Ran He

APPROVED:

Dr. Zhifeng Ren, Chairman
Department of Physics and T_CSUH

Dr. Wei-Kan Chu
Department of Physics and T_CSUH

Dr. Oomman Varghese
Department of Physics

Dr. Shuo Chen
Department of Physics

Dr. Kenneth White
Department of Mechanical Engineering

Dean, College of Natural Sciences and Mathematics

Acknowledgment

I never expected that I would want to write the acknowledgment section so eagerly until I finished the main manuscript of this dissertation. There are so many people I am obliged to, and the very first person I would like to thank is my advisor, Dr. Zhifeng Ren. He used to be, and will always be my idol. I feel extremely lucky of getting the chance to work with him. During my whole Ph.D. study, I learned substantially from him. Academically, many times I was tormented by the huge numbers of experimental data and complicated phenomena, but Dr. Ren could always grasp the key points and show me the right way to go. His way of thinking enlightened and equipped my mind to face any academic problems. Besides, Dr. Ren gave me more than academic capabilities. I am more aware of the meanings of confidence, enthusiasm, and responsibilities because of him. His noble characters are the lifelong gifts for me.

I would also like to express my sincere gratitude to the committee members, Dr. Zhifeng Ren, Dr. Shuo Chen, Dr. Wei-Kan Chu, Dr. Kenneth White, and Dr. Oomman Varghese, for all the questions and comments they proposed during my APE. They really helped me finding my blind spots and spurred me to think deeper and more thoroughly. It's my greatest honor to receive advice from these eminent scholars.

Many sincere thanks to my colleagues at UH. It's a really pleasure to work with these great people. I would like to thank Dr. Xiao Yan, Dr. Shuo Chen, Dr. Qing Jie, Dr. Dezhi Wang, Dr. Hee Seok Kim, Dr. Haiqing Zhou, Mr. Jun Mao, Ms. Sonika Gahlawat, Mr. Hui Wang, Ms. Jing Shuai, Mr. Zihang Liu, Dr. Yumei Wang, Dr. Qian Zhang, Dr.

Chuanfei Guo, Dr. Lihong Huang, Dr. Fang Yu, Dr. Weishu Liu, Dr. Hangtian Zhu, Dr. Tulashi Dahal, Dr. Eyob Chere, Mr. Keshab Dahal, Ms. Hao Zhang, and Ms. Yuan Liu. I benefited greatly from all the fruitful discussions with them.

Especially I would like to thank Dr. Xiao Yan, Dr. Qing Jie, Mr. Hui Wang and Dr. Dezhi Wang for teaching me the usage of the experimental devices.

Also, I would like to thank Dr. Daniel Kraemer and Dr. Lingping Zeng at MIT, Dr. Chunhua Li at UH, and Dr. Georgy Samsonidze at Bosch for their contributions in my work. Their specialties helped to expand my research to new dimensions.

Many thanks to Dr. Gang Chen at MIT, Dr. Yucheng Lan at Morgen State University, Dr. David Broido at Boston College and Dr. Qinyong Zhang at Xihua University for sharing their novel ideas on my work, as well as their generous assistance to revise my manuscripts.

I would also like to thank all my friends for accompanying me in all the years. All the happy hours we spent together will become cherishing memories.

Finally, I would like to thank my family. I feel warm inside when I think of them. The telephone calls and video chats with them accompanied me in many tough nights. I love them forever.

Ran He

Dec. 2016

Study on Half-Heusler Compounds for Thermoelectric Power Generation

---

An Abstract of Dissertation

Presented to

the Faculty of the Department of Physics and T_CSUH

University of Houston

In Partial Fulfillment

of the Requirements for the Degree

Doctor of Philosophy

By

Ran He

December 2016

Abstract

Thermoelectric (TE) technique is unique in heat-to-power conversion due to its solid and non-moving nature. The efficiency of thermoelectric devices is related to the dimensionless figure-of-merit (*ZT*) of the material, defined as $ZT = \frac{S^2\sigma}{\kappa}T$, where *S, σ, κ,* and *T* are the Seebeck-coefficient, electrical conductivity, thermal conductivity, and absolute temperature, respectively, and the term $S^2\sigma$ is called the power factor. The design of TE devices for power generation applications requires the knowledge of the mechanical properties of TE materials due to the externally loaded mechanical and thermal stresses. Therefore, this nanoindentation technique was adopted to test the mechanical properties of various TE materials applied in a moderate-temperature range (200-700 °C). The results show the half-Heusler (HH) compounds are more mechanically robust as compared with other materials and favorable for applications. However, the usage of hafnium (Hf) in the HH compounds is unfavorable for applications due to its ultrahigh price. Therefore, the TE performances of p-type HH compounds were investigated with decreased Hf usage. The optimized new compound ($Hf_{0.19}Zr_{0.76}Ti_{0.05}CoSb_{0.8}Sn_{0.2}$) has *ZT* values similar to the previously reported best composition ($Hf_{0.44}Zr_{0.44}Ti_{0.12}CoSb_{0.8}Sn_{0.2}$). But the specific power cost ($\$ W^{-1}$) of the new compound is much lower due to the suppressed usage of Hf. Similar suppressing of power cost was also obtained in the NbCoSn-based n-type HH compounds through the elimination of Hf usage. Furthermore, the study of TE performances of the NbFeSb-based p-type HH, another Hf-free compound, resulted in an extremely high power factor of ~106 μW cm^{-1} K^{-2} in $Nb_{0.95}Ti_{0.05}FeSb$ due to the improved carrier mobility. This is the highest power factor among the semiconductor thermoelectric

materials above room temperature. Subsequently, a single-leg device based on the high-power-factor material yielded a record output-power density of ~22 W cm^{-2} operating at between 293 and 868 K. Such a high output-power density greatly facilitates the large-scale power generation applications.

Contents

List of Publications

[18] **Ran He**, Daniel Kraemer, Jun Mao, Lingping Zeng, Qing Jie, Yucheng Lan, Chunhua Li, Jing Shuai, Hee Seok Kim, Yuan Liu, David Broido, Ching-Wu Chu, Gang Chen, and Zhifeng Ren, *PNAS*, doi: 10.1073/pnas.1617663113 (2016).

[17] Haiqing Zhou, Fang Yu, Yufeng Huang, Jingying Sun, Zhuan Zhu, Robert J Nielsen, **Ran He**, Jiming Bao, William A Goddard III, Shuo Chen and Zhifeng Ren, *Nature Communications* **7**, 12765 (2016).

[16] **Ran He**, Lihong Huang, Yumei Wang, Georgy Samsonidze, Boris Kozinsky, Qinyong Zhang and Zhifeng Ren, *APL materials* **4**, 104804 (2016).

[15] Aijun Hong, Lin Li, **Ran He**, Jijun Gong, Zhibo Yan, Kefeng Wang, Juming Liu and Zhifeng Ren, *Scientific Reports* doi:10.1038/srep22778 (2016).

[14] Qian Zhang, Eyob Chere, Yumei Wang, Hee Seok Kim, **Ran He**, Feng Cao, Keshab Dahal, David Broido, Gang Chen and Zhifeng Ren, *Nano Energy* **22**, 572-582 (2016).

[13] Jing Shuai, Hee Seok Kim, Zihang Liu, **Ran He**, Jiehe Sui and Zhifeng Ren, *Applied Physics Letters* **108**, 183901 (2016).

[12] Jing Shuai, Zihang Liu, Hee Seook Kim, Yumei Wang, Jun Mao, **Ran He**, Jiehe Sui and Zhifeng Ren, *Journal of Materials Chemistry A* **4**, 4312-4320 (2016).

[11] Haiqing Zhou, Fang Yu, Jingying Sun, **Ran He**, Yumei Wang, Chuan Fei Guo, Feng Wang, Yucheng Lan, Zhifeng Ren and Shuo Chen, *Journal of Materials Chemistry A* **4**, 9472-9476 (2016).

[10] Zihang Liu, Yumei Wang, Jun Mao, Huiyuan Geng, Jing Shuai, Yumei Wang, **Ran He**, Wen Cai, Jiehe Sui and Zhifeng Ren, *Advanced Energy Materials* **6**, 1502269 (2016).

[9] Jun Mao, Hee Seok Kim, Jing Shuai, Zihang Liu, **Ran He**, Udara Saparamadu, Fei Tian, Weishu Liu and Zhifeng Ren, *Acta Materialia* **103**, 633-642 (2016).

[8] Haiqing Zhou, Yumei Wang, **Ran He**, Fang Yu, Jingying Sun, Feng Wang, Yucheng Lan, Zhifeng Ren and Shuo Chen, *Nano Energy* **20**, 29-36 (2016).

[7] **Ran He**, Sonika Gahlawat, Chuanfei Guo, Shuo Chen, Tulashi Dahal, Hao Zhang, Weishu Liu, Qian Zhang, Eyob Chere, Kenneth White, and Zhifeng Ren, *Physics Status Solidi A* **212**, 2191-2195 (2016).

[6] Jiehe Sui, Jing Shuai, Yucheng Lan, Yuan Liu, **Ran He**, Dezhi Wang, Qing Jie, and Zhifeng Ren, *Acta Materialia* **87**, 266-272 (2015).

[5] Lihong Huang, **Ran He**, Shuo Chen, Hao Zhang, Keshab Dahal, Haiqing Zhou, Hui Wang, Qinyong Zhang, and Zhifeng Ren, *Materials Research Bulletin* **70**, 773-778 (2015).

[4] Zihang Liu, Jing Shuai, Huiyuan Geng, Jun Mao, Yan Feng, Xu Zhao, Xianfu Meng, **Ran He**, Wei Cai and Jiehe Sui, *ACS applied materials & interfaces* **7**, 23047-23055 (2015).

[3] **Ran He**, Hee Seok Kim, Yucheng Lan, Dezhi Wang, Shuo Chen, and Zhifeng Ren, *RSC Advanced* **4**, 64711-64716 (2014).

[2] Sonika Gahlawat, **Ran He**, Shuo Chen, L. Wheeler, Zhifeng Ren, and Kenneth W. White, *Journal of Applied Physics* **116**, 083516 (2014).

[1] Giri Joshi, **Ran He**, Michael Engber, Georgy Samsonidze, Tej Pantha, Ekraj Dahal, Keshab Dahal, Jian Yang, Yucheng Lan, Boris Kozinsky, and Zhifeng Ren, *Energy and Environmental Science* **7**, 4070-4076 (2014).

List of Figures

Chapter 1 Introduction and Theory of Thermoelectrics

1.1 Introduction

The majority of the energy consumption generated by burning fossil fuels (coal, oil, gas, etc.) are dissipated as wasted heat. In addition, the increased emission of carbon-dioxide intensifies the greenhouse effects. Therefore, converting parts of the waste-heat into useful electricity not only increases the energy usage efficiency, but also alleviates the environmental impact.

There are several existing systems that fulfil this purpose. For example the binary cycle systems utilizing organic fluids [1-2]; the thermo-electro-chemical systems that utilizing thermogalvanic effects [3-4]; the thermo-osmotic vapor transport through hydrophobic nanoporous membranes [5].

In comparison, the thermoelectric (TE) technique is unique in heat-to-power conversion due to its solid nature. The TE effects are the coupled transport of phonons and electrons. Historically, the first TE effect, now known as the Seebeck effect, was observed by Thomas Johann Seebeck in 1821 [6]. In the following three decades the TE field has developed extensively with more insights into the fundamentals, as well as the discovery of many new phenomena, such as the Peltier effect and the Thomson effect [7, 8]. In the early 1910s Altenkirch firstly derived the maximum efficiency of a TE generator and cooling performance of a Peltier cooler, and introduced the concept of the figure-of-merit, *ZT* [9]. However, subsequent investigations dimmed since the thermopower (*i.e.* the Seebeck-coefficient) in metals are too low to make applicable TE generators. It was not until the late 1940s through 1970s, the TE field began receiving augmented study after

Ioffe's development of the modern theory for semiconductors that identified semiconductors as more promising TE materials than metals [10]. In addition, NASA was also actively involved in TE study at that time in order to power their space probes. Many important progresses were made, such as the establishing of modern theory of thermoelectricity [10], the first TE generator, and the radioisotope thermoelectric generator (RTG) for space probes. However, the low conversation efficiency (for example, 3-7% of RTG) and high cost of the TE technique hindered its applications in other fields, and no significant improvement was achieved in the 1980s.

During the 1990s, the intensified global energy crisis and environmental issues urged the research of novel and clean energy sources. Thus, the TE technique experienced a rebirth due to its potential in improving the energy usage efficiency and decreasing the emission of carbon-dioxide. Furthermore, the study of TE materials was also encouraged by the theoretical predictions that TE efficiency could be enhanced significantly in nanostructured materials [11, 12]. It was predicted that, in comparison to the bulk TE material, nanostructured TE materials would have higher power factors ($S^2\sigma$) if the quantum-confinement effects could be properly introduced [13]. In addition, the heat transport could be suppressed if the size of the materials is comparable or shorter than the phonon mean-free-path (MFP) [14]. These predictions were later demonstrated experimentally, where the ZT improved significantly in the Bi_2Te_3/Sb_2Te_3 superlattices and PbTe/PbSeTe quantum dot superlattices [15, 16].

However, the synthesis of low-dimensional materials are usually expensive, and it's also difficult to obtain in high yields. Therefore, the TE community also focused on

developing novel bulk TE materials, such as skutterudites [17], zintl phases [18], and clathrates [19]. These materials possess large unit cells or complex crystal structures that can suppress the phonon-thermal conductivity and enhance the heat-to-power conversion efficiency. For example, the unit cells of the skutterudites have large lattice constant (~10 Å), which suppresses the thermal conductivity, and also possesses positions that can be easily occupied by "fillers" elements. The fillers serve as dopants to optimize the carrier concentration, and also rattle inside the unit cells, thus impeding heat transport and suppressing thermal conductivity.

Indeed, the development of novel bulk TE materials obtained several successes [20, 21], and better TE properties were expected if they could be combined with the nanostructure concept in a more economical and practical way. It was further pointed out that for reducing the thermal conductivity, superlattice structure is not rigidly required as long as the interfaces densities are high enough inside the samples [22]. This idea was subsequently realized by our group using high-energy ball-milling following a sintering process to build the nanostructured bulk samples. This approach works very well for many TE materials including but not limited to Bi_2Te_3 [23], IV-VI semiconductor compounds [24-26], skutterudites [27, 28], $CuSe_2$ [29], Zintl phases [30], half-Heuslers [31-33], MgAgSb [34], and Mg_2(Si, Ge, Sn) [35]. As one example, a peak ZT of ~1.4 was reported for the nanostructured p-type $Bi_{0.4}Sb_{1.6}Te_3$ [23]. This shows an enhancement of ~40% in comparison to its bulk counterpart. Importantly, all the techniques in this approach are industrially well-established and thus a large yield of the TE materials is possible.

In this chapter, I will briefly review the TE phenomena, the transport properties, current challenges in improving the properties, and my approach to boost the TE performances.

1.2 Fundamentals of thermoelectric effects

Thermoelectric effects are the coupled transport of electrons and phonons. Generally, the Fermi distribution function varies with temperature and the Fermi level. Thus, the carriers will "flow" inside the material to satisfy the thermodynamic balance once a temperature gradient or a voltage drop is applied across the material. These effects could potentially be applied for power generation or temperature-control purposes.

1.2.1 Thermoelectric effects

1.2.1.1 Seebeck effect

As shown in Figure 1.1, when two different metals (for example, Cu and Fe) are connected with the two junctions at different temperatures, a voltage difference appears. This was first discovered by Thomas Johann Seebeck in 1821, thus the phenomena is called the Seebeck effect.

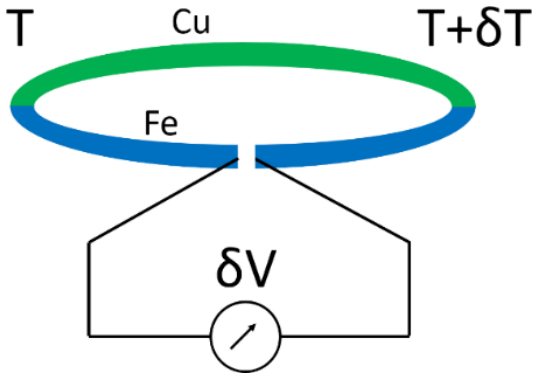

Figure 1.1 Schematic diagram of the Seebeck effect.

The Seebeck effect is the working principle of thermocouple. However, the paired wires are not necessary to observe the Seebeck effect since it is an intrinsic property for any material. In the classical view, the temperature gradient breaks the thermodynamic balance inside the material and drives the charge carriers to "diffuse" from the hot side to the cold side and form a continuous current if the circuit is closed. A more accurate picture is given by modern solid-state physics, where the Fermi-Dirac distribution function varies as the temperature change. It yields a re-distribution of charge carriers across TE legs, which drives the formation of current.

The Seebeck effect is characterized by the Seebeck-coefficient (S). With the temperature difference δT across a material and yielding a voltage drop δV along the same direction of temperature drop, the Seebeck-coefficient is expressed as

$$S(T) = -\frac{\delta V}{\delta T} \tag{1.1}$$

For semiconductors, the sign of the Seebeck-coefficient depends on the dominate carrier type: it is positive for holes and negative for electrons. The Seebeck-coefficient is also named thermopower and is represented by the symbol "α" in some reports.

1.2.1.2 Peltier effect

The Peltier effect was discovered in 1834 by a French physicist Jean Charles Athanase Peltier. It is the reverse of the Seebeck effect that depicting the occurrence of heating or cooling when an external current passes across a junction between two materials. The Peltier coefficient (Π_{ab}) of a pair of materials (material a and material b) at a junction is defined as the heat-flux density (q) divided by the applied current density (j)

$$\Pi_{ab} = \Pi_a - \Pi_b = \frac{q}{j} \tag{1.2}$$

where Π_a (Π_b) is the Peltier coefficient of the material a (b). From a solid-state physics view, the chemical potential become position-dependent under the applied voltage, which drives the charge carriers to "flow" from the high-chemical-potential side to the low-chemical-potential side. This process automatically transfers thermal energy along the material. Therefore, one side of the material will be cooled and the other side will be heated. A schematic diagram of the Peltier effects is shown in Figure 1.2. Note that the Peltier effect generates only a portion of the total heat, and other effects such as Joule heating and Thomson effect are also related to heat generation (see below).

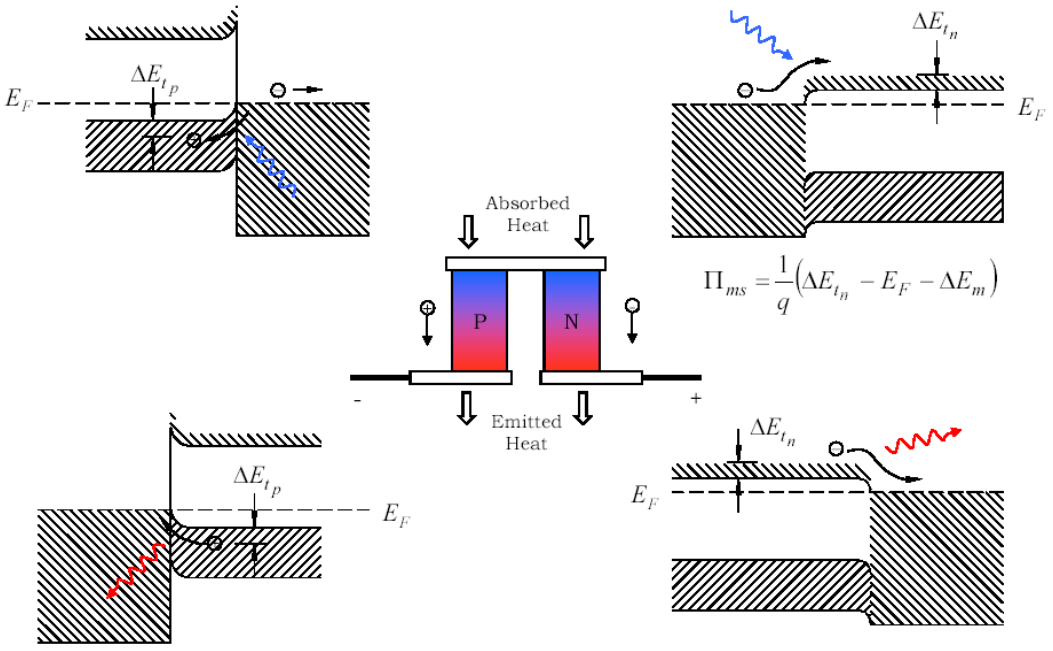

Figure 1.2 A schematic diagram of the Peltier effects (Presentation at DTEC by T. Hogan, Michigan State University).

1.2.1.3 Thomson effect

The Thomson effect was firstly discovered by William Thomson (Lord Kelvin) in 1851. It describes the heating or cooling of a conductor that simultaneously possess a current and a temperature difference. The heat-flux density (q) is given as (assuming one-dimensional transport)

$$q = -\beta j \frac{dT}{dx} \tag{1.3}$$

where β and j are the Thomson coefficient and current density, respectively.

1.2.1.4 The Kelvin's relation

The three effects introduced above are interconnected with each other through the Kelvin's relation.

$$\beta \equiv \frac{d\Pi}{dT} - S \tag{1.4}$$

$$\Pi = ST \tag{1.5}$$

Eq. (1.4) and Eq. (1.5) are named as the first and second Kelvin's relation, respectively. The derivation of the Kelvin's relation requires knowledge of fundamental thermodynamics and will be given in section 1.2.4.

1.2.1.5 Thermoelectric devices

The thermoelectric device can be designed for applications such as power generation or temperature control, depending on whether the Seebeck effect or the Peltier effect is exploited. The building block of thermoelectric devices is the uni-couple, formed by connecting one n-type and one p-type leg in series, as shown in Figure 1.3. One uni-couple device usually generates only a small voltage, thus in real applications multiple uni-couples are assembled in series to increase the electromotive force (emf).

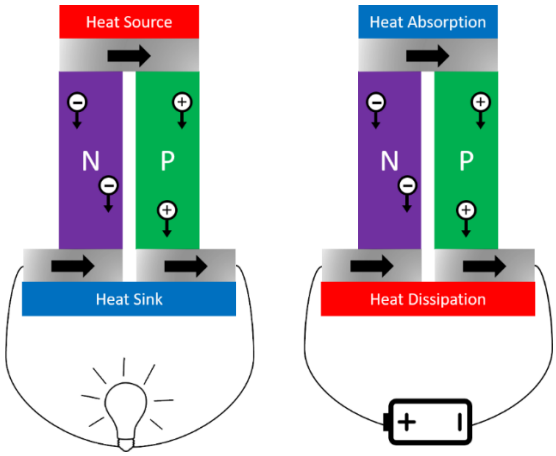

Figure 1.3 Schematic of a thermoelectric generator (left) and cooler (right).

For TE devices, the highest heat-to-power conversion efficiency is ~10%, which is not enough for use in large-scale power generation. The thermoelectric performance is governed by the dimensionless quantity, the figure-of-merit (ZT). Successful improvement of ZT could accelerate the large-scale application of the thermoelectric technique. The detailed introduction to ZT is given section 1.2.2.

1.2.2 Thermoelectric parameters

The dimensionless figure-of-merit (ZT) is the core parameter for characterizing the performance of a thermoelectric material. It is defined as

$$ZT = \frac{S^2\sigma}{\kappa}T \tag{1.6}$$

$$\kappa = \kappa_e + \kappa_L \tag{1.7}$$

where S, σ, κ, κ_e, κ_L and T are the Seebeck-coefficient, the electrical conductivity, the thermal conductivity, the electronic thermal conductivity, the lattice thermal conductivity and the absolute temperature, respectively. The term $S^2\sigma$ is called the power factor, which

governs the maximum output-power density. Higher *ZT* corresponds to higher conversion efficiency. Thus, good thermoelectric material needs to have high Seebeck-coefficient, high electrical conductivity, and low thermal conductivity. Unfortunately, it's very difficult to improve the three parameters simultaneously since they are related to each other, as will be introduced in the section below.

1.2.2.1 Conflicting thermoelectric properties

It's extremely difficult to simultaneously improve all the TE parameters due to intrinsic conflicts. A good example to show the conflicts of the TE parameters is through the *carrier concentration* (*n*). The electrical conductivity is a multiplication of electron charge (*e*, positive), carrier concentration (*n*), and carrier mobility (μ)

$$\sigma = ne\mu \tag{1.8}$$

With the single parabolic band (SPB) assumption and energy-independent scattering approximation [36], the Seebeck-coefficient satisfies the Pisarenko relation [37]

$$S = \frac{8\pi k_B^2}{3eh^2} m^* T \left(\frac{\pi}{3n}\right)^{\frac{2}{3}} \tag{1.9}$$

where k_B, h, and m^* are the Boltzmann constant, the Planck constant, and the density-of-states (DOS) effective mass, respectively.

The electronic thermal conductivity is also related to the carrier concentration through the electric conductivity

$$\kappa_e = L\sigma T \tag{1.10}$$

where L is the Lorenz number, which is ~2.4×10^{-8} W Ω K^{-2} for metals. Eq. (1.10) is named the *Wiedemann-Franz law* [38].

The conflicting thermoelectric properties are clearly shown in Figure 1.4. Metals possess high conductivity and a low Seebeck-coefficient, while insulators have a high Seebeck-coefficient and a low conductivity, as a result of the carrier concentration difference. Thus, both metals and insulators are usually not suitable for thermoelectric applications since their ZT are too low. The carrier concentration of good thermoelectric materials usually locates in the order of 10^{19}~10^{21} cm^{-3}. This is usually the range of heavily doped semiconductors.

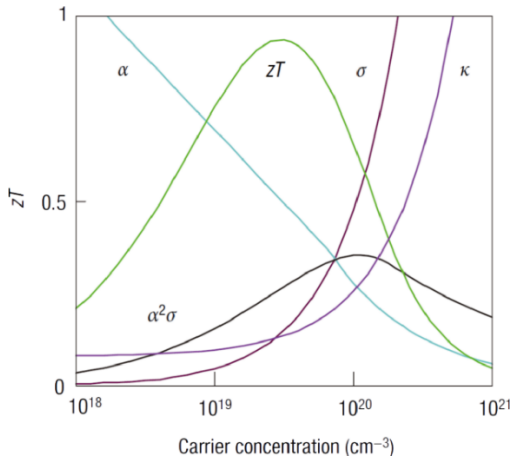

Figure 1.4 Optimizing ZT through carrier concentration tuning [39]. Here the Seebeck-coefficient is denoted as α.

Another example that shows the conflict is from the **effective mass**. As shown in Eq. (1.9), higher effective mass benefits the Seebeck-coefficient (S). Meanwhile, it also yields lower carrier mobility (μ) if there is no band-convergence. For real materials, however, there is no optimal combination range for the mobility and effective mass. Good

*ZT*s were reported in materials with low mobility and high effective mass (half-Heuslers [40], *etc.*), as well as with high mobility and low effective mass (InSb [41], *etc*.).

1.2.2.2 Lattice thermal conductivity

All the conflicting parameters are related to the electron transport. On the other hand, the lattice thermal conductivity is related to phonon transport and does not have direct relations with the rest parameters. Therefore, it has been actively investigated to suppress the lattice thermal conductivity.

The lattice thermal conductivity derived from the Boltzmann equation has a general expression:

$$\kappa_L = \frac{1}{3} c_v v_s l \tag{1.11}$$

where c_v, v_s, and l are the specific heat at constant volume, the average velocity, and the mean-free-path of phonons, respectively. Clearly it's necessary to shorten the phonon mean-free-path to obtain lower lattice thermal conductivity. This was realized by the nanostructuring approach developed in our group. For a more detailed analysis, I will introduce the Klemens model in chapter 6 to study the lattice thermal conductivity under different scattering mechanisms in NbFeSb-based half-Heusler.

1.2.2.3 High *ZT* materials

Depending on the temperature where the peak *ZT* appears, thermoelectric (TE) materials could be roughly divided into three groups: low-temperature TE material (300 K to 500 K), mid-temperature TE material (500 K to 900 K), and high-temperature TE

material (>900K). Figure 1.5 shows the figure-of-merit of some of the state-of-the-art thermoelectric materials.

The Bismuth telluride (Bi_2Te_3) based alloys are the most famous low-temperature TE material. These alloys have very high *ZT* from 300 to 500 K, and already been commercialized for power generation and cooling for decades. Another promising low-temperature TE material is the MgAgSb alloy that have comparable *ZT* with the Bi_2Te_3 based alloys.

There are several promising mid-temperature thermoelectric materials, such as the skutterudites, the lead telluride (PbTe), and the magnesium-stannide (Mg_2Sn) compounds. Recently the SnSe single crystal, and several Zintl phases are also reported as promising mid-temperature materials. In comparison, the skutterudites compounds, the Mg_2Sn compounds and Zintl phases are particularly attractive since the other compounds are not favorable for applications: the PbTe compounds use toxic element (Pb), and the SnSe compounds are mechanically fragile.

For high-temperature power generation, the silicon-germanium alloys were used back to 1950s by NASA for space programs, and is still under active investigation now. Another promising high-temperature TE materials are the half-Heusler compounds due to their superior thermal and mechanical stability and high power factors.

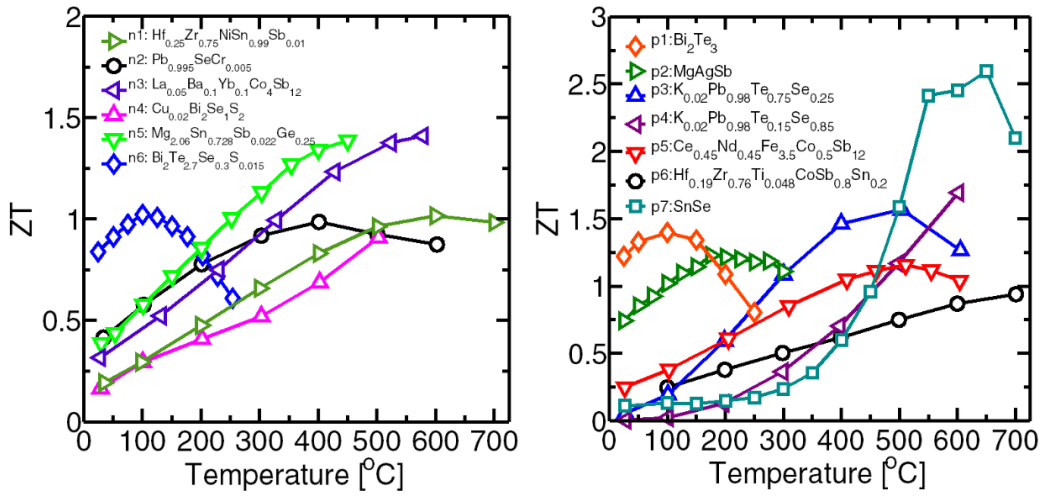

Figure 1.5 State-of-the-art high ZT in some of the n-type and p-type materials. Figure courtesy of Dr. Hee Seok Kim, post-doctoral fellow in Prof. Zhifeng Ren's lab.

1.2.3 Thermoelectric device performance

1.2.3.1 Power generation

The conversion efficiency of a generator is the ratio of the energy generated, to the heat absorbed at the hot-junction. As analyzed by Ioffe [10], the conversion efficiency (η) from heat to power is

$$\eta = \frac{T_H - T_C}{T_H} \cdot \frac{\sqrt{1+\overline{ZT}}-1}{\sqrt{1+\overline{ZT}}+\frac{T_C}{T_H}} \qquad (1.12)$$

where T_C and T_H are the cold-side and hot-side temperatures, respectively. The $\overline{ZT}$ is the average ZT between the hot-side and cold-side. The term $(T_H\text{-}T_C)/T_H$ is the Carnot efficiency of an ideal heat engine. The relation between the average ZT and the conversion efficiency is schematically plotted in Figure 1.6. Clearly, higher ZT yields higher conversion efficiency. When $ZT \to \infty$, $\eta \to$ the Carnot efficiency.

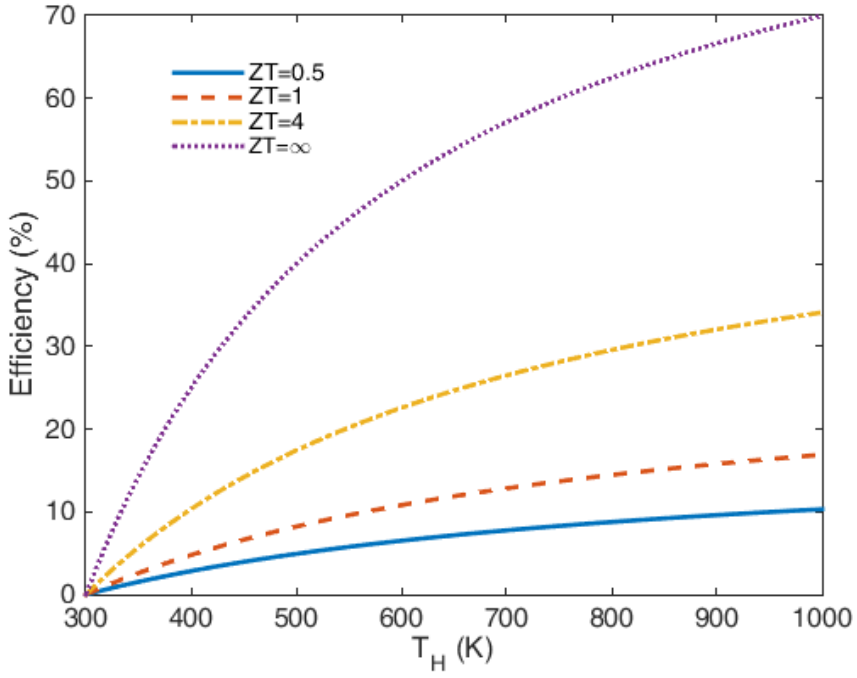

Figure 1.6 Power generation efficiency of single-leg device as function of hot side temperature T_H with an assumption of T_C=300 K.

1.2.3.2 Cooling

The cooling efficiency of a TE device is characterized by the coefficient of performance (COP). The COP is defined as the amount of heat pumping divided by the amount of supplied electrical power. The maximum COP for an ideal TE device is given by

$$COP_{max} = \frac{T_C}{T_H - T_C} \frac{\sqrt{1+\overline{ZT}} - \frac{T_H}{T_C}}{\sqrt{1+\overline{ZT}}+1} \tag{1.13}$$

Higher ZT gives higher COP.

1.2.4 Thermoelectric transport theory

Firstly, we discuss the presence of electric field (ε) only. Considering one-dimensional transport along the *x*-direction. The distribution function of electrons under relaxation time approximation is [42],

$$f = f_0 - \tau(v_x \frac{\partial f_0}{\partial x} - \frac{e\varepsilon}{m}\frac{\partial f_0}{\partial v_x}) \tag{1.14}$$

We set the electron charge as $-e$, thus e is positive. The quantities τ, v_x, and m are the relaxation-time, speed, and mass of electron, respectively. The term f_0 is the equilibrium Fermi-Dirac distribution function

$$f_0 = \frac{1}{exp\left(\frac{E-\varphi}{k_B T}\right)+1} \tag{1.15}$$

where E, φ, k_B, and T are the electron energy, the Fermi level, the Boltzmann constant, and the absolute temperature, respectively. For semiconductors, if the band-edge energy (E_C) were picked as the reference energy, then the energy of electrons (E) are spatially invariant. This gives us

$$\varepsilon = -\frac{d(-E_C/e)}{dx} \tag{1.16}$$

$$\frac{\partial f_0}{\partial x} = \frac{\partial f_0}{\partial \varphi}\frac{d\varphi}{dx} = -\frac{\partial f_0}{\partial E}\frac{d\varphi}{dx} \tag{1.17}$$

and Eq. (1.14) becomes

$$f = f_0 + \tau\left(v_x \frac{\partial f_0}{\partial E}\frac{d\varphi}{dx} + \frac{e\varepsilon}{m}\frac{\partial f_0}{\partial E}\frac{\partial E}{\partial v_x}\right) = f_0 + \tau v_x \frac{\partial f_0}{\partial E}(\frac{d\varphi}{dx} + e\varepsilon) \tag{1.18}$$

In Eq. (1.18), I used the relation $E = (1/2)mv_x^2$. Therefore, the current density (j) is

$$j = -\frac{2}{(2\pi)^3}\int_{-\infty}^{\infty}\int_{-\infty}^{\infty}\int_{-\infty}^{\infty} ev_x f\, dk_x dk_y dk_z$$

$$= -\frac{e}{4\pi}\oint_0^{4\pi}\left\{\int_0^{\infty} v_x^2\tau\left(\frac{d\varphi}{dx} + e\varepsilon\right)\frac{\partial f_0}{\partial E}D(E)dE\right\}d\Omega$$

$$= -\frac{e}{3}\left(\frac{d\varphi}{dx} + e\varepsilon\right)\int_0^{\infty}\tau v^2 D(E)\frac{\partial f_0}{\partial E}dE$$

$$= \frac{d\Phi}{dx}\frac{e^2}{3}\int_0^{\infty}\tau v^2 D(E)\frac{\partial f_0}{\partial E}dE \approx -\frac{e^2}{3}\varepsilon\int_0^{\infty}\tau v^2 D(E)\frac{\partial f_0}{\partial E}dE \qquad (1.19)$$

Here, Φ is the *electrochemical-potential* which has a dimension of energy divided by charge. Using Eq. (1.16), we have

$$\Phi = -(E_C + \varphi)/e \qquad (1.20)$$

The final step in Eq. (1.19) is approximated since the spatial variation of the chemical potential ($\frac{d\varphi}{dx}$) is usually small. This is indeed the case for metals and degenerate semiconductors that have very high carrier concentrations.

Eq. (1.19) could be further written as

$$j = \sigma\left(-\frac{d\Phi}{dx}\right) \approx \sigma\varepsilon \qquad (1.21)$$

Eq. (1.21) is Ohm's law and σ is the *electrical conductivity*

$$\sigma = -\frac{e^2}{3}\int_0^{\infty}\tau v^2 D(E)\frac{\partial f_0}{\partial E}dE = L_{11} \qquad (1.22)$$

where L_{11} is a notation will be used later.

Now, let's superimpose a temperature gradient on the electric field. In this case, both the Fermi level and the temperature varies with location, and $\partial f_0/\partial x$ is written as

$$\frac{\partial f_0}{\partial x} = -\frac{\partial f_0}{\partial E}\frac{d\varphi}{dx} - \frac{E-\varphi}{T}\frac{\partial f_0}{\partial E}\frac{dT}{dx} \tag{1.23}$$

Substituting Eq. (1.23) into Eq. (1.14), then following the same routine as in Eq. (1.19), we have

$$j = -\frac{e}{3}\int_0^\infty \tau v^2 \left(\frac{d\varphi}{dx} + e\varepsilon + \frac{E-\varphi}{T}\frac{dT}{dx}\right) D(E)\frac{\partial f_0}{\partial E}dE \tag{1.24}$$

or

$$j = L_{11}\left(-\frac{d\Phi}{dx}\right) + L_{12}\left(-\frac{dT}{dx}\right) \tag{1.25}$$

The first term in Eq. (1.25) is exactly Eq. (1.21). The second term describes the current under the temperature gradient

$$L_{12} = \frac{e}{3T}\int v^2\tau(E-\varphi)D(E)\frac{\partial f_0}{\partial E}dE \tag{1.26}$$

With an open circuit (j=0), Eq. (1.25) gives

$$\frac{L_{12}}{L_{11}} = \left(-\frac{d\Phi}{dx}\right)\Big/\left(\frac{dT}{dx}\right) \tag{1.27}$$

Comparing with Eq. (1.1), Eq. (1.27) defines the *Seebeck-coefficient* from the thermodynamic view

$$S = \frac{L_{12}}{L_{11}} = -\frac{d\Phi}{dT} = -\frac{1}{eT}\frac{\int v^2\tau(E-\varphi)D(E)\frac{\partial f_0}{\partial E}dE}{\int v^2\tau D(E)\frac{\partial f_0}{\partial E}dE} \tag{1.28}$$

Now, let's examine the heat-flux under the coexisting temperature and voltage gradient. Note that the heat-flux is only a portion of the total energy-flux since we are

dealing with an open system with particle-flux. Applying the *first law of thermodynamics* to a fixed differential volume

$$dU = dQ + \varphi dN \tag{1.29}$$

Then, the heat-flux (q), energy-flux (j_E), and particle-flux (j_N) satisfy

$$dq = dj_E - \varphi dj_N \tag{1.30}$$

Considering one-dimensional flow along x-direction, these fluxes can be written as

$$j_E = \int E v_x f dv_x dv_y dv_z \text{ and } j_N = \int v_x f dv_x dv_y dv_z \tag{1.31}$$

therefore, the heat-flux along the x-direction is

$$q = \int (E - \varphi) v_x f dv_x dv_y dv_z \tag{1.32}$$

Using Eq. (1.14) and Eq. (1.23) and following the same procedure in deriving the current density, we obtain the expression for heat-flux,

$$q = L_{21}\left(-\frac{d\Phi}{dx}\right) + L_{22}\left(-\frac{dT}{dx}\right) \tag{1.33}$$

The first term is the energy carried due to the convection of electrons under an electrochemical-potential gradient, the second term is due to the diffusion of electrons under a temperature gradient. The expressions for the two coefficients are

$$L_{21} = \frac{e}{3}\int v^2 \tau (E - \varphi) D(E) \frac{\partial f_0}{\partial E} dE = T L_{12} \tag{1.34}$$

$$L_{22} = -\frac{1}{3T}\int v^2 \tau (E - \varphi)^2 D(E) \frac{\partial f_0}{\partial E} dE \tag{1.35}$$

Eliminating the factor $\frac{d\Phi}{dx}$ using Eq. (1.25) and Eq. (1.33), we get

$$q = \frac{L_{21}}{L_{11}} j + \left(L_{22} - \frac{L_{21}L_{12}}{L_{11}}\right)\left(-\frac{dT}{dx}\right) = \Pi j - \kappa_e \frac{dT}{dx} \tag{1.36}$$

where

$$\Pi = \frac{L_{21}}{L_{11}} = TS \tag{1.37}$$

$$\kappa_e = L_{22} - \frac{L_{21}L_{12}}{L_{11}} \tag{1.38}$$

Π is the *Peltier coefficient* introduced above, and κ_e is the *electronic thermal conductivity*. Eq. (1.37) is the *second Kelvin relation*, same as Eq. (1.5).

However, Eq. (1.36) is not complete for thermal transport since heat can be carried by phonons also. Therefore, the quantity κ_e should be replaced by κ, the total thermal conductivity, to describe the complete heat-flux density. By doing so, we get a pair of equations

$$q = -(\kappa + \Pi S\sigma)\frac{dT}{dx} - \Pi\sigma\frac{d\Phi}{dx} \tag{1.39a}$$

$$j = -S\sigma\frac{dT}{dx} - \sigma\frac{d\Phi}{dx} \tag{1.39b}$$

The two equations clearly show the coupled transport of heat and charge carriers under a temperature gradient ($\frac{dT}{dx}$) and an electrochemical potential gradient ($\frac{d\Phi}{dx}$).

Eliminating the factor $\frac{d\varphi}{dx}$ between Eq. (1.39a) and Eq. (1.39b) produces

$$q = -\kappa\frac{dT}{dx} + \Pi j \tag{1.40}$$

Note that if there is no current (j=0), Eq. (1.40) is just the Fourier's law of heat conduction.

Considering a differential volume, inside which the total energy-flux (j_E) constitutes of two parts. One from the thermal heat-flux (q) and the other from the energy carried by the electrons ($j\Phi$). If the energy-flux is constant across the material, then the amount of energy flowing into any differential volume (dx in one-dimension) equals the energy flowing out. Otherwise it gains net energy accumulation $\dot{e}$ per unit volume:

$$\dot{e} = -\frac{dj_E}{dx} = -\frac{dq}{dx} - j\frac{d\Phi}{dx} \tag{1.41}$$

Here, a constant electric current is assumed. Substituting Eq. (1.39b) and Eq. (1.40) into Eq. (1.41) to eliminate q and $\frac{d\varphi}{dx}$, it gives

$$\dot{e} = \frac{d}{dx}\left(\kappa\frac{dT}{dx}\right) + \frac{j^2}{\sigma} - \left(\frac{d\Pi}{dT} - S\right)\frac{dT}{dx}j \tag{1.42}$$

The first and the second term in Eq. (1.42) are due to heat conduction and Joule heating, respectively. The third term is the Thomson effect, from which the Thomson coefficient (β) is defined when comparing with Eq. (1.3)

$$\beta \equiv \frac{d\Pi}{dT} - S \tag{1.43}$$

Eq. (1.43) is the *first Kelvin's relation*, as already shown in Eq. (1.4).

1.3 Nanoindentation

Indentation test was initially introduced to define the Mohs' hardness. If one material is able to leave a permanent scratch in another, it was ranked as the harder material. Diamond has the maximum hardness value of 10 in the Mohs' scale. This technique was then refined to different versions including the Brinell, Knoop, Vickers, and Rochwell tests

in which the penetration depth of these tests are usually in the scale of micron (10^{-6} m) or millimeter (10^{-3} m) [43]. Nanoindentation is another indentation test in which the depth of penetration is measured in nanometers (10^{-9} m) [44]. This unique feature allows indenting on small volumes such as thin film. Another distinguishing feature of nanoindentation is the indirect measurement of the contact area. In nanoindentation test, the contact area is so small that it needs to be calculated from the penetration depth based on the tip geometry.

Nanoindentation can also be used to calculate the elastic modulus, the fracture toughness, and many other mechanical properties [45]. These properties are all design criteria for the application of materials including thermoelectric materials. In chapter 3, I will use the nanoindentation technique to characterize the mechanical properties of some thermoelectric materials.

1.4 Outline of my work

The major goals of my work are ranking the mechanical robustness of the common thermoelectric (TE) materials, then focusing on the mechanically strong TE materials, and improving their overall performance, including better cost performance, higher *ZT*, and higher output-power density.

Since the thermoelectric devices are mainly used when the reliability is more important than the power generation efficiency, the mechanical properties of TE materials would be one of the major concern in terms of application. For example, considering the waste-heat recovery from vehicles, the thermoelectric generator (TEG) would be exposed to thermal stress and mechanical vibrations. This would require the TEG being

mechanically and thermally stable. Although many success has been reported in improving *ZT*, the reports on mechanical properties of these thermoelectric materials remain scarce. In chapter 3, I will apply the nanoindentation to test the common thermoelectric materials (half-Heuslers, skutterudites, bismuth telluride, silicon–germanium alloys, and lead selenide), and to evaluate the hardness and the Young's modulus. As a result, the half-Heusler alloys exhibit considerably higher hardness and modulus values, and lower brittleness as compared with other materials. Thus, the half-Heusler alloys are considered ranking well-above competitive materials for use in thermoelectric power generators.

I will then spend effort on improving the thermoelectric properties of the half-Heusler alloys. The nanostructured half-Heusler alloys were reported possessing satisfactory *ZT*~1 in both the p-type and n-type materials [31-33, 40, 46-47]. However, the cost performances of these materials are unfavorable due to the use of the rare element, hafnium (Hf). In chapters 4 and 5, I managed improving the cost performance in the nanostructured p-type and n-type half-Heuslers by decreasing or even eliminating the Hf usage. The final products are more favorable for waste-heat recovery applications due to the lower specific power cost (dollars per watt, $\$ W^{-1}$).

Although the nanostructuring approach is powerful in improving *ZT* for many inorganic TE materials, it is only effective when the grain-size is comparable to or smaller than the phonon mean-free-path (MFP). For compounds with phonon MFP shorter than nano-sized grains, nanostructuring might impair the electron transport more than the phonon transport, thus potentially decreasing the power factor and *ZT*. Therefore, in chapter 6, I will introduce my study on NbFeSb-based p-type half-Heusler. I find that the

lattice thermal conductivity is not sensitive to the grain-size. Meanwhile, the carrier mobility improves significantly when the grains are larger. Thus, by increasing the grain-size, I managed to improve the electrical conductivity and maintain the Seebeck-coefficient while thermal conductivity is almost unchanged. This ultimately yields an ultra-high power factor (~106 μW $cm^{-1} K^{-2}$) and improved *ZT*. I will also show that the high power factor favors higher output-power density, and a record output-power density (~22 W cm^{-2}) is realized in a single-leg device operating between 293 and 868 K. Such a high output-power density can be beneficial for large-scale power generation applications.

1.5 References

[1] B. F. Tchanche, *et al.*, Low-grade heat conversion into power using organic Rankine cycles-A review of various applications, *Renew. Sustain. Energy Rev.* **15**, 3963-3979 (2011).

[2] F. Vélez, *et al.*, A technical, economical and market review of organic Rankine cycles for the conversion of low-grade heat for power generation, *Renew. Sustain. Energy Rev.* **16**, 4175-4189 (2012).

[3] R. Hu, *et al.*, Harvesting waste thermal energy using a carbon-nanotube-based thermo-electrochemical cell, *Nano Lett.* **10**, 838-846 (2010).

[4] S.W. Lee, *et al.*, An electrochemical system for efficiently harvesting low-grade heat energy, *Nat. Comm*. **5**, 3942 (2014).

[5] A. P. Straub, *et al.*, Harvesting low-grade heat energy using thermo-osmotic vapour transport through nanoporous membranes, *Nat. Energy* **1**, 16090 (2016).

[6] T. J. Seebeck, Abhandlungen der Deutschen Akademie der Wissenschaften zu Berlin. 265 (1823)

[7] J. C. Peltier, Nouvelles experiences sur la caloricite des courans electrique, *Ann. Chim.* LV1 371 (1834).

[8] W. Thomson, On a mechanical theory of thermoelectric currents, *Proc. Roy. Soc. Edinburgh* 91–98, (1851).

[9] E. Altenkirch, Elektrothermische Kälteerzeugung und reversible elektrische Heizung, *Physikalische Zeitschrift* **12**, 920 (1911).

[10] A. F. Ioffe, *Semi-conductor Thermoelements and Thermoelectric Cooling, Infosearch*, London, (1957).

[11] L. D. Hicks and M. S. Dresselhaus, Effect of quantum-well structures on the thermoelectric figure of merit, *Phys. Rev. B* **47**, 12727 (1993).

[12] L. D. Hicks and M. S. Dresselhaus, Thermoelectric figure of merit of a one-dimensional conductor, *Phys. Rev. B* **47**, 16631 (1993).

[13] M. S. Dresselhaus *et al.*, New Directions for Low-Dimensional Thermoelectric Materials, *Adv. Mater*. **19**, 1043 (2007).

[14] G. Chen, Thermal conductivity and ballistic-phonon transport in the cross-plane direction of superlattices, *Phys. Rev. B: Condens. Mater. Sci* **57**, 14958 (1998).

[15] R. Venkatasubramanian, *et al.*, Thin-film thermoelectric devices with high room-temperature figures of merit, *Nature* **413**, 597 (2001).

[16] T. C. Harman, *et al.*, Quantum dot superlattice thermoelectric materials and devices, *Science* **297**, 2229 (2002).

[17] T. Tritt, *Thermelectric Materials Research I* 139-253, Semiconductors and Semimetals Series 69, Elsevier, (2001).

[18] S. M. Kauzlarich, S. R. Brown and G. J. Snyder, Zintl phases for thermoelectric devices, *Dalton Trans.* **21**, 2099-2107 (2007).

[19] G. S. Nolas, J. Poon and M. Kanatzidis, Recent developments in bulk thermoelectric materials, *Mater. Res. Soc. Bull.* **31**, 199 (2006).

[20] K. F. Hsu, *et al.*, Cubic $AgPb_mSbTe_{2+m}$: bulk thermoelectric materials with high figure of merit, *Science*, **303**, 818 (2004).

[21] G. S. Nolas, *et al.*, The effect of rare-earth filling on the lattice thermal conductivity of skutterudites, *J. Appl. Phys.*, **79**, 4002 (1996).

[22] G. Chen, Semiconductors and Semimetals, *Recent Trends in Thermoelectric Materials Research*, **71**, 203-259, Ed. T. Tritt, Academic press, San Diego, (2001).

[23] B. Poudel, *et al.*, High-thermoelectric performance of nanostructured bismuth antimony telluride bulk alloys, *Science* **320**, 634-638 (2008).

[24] Q. Zhang, *et al*., Study of the thermoelectric properties of lead selenide doped with boron, gallium, indium, or thallium, *J. Am. Chem. Soc.* **134**, 17731-17738 (2012).

[25] Q. Zhang, *et al.*, Enhancement of thermoelectric performance of n-type PbSe by Cr doping with optimized carrier concentration, *Adv. Energy Mater.* **5**, 1401977 (2015).

[26] Q. Zhang, *et al.*, High thermoelectric performance by resonant dopant indium in nanostructured SnTe, *PNAS* **110**, 13261-13266 (2013).

[27] J. Yang, *et al.*, Solubility study of Yb in n-type skutterudites $Yb_xCo_4Sb_{12}$ and their enhanced thermoelectric properties, *Phys. Rev. B* **80**, 115329 (2009).

[28] T. Dahal, *et al.*, Thermoelectric property enhancement in Yb-doped n-type skutterudites $Yb_xCo_4Sb_{12}$, *Acta Mater.* **75**, 316-321 (2014).

[29] B. Yu, *et al.*, Thermoelectric properties of copper selenide with ordered selenium layer and disordered copper layer, *Nano Energy* **1**, 472-478 (2012).

[30] J. Shuai, *et al.*, Thermoelectric properties of Na-doped Zintl compound: $Mg_{3-x}Na_xSb_2$, *Acta Mater.* **93**, 187-193 (2015).

[31] X. Yan, *et al.*, Enhanced thermoelectric figure of merit of p-type half-Heuslers, *Nano Lett.* **11**, 556-560 (2011).

[32] S. Chen, *et al.*, Effect of Hf concentration on thermoelectric properties of nanostructured n-type half-Heusler materials $Hf_xZr_{1-x}NiSn_{0.99}Sb_{0.01}$, *Adv. Energy Mater.* **3**, 1210-1214 (2013).

[33] R. He, *et al.*, Investigating the thermoelectric properties of p-type half-Heusler $Hf_x(ZrTi)_{1-x}CoSb_{0.8}Sn_{0.2}$ by reducing Hf concentration for power generation. *RSC Adv.* **4**, 64711-64716 (2014).

[34] H. Zhao, *et al.*, High thermoelectric performance of MgAgSb-based materials, *Nano Energy* **7**, 97-103 (2014).

[35] W. Liu, *et al.*, N-type thermoelectric material $Mg_2Sn_{0.75}Ge_{0.25}$ for high power

generation, *PNAS* **112**, 3269-3274 (2015).

[36] M. Cutler, J. F. Leavy and R. L. Fitzpatrick, Electronic transport in semimetallic cerium sulfide, *Phys. Rev.*, **133**, A1143-A1152 (1964).

[37] M. Cutler, *et al.*, The conduction band of cerium sulfide $Ce_{3-x}S_4$, *J. Phys. Chem. Solids* **24**, 319-327 (1963).

[38] R. Franz and G. Wiedemann, *Annalen der Physik* (in German) **165** (8), 497–531 (1853).

[39] G. J. Snyder and E. S. Toberer, Complex thermoelectric materials, *Nat. materials,* **7** 105-114 (2008).

[40] G. Joshi, *et al.*, NbFeSb-based p-type half-Heuslers for power generation applications, *Energy & Environ. Sci.* **7**, 4070-4076 (2014).

[41] H. Li, *et al.*, High performance $In_xCe_yCo_4Sb_{12}$ thermoelectric materials with in-situ forming nanostructured InSb phase, *Appl. Phys. Lett.* **94**, 102114 (2009).

[42] G. Chen, *Nanoscale energy transport and conversion: a parallel treatment of electrons, molecules, phonons and photons*, Oxford University Press (2005).

[43] W. F. Hosford, *Mechanical behavior of materials*, Cambridge University Press (2005).

[44] W. C. Oliver and G. M. Pharr, An improved technique for determining hardness and elastic modulus using load and displacement sensing indentation experiments, *J. Mater. Res.* **7,** 1564 (1992).

[45] A. C. Fischer-Cripps, *Nanoindentation*, 3rd edition, Springer (2011).

[46] G. Joshi, *et al.* Enhancement in thermoelectric figure-of-merit of an n-type half-Heusler compound by the nanocomposite approach, *Adv. Energy Mater.* **1**, 643-647 (2011).

[47] C. Fu, *et al*., Band engineering of high performance p-type FeNbSb based half-Heusler thermoelectric materials for figure of merit zT> 1, *Energy Environ. Sci.* **8**, 216-220 (2015).

Chapter 2 Characterization of Thermoelectric Materials

2.1 Introduction

In chapter 1, the thermoelectric (TE) dynamics are introduced. Experimentally, the characterization of TE performances is much more straightforward. The thermoelectric figure-of-merit (ZT) has a very concise expression

$$ZT = \frac{S^2\sigma}{\kappa}T \tag{2.1}$$

To obtain ZT, we only need to measure the Seebeck-coefficient (S), the electrical conductivity (σ), and the thermal conductivity (κ) at the desired temperatures (T). Although conceptually simple, it's still challenging to experimentally reduce the errors in order to obtain high accuracy. Several papers, patents, and press releases have claimed extraordinarily high ZT but have never being repeated and likely resulted from incorrect measurements.

The experimental error has two parts: random error and systematic error [1]. Random error fluctuates from one measurement to the next, and can be minimized by averaging the results from multiple measurements. Systematic error tends to shift all measurements in a systematic way so the mean value is displaced. This may be due to incorrect calibration of equipment or the consistently improper use of equipment. The systematic error can be minimized by calibrating the experimental setups using standard samples.

One important aspect to accurately measure individual thermoelectric properties is taking data from the same sample and the same orientation to avoid problems of

inhomogeneity and anisotropy. In addition, the properties might change during the measurement due to annealing or evaporation when the measurement reaches high temperatures. Thus, multiple rounds of measurements might better characterize these properties.

In this chapter, I will introduce our measurement devices and their underlying working principles. The commercially available equipment (ZEM-3, Ulvac Inc.) was used for simultaneous measurement of the electrical conductivity and the Seebeck-coefficient. The thermal conductivity was calculated as a product of the thermal diffusivity, specific heat, and mass density which were measured by a laser-flash machine (LFA457, Netzsch), a differential-scanning calorimeter (DSC 404 C, Netzsch), and an Archimedes' kit.

2.2 Electrical conductivity measurement

The electrical conductivity is the inverse of the electrical resistivity. To minimize the error from the contact resistance, the four-probe method was used to measure the electrical conductivity. A typical four probe setup is shown in Figure 2.1. A constant current was provided into the conductor through the current probes, and the voltage was measured using the pair of voltage probes. Usually a series of currents were provided, and the voltage responses were recorded. The resistance was deduced from the slope of the *V*-*I* curve, and the resistivity was subsequently calculated by equation $\rho=AR/L$, where R is the resistance, A is the cross-sectional area and L is the distance between the two voltage probes.

The Peltier effect is a challenge when using the four-probe method to measure the electrical conductivity of thermoelectric materials. With current flowing, a temperature

gradient forms due to the Peltier effect. The temperature gradient will further superimpose a Seebeck voltage on the ohmic-voltage. This could be a significant contribution, especially for good thermoelectric materials that have low resistivity and high Seebeck-coefficient. To minimize the Seebeck-voltage contribution, it's preferable to use AC [2] or switching DC [3] as the electrical power supply.

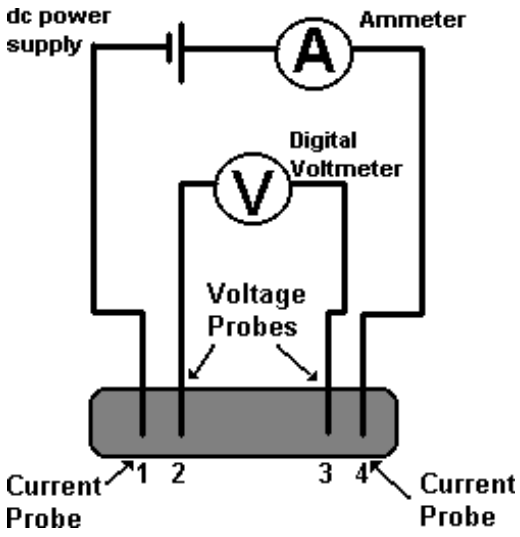

Figure 2.1 Schematic of a four-probe electrical conductivity measurement.

2.3 Room temperature Hall measurement

The Hall effect is named after E. H. Hall who discovered it in 1879 [4]. If an electric current flows through a conductor in a magnetic field, the magnetic field exerts a transverse force (the Lorenz force) on the moving charge carriers. As a result, the charge carriers accumulate on one face of the material and build up an electric field (ε) that is perpendicular to both the current direction and the magnetic field. A sketch of the Hall effect is shown in

Figure 2.2. Note that the sign of the Hall voltage (V_H) varies with the type of the majority carriers.

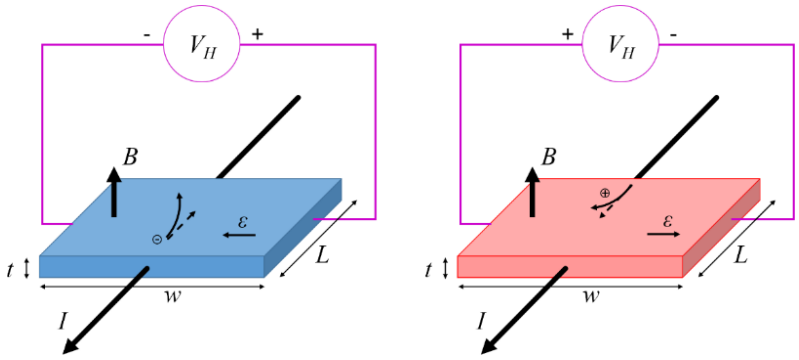

Figure 2.2 The Hall effect for electrons (left) and holes (right).

The Hall measurement is mainly employed to determine the carrier concentration (n_H) and mobility (μ). Consider a flat rectangular sample perpendicular to a uniform magnetic field, B. The thickness, width and length of the sample are t, w, and L, respectively. The length, L, is parallel to the current direction, I, as shown in Figure 2.2.

The Hall carrier concentration is given by

$$n_H = \frac{1}{R_H q} \tag{2.2}$$

where q is the charge of carrier, and R_H is the Hall coefficient, which is given by

$$R_H = \frac{V_H t}{IB} \tag{2.3}$$

The obtained carrier concentration is used to calculate the mobility (μ) using Eq. (1.8). However, this method is unfavorable since it requires the samples to be rectangular. In addition, the directions of the field and current has to be properly aligned.

In our experiments, the Hall measurement was performed using a physical property measurement system (PPMS, Quantum Design, Figure 2.3) with the *Van der Pauw* method that is capable of measuring the properties of samples with an arbitrary shape, provided that the sample is solid and approximately two-dimensional. The Van der Pauw method only requires the thickness of the sample, any size along the plane is not necessary.

Figure 2.3 PPMS (Quantum Design) for the Hall measurement

A typical Van der Pauw sample and the contacts are shown in Figure 2.4. The Van der Pauw method has four contacts (for convenience, they are numbered from 1 to 4 in a counter clockwise order).

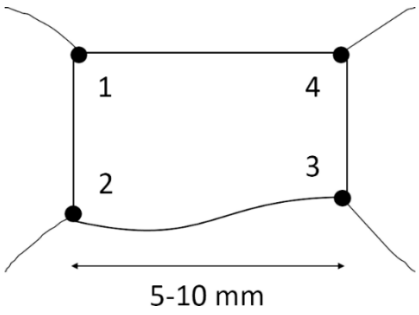

Figure 2.4 A schematic of Van der Pauw sample and contacts. Regular shapes of the samples are not necessary.

Before showing the Van der Pauw method, I make the following definitions first:

I_{mn}: A current injected from contact m, and taken out from contact n. For example, I_{13} means a current, I, that flows into the sample from contact 1 and flows out from contact 3.

$V_{mn,+}$: The DC voltage measured from contact m to n (*i.e.* V_n-V_m) under external positive (+) magnetic field (B). For example, $V_{42,+}$ means V_2-V_4 when the magnetic field is positive. Here, a positive magnetic-field direction is the same direction of the thumb when curling the rest fingers from contact 1 to contact 4 counterclockwise using right hand. If the magnetic field is negative, the symbol becomes "-". The positive and negative magnetic fields should be equal in absolute values during measurement.

A complete Hall measurement using the Van de Pauw method is:

1) With applied current I_{24}, measure $V_{13,+}$
2) I_{42}, $V_{31,+}$
3) I_{13}, $V_{42,+}$
4) I_{31}, $V_{24,+}$
5) I_{24}, $V_{13,-}$
6) I_{42}, $V_{31,-}$
7) I_{13}, $V_{42,-}$
8) I_{31}, $V_{24,-}$

The Hall voltage is given by

$$V_H = \frac{(V_{13,+}+V_{31,+}+V_{42,+}+V_{24,+})-(V_{13,-}+V_{31,-}+V_{42,-}+V_{24,-})}{8} \quad (2.4)$$

Eq. (2.2) through (2.4) were used to calculate the desired carrier concentration (n_H). The accuracy of the Van de Pauw method depends on the uniformity of the sample thickness, and size of the contacts. In addition, the thickness of the samples should be much less than the length and width to approximate the two-dimensional transport.

2.4 Seebeck-coefficient measurement

The Seebeck-coefficient, or thermopower, is intrinsically related to the materials' electronic structure, and not related to the sample geometry. Figure 2.5 shows the measurement schematics. One side of the sample is heated or cooled to create a temperature gradient. The voltmeter reads the voltage drop after the temperature profiles stabilize. In order to avoid the ohmic-voltage, the current is turned off during the Seebeck-coefficient measurement.

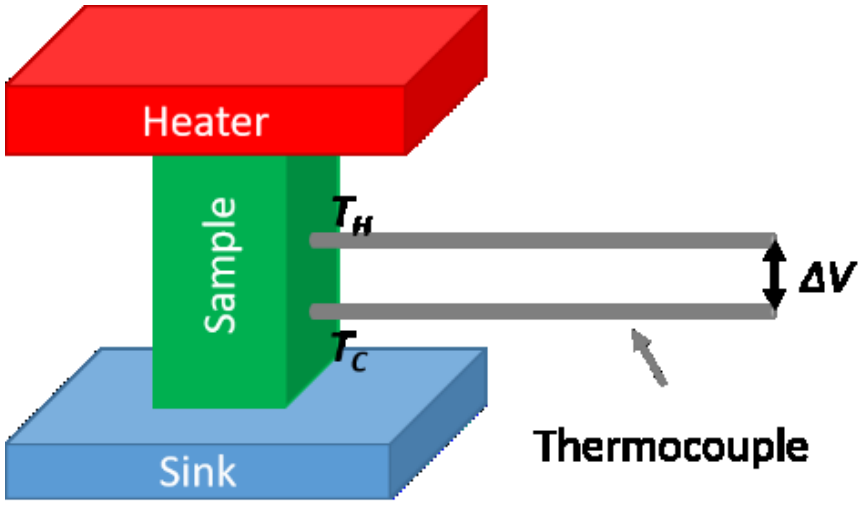

Figure 2.5 Schematic of the Seebeck-coefficient measurement

The measured voltage drop (ΔV) includes three parts

$$\Delta V = -\Delta T(S + S_{TC}) + V_{dark} \tag{2.5}$$

where S and S_{TC} are the Seebeck-coefficients from the sample and the thermocouple, respectively. The thermocouple Seebeck-coefficient (S_{TC}) were calibrated using a standard sample, which was usually the Cu-Ni alloy (constantan).

Figure 2.6 shows a typical ΔV vs. ΔT plot. For better accuracy, a set of small temperature differences were applied, yielding a set of voltage responses. The data points on the ΔV-ΔT plot were linearly fitted, and the slope gave the Seebeck-coefficient. The last term in Eq. (2.5) (V_{dark}) is called the *dark emf*. Ideally the ΔV-ΔT curves should pass through zero where there is no temperature gradient. However, there are always some non-zero intercepts. The intercept is the dark emf, as shown in Figure 2.6. Generally, the Seebeck-coefficient measurement is considered reliable when the dark emf does not exceed 10% of the total Seebeck voltage signal.

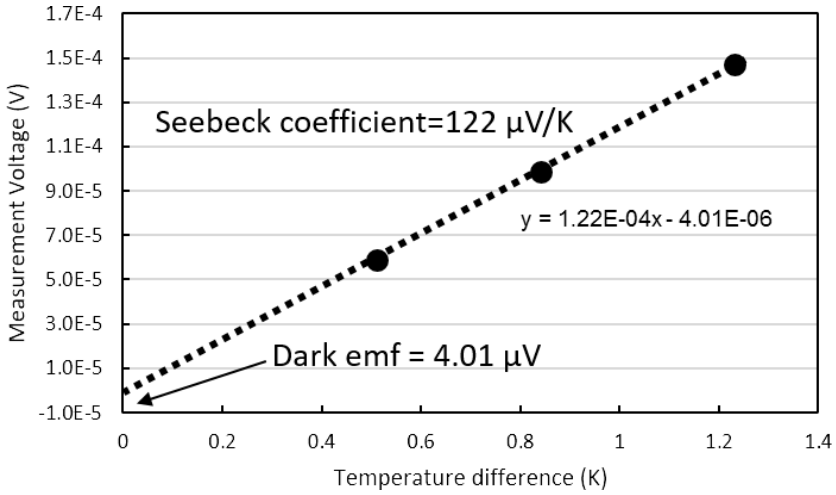

Figure 2.6 A typical ΔV–ΔT plot for Seebeck-coefficient measurement.

2.5 ZEM-3

In my experiments, both the electrical conductivity and the Seebeck-coefficient were measured in the commercial ZEM-3, as shown in Figure 2.7. Figure 2.8 shows a real sample loaded on the machine.

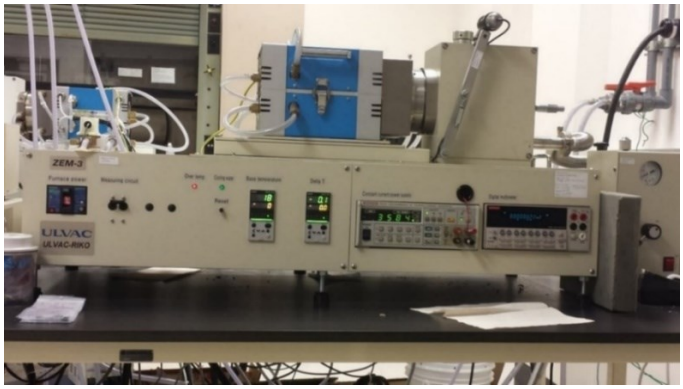

Figure 2.7 A picture of the ZEM-3 machine (Ulvac Inc.) used to measure the Seebeck-coefficient and electric conductivity.

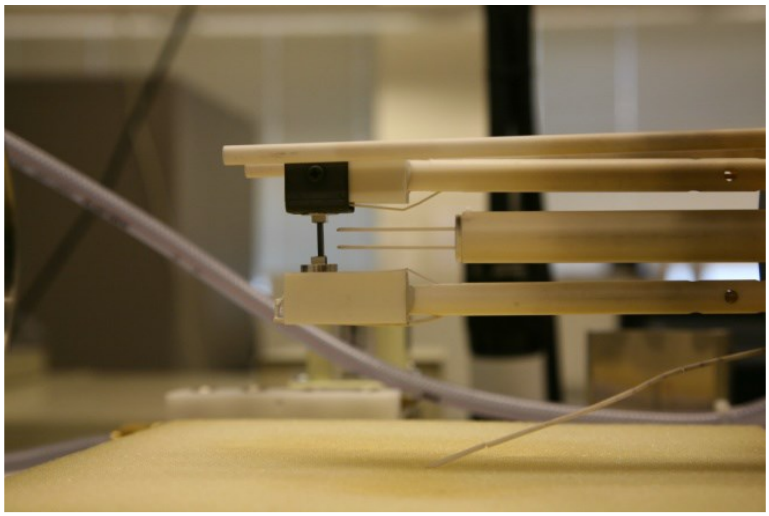

Figure 2.8 A picture of the sample holder with a mounted sample.

The measurements of the electrical conductivity and the Seebeck-coefficient could be carried out at up to 1000 °C if the samples were stable. The working condition of the sample chamber were a helium atmosphere at approximately 0.01 MPa. A complete measurement started from pumping and refilling the chamber with helium gas multiple times to expel oxygen. Upon heating, the temperature of sample increased to the desired values. To increase the accuracy, the measurement would not start unless the temperature variation was slower than a threshold value, usually 0.1 K per 10 seconds. The electrical conductivity was measured firstly using the four-probe approach with alternating DC power supply to cancel out the Seebeck-voltage contributions, as explained in section 2.2. Then the DC power source was turned off, and a set of temperature drops (ΔT) were applied across the material. The voltage drop (ΔV) was measured once the threshold of temperature stability satisfied. Usually, at least 4 different ΔT were used to produce a linear fit. After

subtracting the thermocouple contributions, the Seebeck-coefficients of the measured materials were obtained.

2.6 Thermal conductivity measurement

The thermal conductivity (κ) was evaluated primarily in terms of the Fourier's law for heat conduction.

$$\vec{q} = -\kappa \boldsymbol{\nabla} T \qquad (2.6)$$

where $\vec{q}$ is the heat-flux density. The unit of thermal conductivity is W m^{-1} K^{-1}. Compared to the electrical conductivity and the Seebeck-coefficient, the accuracy of thermal conductivity measurement was lower since heat insulation is more difficult than electrical insulation. Heat losses through conduction, convection, and radiation are always inevitable. Thus, extra care has to be taken to minimize the heat loss effects.

In my experiments, thermal conductivity was not measured directly. It was calculated as the product of thermal diffusivity (D, in the dimension of m^2 s^{-1}), specific heat (c_p, J kg^{-1} K^{-1}), and mass density (d, kg m^{-3}) that were measured by a laser-flash machine (LFA457, Netzsch), a differential-scanning calorimeter (DSC 404 C, Netzsch), and an Archimedes' kit.

$$\kappa = D \times c_p \times d \qquad (2.7)$$

2.6.1 Thermal-diffusivity and specific-heat measurement by laser-flash method

The laser-flash method was first described by Parker, *et al.* [5] in 1961 and it was reviewed in a number of references [6-8]. This method was improved subsequently by

Cowan [9], Cape & Lehman [10], and Blumm & Opfermann [11]. The laser-flash technique is very reliable for thermal-diffusivity measurements. This method has less contact issue since the samples are heated by laser. In addition, the temperature variations are read in a very short time so that the heat loss during the process can be minimized. A sketch of the laser-flash system is shown in Figure 2.9. The picture of an actual measurement system is shown in Figure 2.10.

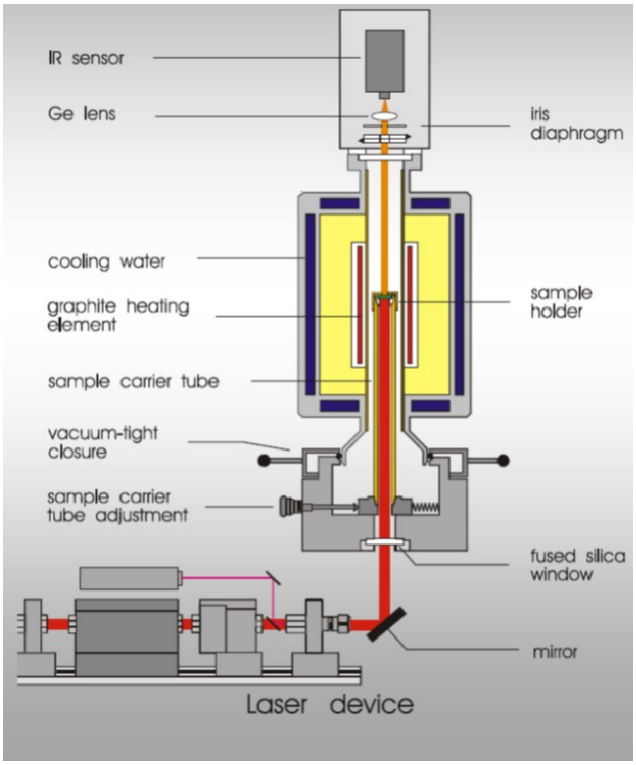

Figure 2.9 A sketch of the laser-flash method.

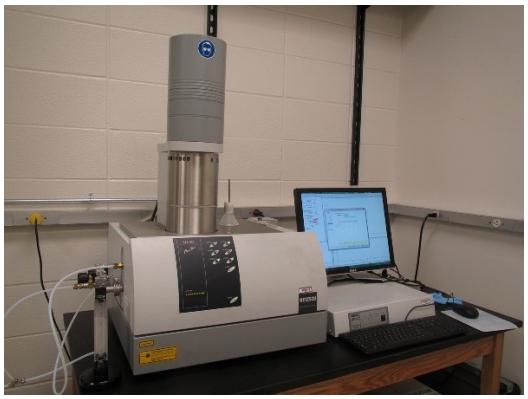

Figure 2.10 The laser-flash equipment for the thermal-diffusivity measurement

During measurement, one face of the sample was irradiated by a short pulse of laser, while the time-sensitive temperature rise on the opposite surface was recorded, from which the thermal diffusivity was calculated.

To better understand the measurement principles, let's consider a one-dimensional thermal-diffusion-transport equation and assume an adiabatic system, *i.e.* there is no heat loss. If a solid sample has uniform thickness, L, the temperature distribution at any later time, t, is given by [12],

$$T(x,t) = \frac{1}{L}\int_0^L T(x,0)dx + \frac{2}{L}\sum_{n=1}^{\infty} exp\left(\frac{-n^2\pi^2 Dt}{L^2}\right) \times \cos\frac{n\pi x}{L}\int_0^L T(x,0)\cos\frac{n\pi x}{L}dx \quad (2.8)$$

where D is the diffusivity. If a pulse of laser with energy Q is instantaneously and uniformly absorbed by a thin layer with depth, g, at the front side of the sample, then the initial condition becomes,

$T(x,0) = \frac{Q}{dc_p g}$, for $0<x<g$, and

$T(x, 0) = 0$, for $g<x<L$

where d is the sample density, and c_p is the specific heat. With this initial condition, Eq. (2.8) become

$$T(x,t) = \frac{Q}{dc_pL}\left[1 + 2\sum_{n=1}^{\infty} cos\frac{n\pi x}{L}\frac{sin(n\pi g/L)}{n\pi g/L} exp\left(\frac{-n^2\pi^2 Dt}{L^2}\right)\right] \quad (2.9)$$

Note that g is usually very small for opaque materials, then $sin(n\pi g/L) \approx n\pi g/L$. Since we are interested in the temperature variation at the rear surface where $x=L$, therefore, we get

$$T(L,t) = \frac{Q}{dc_pL}\left[1 + 2\sum_{n=1}^{\infty}(-1)^n exp\left(\frac{-n^2\pi^2 Dt}{L^2}\right)\right] \quad (2.10)$$

Define two dimensionless parameters, V and ω

$$V(L,t) = T(L,t)/T_M \quad (2.11)$$

$$\omega = \pi^2 Dt/L^2 \quad (2.12)$$

$$T_M = \frac{Q}{dc_pL} \quad (2.13)$$

T_M is the maximum temperature at the rear surface. Combining Eq. (2.10-2.12), we get

$$V = 1 + 2\sum_{n=1}^{\infty}(-1)^n exp(-n^2\omega) \quad (2.14)$$

Eq. (2.14) is plotted in Figure 2.11.

When V equals 0.5, ω equals 1.38. Therefore, the diffusivity is written as

$$D = \frac{1.38L^2}{\pi^2 t_{1/2}} \quad (2.15)$$

where $t_{1/2}$ is the time required for the rear surface to reach half of the maximum temperature rise.

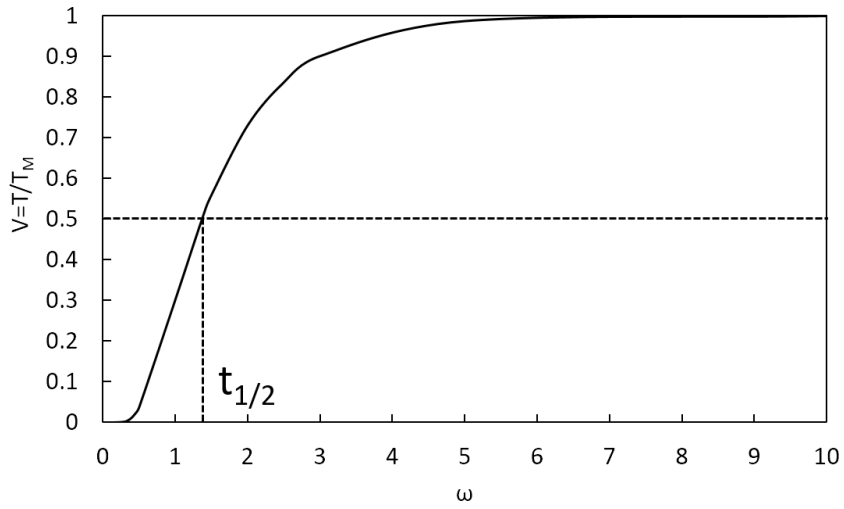

Figure 2.11 Dimensionless plot of rear surface temperature variation.

Eq. (2.15) is based on the adiabatic approximation, which is not accurate for the actual measurement. Several corrections are proposed that incorporate the radiation and convection on the surface [9], the transient heat transfer, finite pulse effects and heat losses [10], and pulse length correction [12]. The software in use contains a set of theoretical analysis that take all possible issues into account and I can choose the one that fits my experimental conditions. The measurement error for the diffusivity can be minimized to ~2%, most of which is attributed from the error in thickness measurement.

The laser-flash method can also measure the specific heat by using a standard specimen with a known specific heat, (c_p), and density, (d). From Eq. (2.13)

$$Q = dc_pLT_M = \left(dc_pLT_M\right)_{stanard} = \left(dc_pLT_M\right)_{sample} \tag{2.16}$$

This approach assumes identical laser pulse energy (Q) and maximum temperature on the rear surface (T_M) on both samples. This assumption is not always guaranteed since the size and thickness of the samples used in laser-flash measurement are large. Thus, the error in measuring the specific heat using the laser-flash method is ~5 to 10%. During our experiment, the differential-scanning calorimeter (DSC) method was used to measure the specific heat with better accuracy, as will be introduced in the following section.

2.6.2 Specific-heat measurement by differential-scanning calorimeter

Differential-scanning calorimeter (DSC) measures the difference of heat required to increase the temperature between a sample of interest and a reference material (usually sapphire). A picture of a DSC (404 C, Netzsch) is shown in Figure 2.12. The working principle of DSC is shown in Figure 2.13, where the magnified region on the upper right corner shows the sample stage that carries two crucibles, and there is one thermocouple below each of the crucibles. For specific-heat measurement, one of the crucibles was always left empty, while the samples and the reference will be loaded in another crucible. A typical measurement procedure starts with baseline-signal calibration by heating the two empty crucibles to the desired temperature. The baseline measurement was repeated at least twice until two successive signals overlap. Then the reference and the samples were loaded subsequently and the DSC signals were recorded upon heating. The DSC system controls the rate of temperature rise, and it was usually set at 20 K per minute.

Figure 2.12 A picture of a DSC 404C for specific-heat measurement.

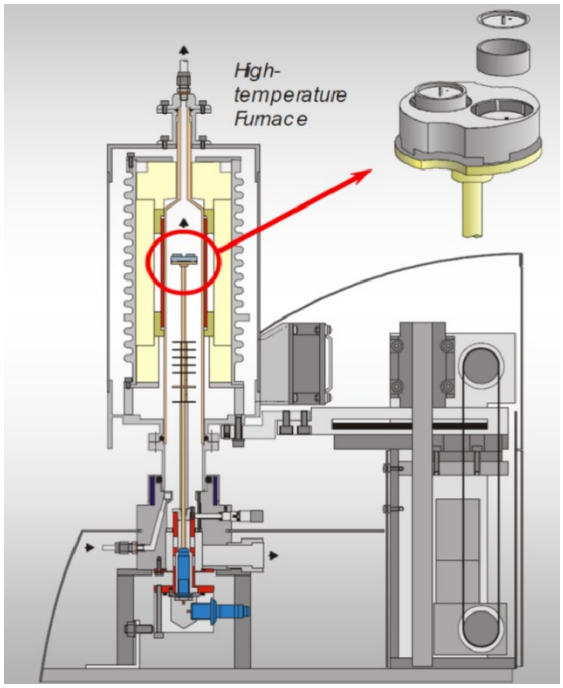

Figure 2.13 A sketch of the DSC 404C. The upper right corner shows the sample stage.

To understanding the measurement principles, we consider a heat input, δQ, to a specimen that causes an increase of temperature, dT. Therefore,

$$\delta Q^R(T) = m^R \cdot {c_p}^R(T) \cdot dT^R = DSC^R(T) - DSC^B(T) \quad (2.17)$$

$$\delta Q^S(T) = m^S \cdot {c_p}^S(T) \cdot dT^S = DSC^S(T) - DSC^B(T) \quad (2.18)$$

The superscripts *R*, *S* and *B* represent reference, sample, and baseline, respectively. Assuming the temperature rising of the samples are always the same as the setting value (20 K per minute), then

$$dT^R = dT^S = dT \quad (2.19)$$

We obtain the temperature-dependent specific heat

$${c_p}^S(T) = \frac{DSC^S(T) - DSC^B(T)}{DSC^R(T) - DSC^B(T)} \cdot \frac{m^R}{m^S} \cdot {c_p}^R(T) \quad (2.20)$$

For Eq. (2.19) to be valid, the sample surfaces should be smooth enough to ensure good thermal contact. In addition, the samples should be thin enough to guarantee temperature uniformity. The thicknesses of the samples were usually in the range between 0.5-1 mm. A typical measurement of specific heat is presented in Figure 2.14.

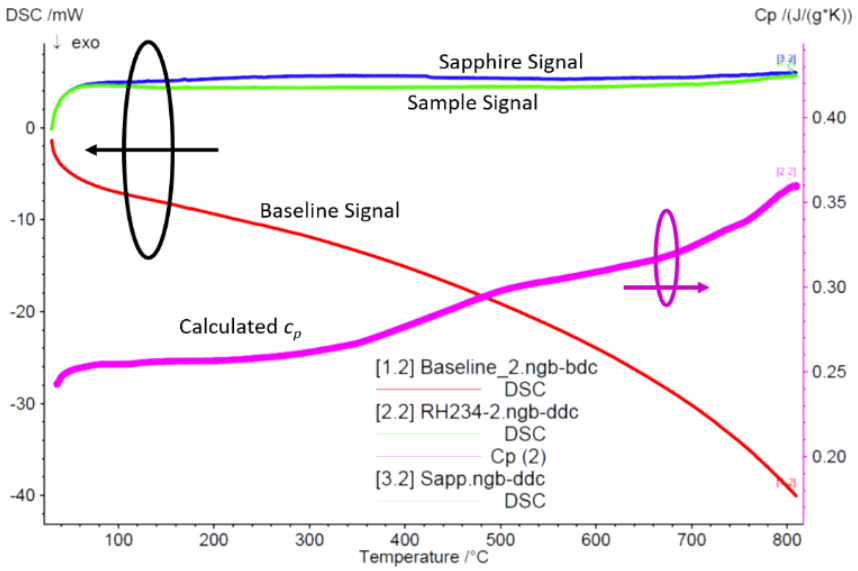

Figure 2.14 A typical c_p calculation using the DSC method.

2.7 References

[1] J. R. Taylor, *An introduction to error analysis: the study of uncertainties in physical measurements*, University Science Books (1997).

[2] H. J. Goldsmid, The electrical conductivity and thermoelectric power of bismuth telluride, *Proc. Phys. Soc. London.* **71**, 633 (1958).

[3] T. M. Dauphinee, S. B. Woods, Low-level thermocouple amplifier and a temperature regulation system, *Rev. Sci. Instrum.* **26**, 693 (1955).

[4] E. Hall, On a new action of the magnet on electric currents, *American Journal of Mathematics*, **2** 287–292 (1879).

[5] W. J. Parker, *et al.*, Flash method of determining thermal diffusivity, heat capacity, and thermal conductivity, *J. Appl. Phys.* **32**, 1679 (1961).

[6] F. Righini. and A. Cezarliyan, Pulse method of thermal-diffusivity measurements, *High Temp.-High Press.* **5**, 481 (1973).

[7] R. E. Taylor an K. D. Maglic, in *Compendium of Thermophysical Property Measurement Methods* **1**, 305, Plenum Press, NY (1984).

[8] R. Taylor, in *First European Conference on Thermoelectrics*, 107, Peter Peregrinus, London (1987).

[9] R. D. Cowan, Pulse method of measuring thermal diffusivity at high temperatures, *J. Appl. Phys.* **34**, 926 (1963).

[10] J. A. Cape and G. W. Lehman, Temperature and finite pulse-time effects in the flash method for measuring thermal diffusivity, *J. Appl. Phys.* **34**, 1909 (1963).

[11] J. Blumm and J. Opfermann, Improvement of the mathematical modeling of flash measurements, *High Temp.-High Press*. **34**, 515 (2002).

[12] H. S. Carslaw and J. C. Jaeger, *Conduction of Heat in Solids*, Oxford University Press, New York, (1959).

Chapter 3 Study on Mechanical Properties of Thermoelectric Materials Using Nanoindentation

A part of this chapter contains our previously published work:

R. He, *et al.*, Studies on mechanical properties of thermoelectric materials by nanoindentation, *Phys. Status Solidi A* **212**, 2191-2195 (2015).

3.1 Introduction

The thermoelectric (TE) technique is mainly applied where the stability is more important than conversion efficiency. In recent years, there are many enhancements of the TE figure-of-merit (ZT), and some reports claimed ZT as high as 2.6 in SnSe single crystal [1]. Indeed, the ZT improvement greatly facilitates the large-scale application of this technique. On the other hand, the mechanical robustness is also important for TE materials. This is especially true when the TE generator (TEG) is used for waste-heat recovery on vehicles, where the external mechanical vibration and thermal stress are loaded on the TEG. Materials that are mechanically weak might fail during operation [2]. Besides, some of the mechanical properties, such as the elastic constants and the coefficient of thermal expansion (CTE), are also related with phonon transport properties. Therefore, understanding the mechanical performance also helps optimizing the thermoelectric performance.

However, the reports of mechanical properties of TE materials remain limited. In this chapter, I will introduce the measurement of hardness and the Young's modulus using the nanoindentation technique and atomic force microscopy (AFM) correction [3]. The

tested materials are nanostructured half-Heuslers [4, 5], skutterudites [6, 7], bismuth tellurides [8, 9], silicon-germanium alloys [10, 11], and lead selenide [12] that are mainly used in the temperature range of 200–1000 °C. The measurement results provide a first-order ranking of these materials for subsequent studies.

3.2 Measurement principles

The nanoindentation experiments were performed on a Nanoindenter XP (MTS) machine, as shown in Figure 3.1. A diamond Berkovich tip was used as the indenter. The Berkovich tip has a threefold symmetry with an angle of 65.3° between the centerline and the three face, as shown in Figure 3.2.

Figure 3.1 A picture of the nanoindentation machine (Nano Indenter XP, MTS) for measuring hardness and the Young's modulus.

Figure 3.3 shows the working principle of a nano-indenter. A complete measurement cycle incorporates both the loading and unloading process. As the indenter

is driven into the surface, the tip meets both the elastic and plastic deformations. Upon unloading at the maximum displacement, h_{max}, the plastic deformation remains while the elastic deformation recoveries, leaving a residual impression depth, h_f, that is smaller than h_{max} [13-15]. The load-displacement curves (P-h curve) during the indenting tests are recorded, and the elastic properties and plastic properties could be effectively separated. A typical P-h curve during a nanoindentation test is shown in Figure 3.4.

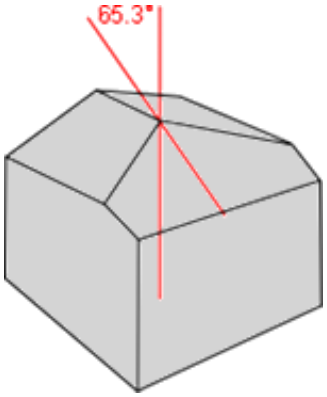

Figure 3.2 A sketch of the Berkovich tip for indenting.

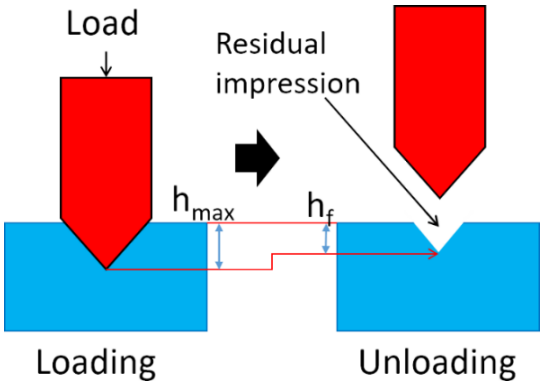

Figure 3.3 A sketch of the working principle of nanoindentation [3].

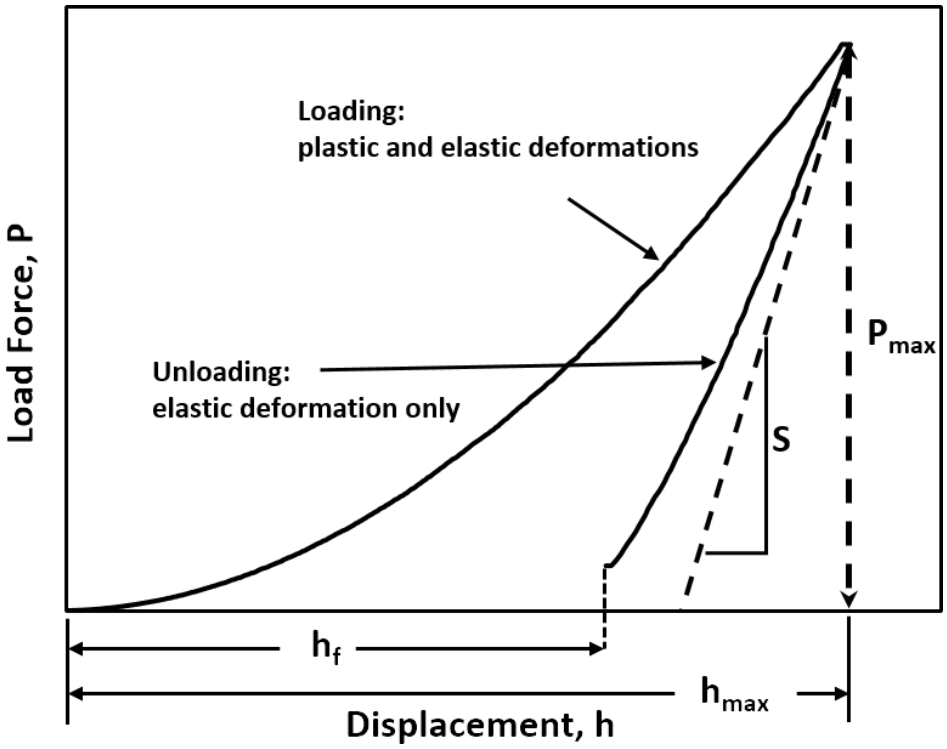

Figure 3.4 A typical P-h curve during indenting test using nanoindentation.

The hardness, *H*, is evaluated by the following equation,

$$H = \frac{P}{A} \tag{3.1}$$

where *P* is the load, and *A* is the projected contact area. As mentioned in chapter 1, the contact area is evaluated from the penetration depth, *h*, following the Oliver-Pharr method [13],

$$A = C_0 \cdot h^2 + C_1 \cdot h + C_2 \cdot h^{\frac{1}{2}} + C_3 \cdot h^{\frac{1}{4}} + C_4 \cdot h^{\frac{1}{8}} + C_5 \cdot h^{\frac{1}{16}} + \cdots \tag{3.2}$$

where the coefficients (C_i) are related to the tip geometry. The first coefficient, C_0=24.56, is the only non-zero term if the Berkovich tip is geometrically perfect. The other coefficients are the higher order corrections which are obtained by performing the

indentation tests on a standard material with isotropic, depth-independent elastic properties (usually the fused silica).

The Young's modulus, E, is given by the equation,

$$\frac{1}{E_r} = \frac{1-\upsilon^2}{E} + \frac{1-\upsilon_i{}^2}{E_i} \tag{3.3}$$

where υ is the Poisson's ratio of the sample and the subscript, i, is related to the tip material (diamond in our case, $\underline{E_i}$ = 1141 GPa and υ_i = 0.07). The reduced modulus, E_r, is given by,

$$E_r = \frac{\sqrt{\pi}\cdot S}{2\beta\sqrt{A}} \tag{3.4}$$

where β is a constant related to the geometric shape of the tip; for Berkovich tip, β=1.034. The contact stiffness, S, is taken as the initial slope of unloading-displacement curve, as shown in Figure 3.4.

3.3 Thermoelectric sample preparation

The tested materials include half-Heusler (n-type and p-type), skutterudites (n-type and p-type), bismuth telluride (n-type and p-type), silicon–germanium alloys (n-type and p-type), and lead selenide (p-type). All the materials were synthesized by our group and the experimental details can be found in literatures [4-12]. Here, I use the p-type half-Heusler as an example. Typically, the samples were prepared with three steps: melting, ball-milling, and sintering.

3.3.1 Melting

Typically, the sample preparation began with weighing the high purity elements (>99.9%) according to stoichiometry. Then the elements were melted to form the desired phases. There exist several melting methods such as bridge method, induction-melting, arc-melting, and zone-melting, *etc.* [16, 17]. Since the composition of our tested p-type half-Heusler, $Hf_{0.44}Zr_{0.44}Ti_{0.12}CoSb_{0.8}Sn_{0.2}$ [4], contained hafnium (Hf) that has high melting point (~2506 K), I chose the *arc-melting* technique because it can create a local high temperature by focused electric arc to melt Hf. The image of an arc-melting machine is shown in Figure 3.5. The weighed elements were placed in a copper crucible. Usually, the element with higher melting point were loaded on the top to melt the elements at the bottom. The copper crucible were transferred into the argon (Ar) protected melting chamber to prevent oxidation during the melting process. Usually one ingot was melted 3 to 4 times and flipped over each time to guarantee uniformity.

Figure 3.5 A picture of the arc-melting machine

3.3.2 Ball-milling

By using a high-energy ball-milling machine (Spex 8000, Spex Industries), the ingots prepared by arc-melting were crushed to nano-sized powders through repeated collisions between the materials and the steel balls inside a ball-milling jar [18]. The ball-milling process is simple and easy to handle, and also can be used to prepare oxygen-free fine powder under an argon environment. Figure 3.6 shows the stainless steel jars and balls, and a ball-milling machine (Spex 8000).

Since all the materials were previous reported and the preparation procedures were optimized, the ball-milling conditions were chosen in accordance with these reports [4-12]. For p-type half-Heusler studied in this chapter ($Hf_{0.44}Zr_{0.44}Ti_{0.12}CoSb_{0.8}Sn_{0.2}$), the ingots were milled by two stainless balls with diameter 12.7 mm for 5 hours in an argon environment [4].

Figure 3.6 Pictures show the stainless steel jar and balls, and a ball-milling machine (Spex 8000)

3.3.3 Sintering

High-density bulk samples are necessary for achieving good thermoelectric and mechanical properties. In my experiments, the powders prepared by ball-milling were sintered by using an alternating direct-current (DC) hot-press technique to form the nanostructured bulk samples. The sketch of our hot-pressing system is shown in Figure 3.7.

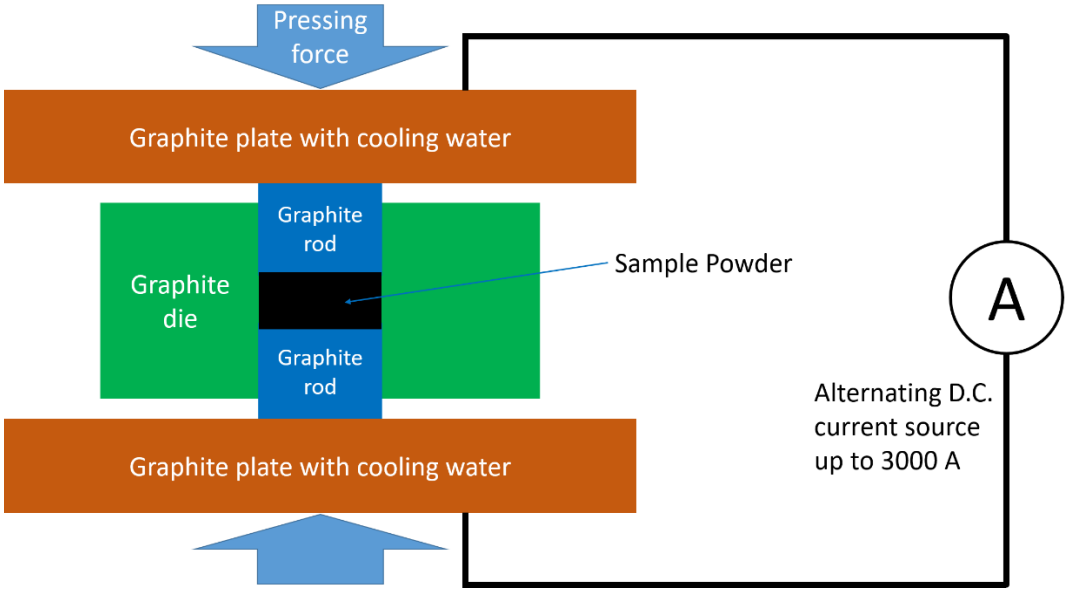

Figure 3.7 A simple sketch of the hot-pressing system.

Before sintering, the powders were loaded into the graphite die in an argon environment to prevent oxidation and moisture. For p-type half-Heusler, the powders were heated to 1125 °C with a temperature rising rate at 100 °C per minute. The peak temperature was maintained for 2 minutes. In addition, a pressure of 80 MPa was applied to assist the densification.

3.4 Sample characterizing

Prior to the indentation test, it's necessary to check the formation of the phases using the X-ray diffraction spectroscopy (XRD). The results showed that all the samples in this work possess desired pure phases. For example, Figure 3.8 shows the XRD spectroscopy of the p-type half-Heusler. The details of the half-Heusler crystal structures will be introduced in the next chapter.

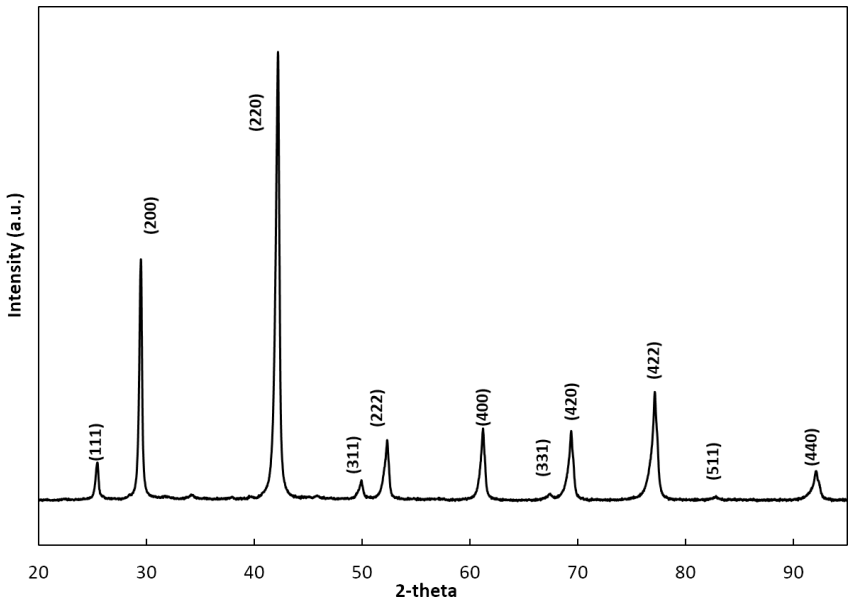

Figure 3.8 The XRD pattern of the as-pressed p-type half-Heusler (HH) sample, showing the formation of the HH phase [3].

Scanning electron microscopy (SEM) were used to examine the grain-sizes to check the possibilities of anisotropy mechanical behaviors due to the grain orientation. The SEM results showed that all the samples possess a grain-size smaller than 300 nm except for the bismuth telluride compounds. For example, the SEM image of p-type half-Heusler is shown in Figure 3.9. The SEM results demonstrated that most of our materials have no anisotropy, only the test of bismuth telluride compounds possessed anisotropy.

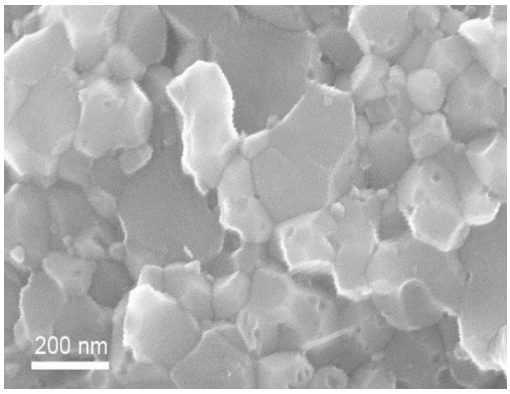

Figure 3.9 An SEM image of p-type half-Heusler, indicating grain-sizes of up to 300 nm [3].

3.5 Surface smoothening

For the indentation results to be reliable, the penetration depth should be 10 times larger than the surface roughness [14]. Since nanoindentation measures the mechanical properties at lengths between 0.1 μm to 1 μm, extra care is needed for surface smoothening. We developed a routine to effectively decrease the surface roughness [19].

Samples used for nanoindentation test are usually in disk shape with a diameter of 0.5 inch (12.7 cm) and thickness ~2 mm. It's important to keep the top and bottom parallel prior to smoothing the surface. This was done by using our sandpaper-polishing system. As shown in Figure 3.10, a double-sided tape stuck the samples to the top of a steel rod, which has a diameter slightly smaller than the inner size of a brass ring. During polishing, the steel rod was fitted into the brass ring, which applied a vertical load to the sample surface. This process guaranteed the uniformity of the sample thickness.

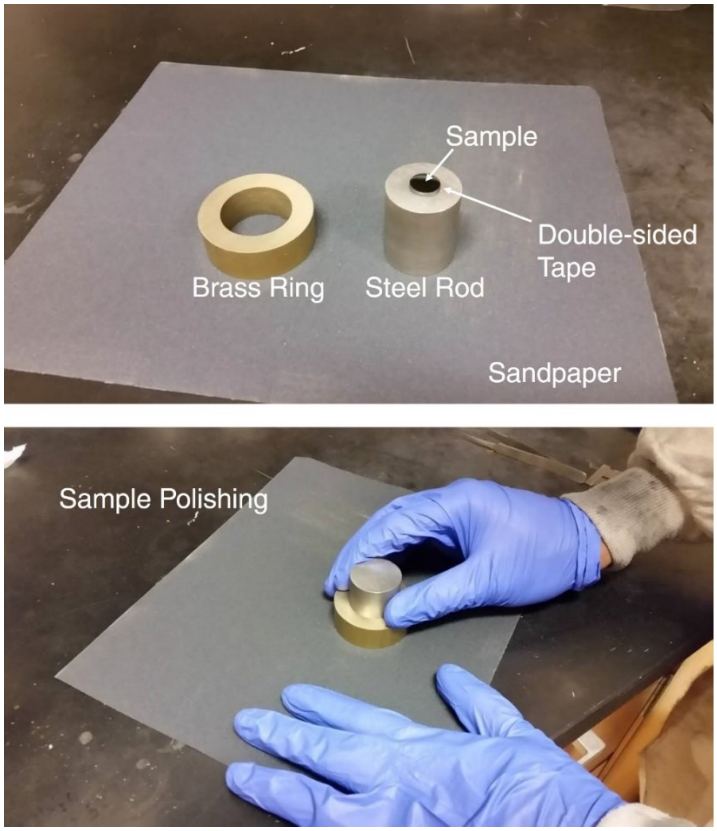

Figure 3.10 Pictures of the sandpaper polishing system.

The samples with parallel surfaces were cured in epoxy with one surface exposed to air. The exposure surfaces were polished again by sandpapers from 120 grit through 2500 grit. Then diamond suspension polishing was applied with average diamond particle-size decreasing from 3 μm through 0.1 μm using a polishing machine. The last step was a mechanical-chemical polishing process using colloidal silica in a vibromet (Buehler Vibromet I, Figure 3.11) for about 15 hours. The surfaces were examined using an atomic force microscopy (AFM), and the surface roughness was ~16 nm. The surface roughness is less than 10% to the minimum penetration depth in our experiments (~200 nm).

Therefore, our measurement provided reliable characterizing of the mechanical properties.

Figure 3.12 shows an AFM image of the p-type half-Heusler after fine polishing.

Figure 3.11 A picture of the vibromet polisher (Buehler Vibromet I) for surface fine polishing.

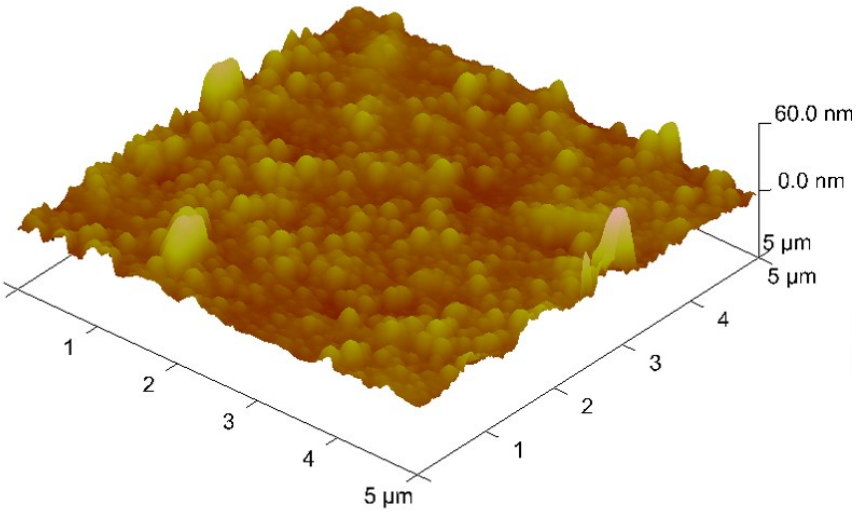

Figure 3.12 AFM scanning of the surface before indentation indicating a surface roughness of ~16 nm [3].

3.6 Nanoindentation tests, results, and discussion

I used an array of 10 ×10 indents, each 1 mm in depth, using the continuous stiffness measurement (CSM) method. In CSM method, a vibration movement was superimposed to the tip during the entire indenting procedure, thus allowed a continuous measurement of the stiffness (Figure 3.4), hardness, and modulus (Figure 3.13). The vibration frequency and displacement amplitude were set at 75 Hz and 1 nm, respectively, and the target strain rate was prescribed as 0.05 s^{-1}. The spacing between the 200 nm deep indents was 10 mm while that between the deeper indents was 25 mm.

The penetration-depth-dependent hardness, and modulus is shown in Figure 3.13 (only six representative curves are shown for clarity). The hardness of p-type half-Heusler ($Hf_{0.44}Zr_{0.44}Ti_{0.12}CoSb_{0.8}Sn_{0.2}$) was between 12 and 14 GPa (Figure 3.13a), and the modulus was between 200 and 250 GPa (Figure 3.10b). Table 3.1 is a compilation of the results of all the materials, with standard deviations from 100 indentations. A typical AFM micrograph characterization of the residual impression of an indent and its depth profile (Figure 3.14) highlights the pronounced mounding upon complete unloading, indicating minimal work-hardening during deformation [14]. This phenomenon was common in all the tested materials. For bismuth telluride and skutterudite, obvious spalling and chipping were observed at 1000 nm indentation depths. Hence, for these highly brittle materials, indentations were limited to lower depths (~200 nm). As a result, it was found that no spalling occurred at lower depth, meanwhile the average hardness and modulus values remained unaltered. Thus, I speculate that spalling at higher depths occurred during unloading.

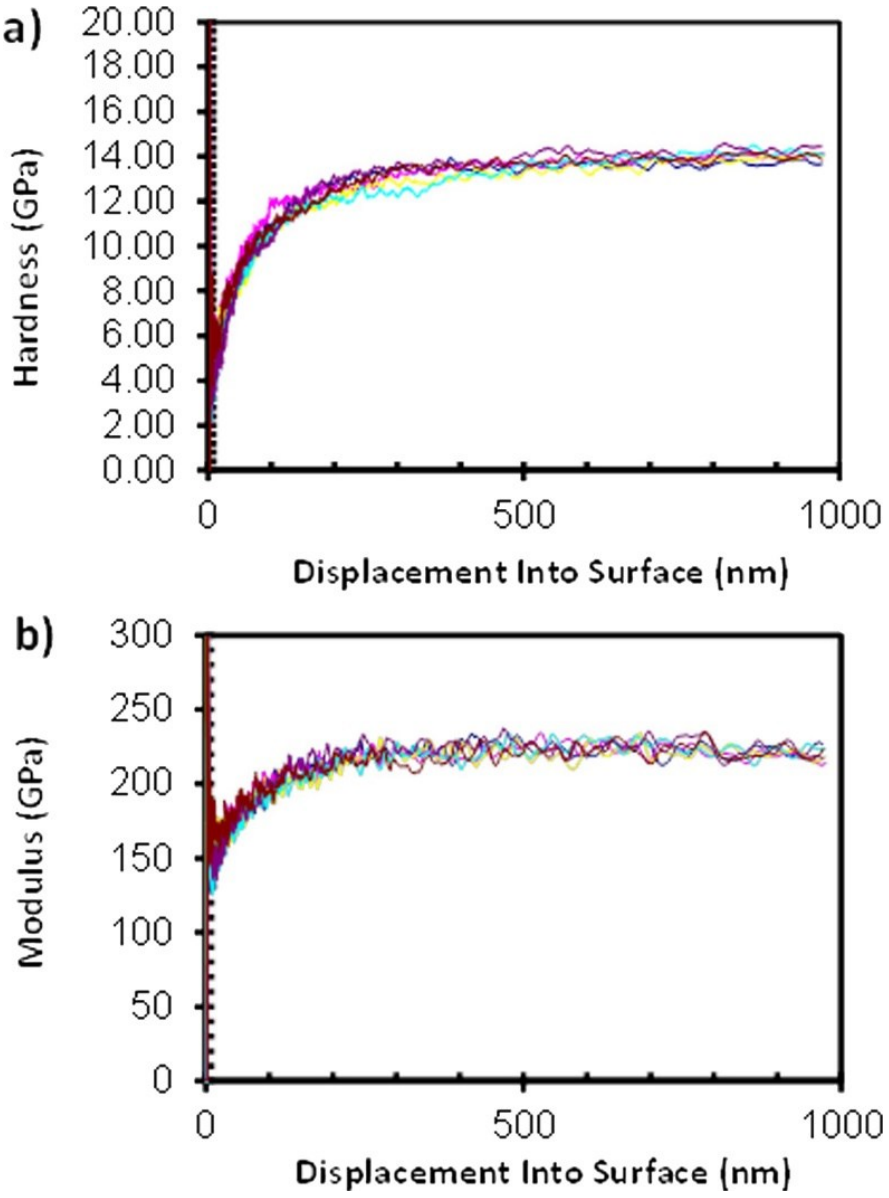

Figure 3.13 Hardness and Young's modulus results (both before correction) by nanoindentation. (a) Young's modulus and (b) hardness of $Hf_{0.44}Zr_{0.44}Ti_{0.12}CoSb_{0.8}Sn_{0.2}$. The indentation depth is set to be 1000 nm [3].

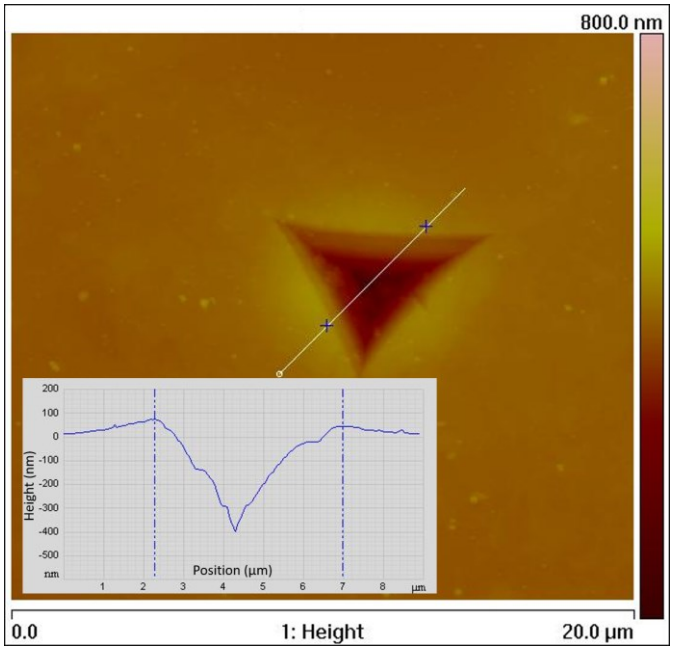

Figure 3.14 AFM image showing the residual impression of a typical indentation (1 micron deep) and the depth profile (inset) on the surface of p-type half-Heusler. The maximum mounding shown by the profile along the line across the indent is about 70 nm and is indicated by the two vertical blue lines within the inset [3].

Bolshakov and Pharr [20] have shown that the procedures developed by Oliver and Pharr [13] to calculate hardness and elastic modulus gave inaccurate results in cases where mounding occurs. Therefore, following Li *et al.* [21], we added the average mound height to the contact depth to adjust the contact area in Eqs. (3.1) through (3.4), thereby more accurately representing the contact area to correct the hardness and modulus, as shown in Table 3.1. However, Note that this correction still did not provide the contact area at full load. The contact diameter ranged from 700 nm to more than 3 µm with a corresponding indentation depth ranging between 200 nm and 1 µm. For the most of the materials that were nanostructured, such as half-Heusler (Figure 3.6), the contact diameter exceeded the largest grain-size (300 nm), confirming that the hardness and elastic modulus represent

averaged quantities over many grains. Such an averaging effect also nullified the effect of crystallographic orientations of individual grains on the mounding behavior, thereby lending threefold symmetry to the indentations as a consequence of the indenter symmetry.

On the contrary, for the large grain-sized materials, a single grain might be isolated by the tip contact. Thus, depending on the crystal structure of the different materials tested and the crystallographic orientation of the indented grains, the threefold symmetry of Berkovich tip resulted in anisotropic mounding. Figure 3.15, an AFM micrograph of a 300 nm deep indent made in $Bi_{0.4}Sb_{1.6}Te$ highlighted the degree of anisotropy and the crystallographic effect on the mounding behavior.

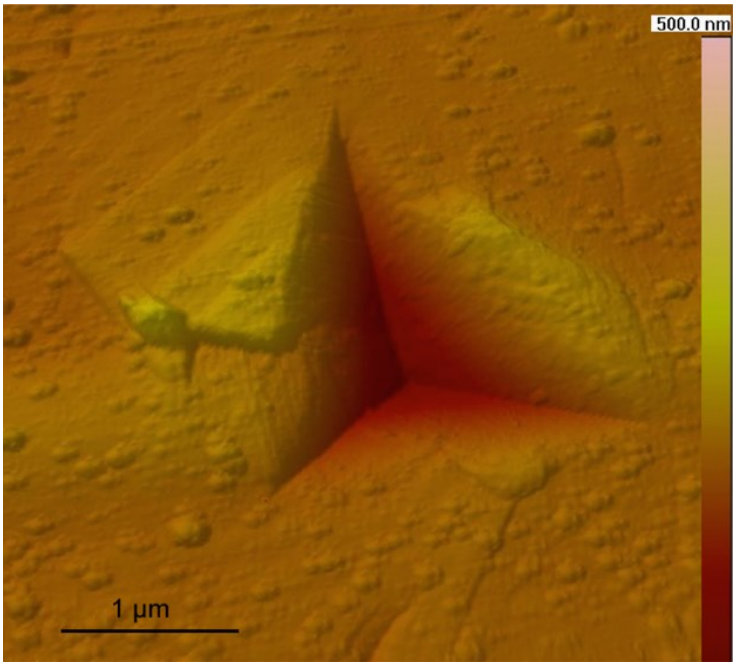

Figure 3.15 AFM micrograph of the residual impression of a 300 nm deep indentation made in $Bi_{0.4}Sb_{1.6}Te_3$ [3].

Note that for materials with high contact stiffness or high *E/H* ratio, the continuous stiffness measurement (CSM) method introduces additional errors in *H* and *E* measurements, especially at low indentation-depths [22]. However, because of the small ratios of *E/H* for the present materials (ranging from 20 to 40), I expect negligible discrepancies between our results obtained from depth-controlled and load-controlled methods. Considering the extreme case of $Bi_{0.4}Sb_{1.6}Te$ with *E/H* ~37 and indentation depth ~200 nm, the CSM method yields *H* ~1.52GPa and *E* ~49 GPa while the load-controlled nanoindentation gives nearly the same values of *H* ~1.44 GPa and *E* ~50 GPa, which guarantees the validity of our analysis.

Note that while higher elastic moduli may imply higher fracture strength, it may deteriorate the thermal-shock resistance under certain design conditions. For instance, the fracture strength and, consequently, fracture toughness vary directly with the Young's modulus: $\sigma_f = \sqrt{\frac{2\gamma E}{\pi a^*}}$, where σ_f, γ, E, and a^* are the fracture strength, surface energy, Young's modulus, and critical flaw size, respectively. However, of the five thermal-shock resistance parameters, *R*, *R'*, and *R''* signify resistance to fracture initiation and vary weakly with modulus as $(1/E)^{1/2}$ while *R'''* and *R''''* denote thermal-shock fracture toughness and have no dependence on *E*. For example,

$$R = \frac{\sigma_f (1-\nu)}{E\alpha} \propto \frac{1}{\sqrt{E}} \tag{3.5}$$

$$R''' = \frac{E}{{\sigma_f}^2(1-\nu)} = \frac{\pi a^*}{2\gamma(1-\nu)} \tag{3.6}$$

where R, R''' are thermal-shock resistance parameters, α is the coefficient of thermal expansion (CTE) and v is the Poisson's ratio [23, 24]. In fact, the dependence of thermal-shock resistance parameters on E varies depending on whether one is considering the problem of crack initiation or that of crack propagation. Thus, while H and E are important quantities, a complete mechanical characterization of a material requires the determination of other properties like flexural strength and toughness.

Table 3.1 Nanoindentation studies on TE materials [3].

Specimen Composition	Nanoindentation(GPa)		After AFM corrections(GPa)	
	Hardness	Modulus	Hardness	Modulus
P-type half Heusler	13.9 $\pm$ 0.3	231.0 $\pm$ 6.2	12.8	221.0
N-type half Heusler*	9.9 $\pm$ 1.2	213.9 $\pm$ 17.6	9.1	186.5
P-type $Bi_{0.4}Sb_{1.6}Te_3$*	1.5 $\pm$ 0.1	48.7 $\pm$ 4.4	1.1	41.5
N-type $Bi_2Te_{2.7}Se_{0.3}$*	1.4 $\pm$ 0.1	42.8 $\pm$ 5.6	1.2	38.8
P-type SKU*	6.8 $\pm$ 0.4	144.0 $\pm$ 11.0	5.6	129.7
N-type SKU*	7.1 $\pm$ 2.2	152.2 $\pm$ 21.9	5.8	136.9
N-type $Si_{0.8}Ge_{0.2}P_2$	11.9 $\pm$ 0.7	175.2 $\pm$ 7.1	10.8	166.3
P-type $Si_{0.8}Ge_{0.2}B_5$	11.8 $\pm$ 0.9	163.9 $\pm$ 4.6	10.7	155.6
P-type $In_{0.005}PbSe$	0.7 $\pm$ 0.1	74.1 $\pm$ 5.9	0.6	65.9

* denotes results from 200 nm deep indents.

P-type half Heusler: $Hf_{0.44}Zr_{0.44}Ti_{0.12}CoSb_{0.8}Sn_{0.2}$

N-type half Heusler: $Hf_{0.25}Zr_{0.75}NiSn_{0.99}Sb_{0.01}$

P-type SKU: $Ce_{0.45}Nd_{0.45}Fe_{3.5}Co_{0.5}Sb_{12}$

N-type SKU: $Yb_{0.35}Co_4Sb_{12}$

3.7 Summary

The hardness and elastic modulus of half-Heusler, skutterudite, bismuth telluride, lead selenide, and silicon-germanium alloys were tested using nanoindentation technique. It was found that the hardness and elastic modulus of the previously reported p-type half-Heusler, $Hf_{0.44}Zr_{0.44}Ti_{0.12}CoSb_{0.8}Sn_{0.2}$ were about 13 and 221 GPa with indentation depths of ~1000 nm. These values were much higher than those obtained for other moderate temperature range TE materials. We might conclude that half-Heusler ranks well above competitive materials for use in thermoelectric power generators, where the demands for mechanical stability are equally important as the energy conversion efficiency. Although, high elastic modulus enhances the fracture toughness, a negative impact on the material's thermal-shock resistance was expected. Therefore, hardness alone is not a complete design parameter, particularly within the context of complex mechanical environments, such as vibrations, thermal-shocks typically seen by automobile devices. These results offered a rapid, first-order ranking to consider further detailed studies of these TE materials.

3.8 References

[1] L. D. Zhao, *et al.*, Ultralow thermal conductivity and high thermoelectric figure of merit in SnSe crystals, *Nature* **508**, 373–377 (2014).

[2] J. H. Yang and F. R. Stabler, Automotive applications of thermoelectric materials, *J. Electron. Mater.* **38**, 1245 (2009).

[3] R. He, *et al.*, Studies on mechanical properties of thermoelectric materials by nanoindentation*, Phys. Status Solidi A* **212**, 2191-2195 (2015).

[4] X. Yan, *et al.*, Enhanced thermoelectric figure of merit of p-Type half-Heuslers, *Nano Lett.* **11**, 556–560 (2011).

[5] S. Chen, *et al.*, Effect of Hf concentration on thermoelectric properties of nanostructured n-type half-Heusler materials $Hf_xZr_{1-x}NiSn_{0.99}Sb_{0.01}$, *Adv. Energy Mater.* **3**, 1210-1214 (2013).

[6] T. Dahal, *et al.*, Thermoelectric property enhancement in Yb-doped n-type skutterudites $Yb_xCo_4Sb_{12}$, *Acta Mater.* **75**, 316-321 (2014).

[7] Q. Jie, *et al.*, Fast phase formation of double-filled p-type skutterudites by ball-milling and hot-pressing, *Phys. Chem. Chem. Phys.* **15**, 6809-6816 (2013).

[8] B. Poudel, *et al.*, High-thermoelectric performance of nanostructured bismuth antimony telluride bulk alloys, *Science* **320**, 634 (2008).

[9] W. S. Liu, *et al.*, Studies on the Bi_2Te_3-Bi_2Se_3-Bi_2S_3 system for mid-temperature thermoelectric energy conversion, *Energy & Environ. Sci.* **6**, 552-560 (2013).

[10] X. W. Wang, *et al.*, Enhanced thermoelectric figure of merit in nanostructured n-type silicon germanium bulk alloy, *Appl. Phys. Lett.* **93**, 193121 (2008).

[11] G. Joshi, *et al.*, Enhanced thermoelectric figure-of-merit in nanostructured p-type silicon germanium bulk alloys, *Nano Lett.* **8**, 4670-4674 (2008).

[12] Q. Zhang, *et al.*, Study of the thermoelectric properties of lead selenide doped with boron, gallium, indium, or thallium, *J. Am. Chem. Soc.* **134**, 17731-17738 (2012).

[13] W. C. Oliver and G. M. Pharr, An improved technique for determining hardness and elastic modulus using load and displacement sensing indentation experiments, *J. Mater. Res.* **7**, 1564 (1992).

[14] A. C. Fischer-Cripps, *Nanoindentation*, Springer, New York (2011).

[15] W. C. Oliver and G. M. Pharr, Measurement of hardness and elastic modulus by instrumented indentation: Advances in understanding and refinements to methodology, *J. Mater. Res.* **19**, 3 (2004).

[16] A. Borshchevsky, *et al.*, Preliminary results on zone-leveling of multidoped SiGe thermoelectric alloys, *In Proc. 7th Symp. Space Power Syst.*, Albuquerque, 229-233 (1990).

[17] T. Caillat, *et al.*, Study of the Bi-Sb-Te ternary phase diagram, *J. Phys. Chem. Solids* **53**, 227 (1992).

[18] C. Suryanarayana, Mechanical alloying and milling, *Proc. in Mater. Sci.* **46**, 1-184 (2001).

[19] S. Gahlawat, *et al.*, Elastic constants determined by nanoindentation for p-type thermoelectric half-Heusler, *J. Appl. Phys.* **116**, 083516 (2014).

[20] A. Bolshakov and G. M. Pharr, Influences of pile-up on the measurement of mechanical properties by load and depth sensing indentation techniques, *J. Mater. Res.* **13**, 1049 (1998).

[21] Z. Y. Li, *et al.*, On two indentation hardness definitions, *Surf. Coat. Technol.* **154**, 124 (2002).

[22] G. M. Pharr, *et al.*, Critical issues in making small-depth mechanical property measurements by nanoindentation with continuous stiffness measurement, *J. Mater. Res.* **24**, 653 (2009).

[23] D. P. H. Hasselman, Elastic energy at fracture and surface energy as design criteria for thermal shock, *J. Am. Chem. Soc.* **46**, 535 (1963).

[24] D. P. H. Hasselman, Unified theory of thermal shock fracture initiation and crack propagation in brittle ceramics, *J. Am. Chem. Soc*. **52**, 600 (1969).

Chapter 4 Thermoelectric Properties of P-type Half-Heusler $MCoSb_{0.8}Sn_{0.2}$ (M=Hf, Zr, Ti)

A part of this chapter contains our previously published work:

R. He, *et al.*, Investigating the thermoelectric properties of p-type half-Heusler $Hf_x(ZrTi)_{1-x}CoSb_{0.8}Sn_{0.2}$ by reducing Hf concentration for power generation*, RSC Adv*. **4**, 64711-64716 (2014).

4.1 Introduction

Half-Heusler (HH) compounds are promising materials for thermoelectric (TE) applications due to their robust mechanical performances, as shown in chapter 3 [1]. Besides, HH compounds are environmentally friendly since the commonly used elements are non-toxic. On the other hand, the drawback of the HH is the relatively high-elemental cost [2]. The p-type and n-type materials have the compositions of $Hf_{0.44}Zr_{0.44}Ti_{0.12}CoSb_{0.8}Sn_{0.2}$ and $Hf_{0.25}Zr_{0.75}NiSn_{0.99}Sb_{0.01}$, respectively, and the high material cost originates from the usage of the expensive element, hafnium (Hf). The market prices of the commonly used elements in half-Heuslers are shown in Table 4.1 [3]. Hf is extremely expensive in comparison with other elements. Based on this table, a simple calculation shows that the price of the p-type and n-type HH compounds shown above are ~\$174 kg^{-1} and ~\$125 kg^{-1}, respectively. The material prices of HH are lower than the bismuth telluride (Bi_2Te_3) and silicon germanium (Si-Ge) based TE materials, but much more expensive than the skutterudite compounds and Mg_2Si-based compounds [2]. For practical applications, lower material-cost is preferable. Thus, successful suppressing of Hf

usage while keeping good TE performances will effectively enhance the cost performance and accelerate the applications of HH-based TE devices. In this and the next chapters, I will discuss the improved cost performance in p-type and n-type half-Heusler materials.

Table 4.1 The price of relevant elements in the year 2010 [3].

Elements	Hf	Zr	Ti	Ni	Sn	Sb	Nb*	Co
Prices ($ kg^{-1})	563	99.8	10.7	21.8	27.3	8.8	14.3	46

*The price of Nb is in year 2005

4.1.1 Crystal structure

The Half-Heusler (HH) compounds are crystallized in the space group $F\bar{4}3m$, and their structures can be viewed as a zinc blende structure with occupied octahedral sites. The HH compounds typically possess the formula XYZ, where X can be a transition metal, a noble metal, or a rare-earth element, Y is a transition metal or a noble metal, and Z is a main group element [4]. The elements X, Y, and Z occupy the Wyckoff positions 4b, 4c, and 4a, respectively, and the 4d position is empty (Figure 4.1). Note that if the 4d position is also occupied, the structure is named Full-Heusler (FH). Among the hundreds of HH compounds, the ones with valance-electron-counts 8 and 18 are semiconductors [4], where the band gap forms due to the strong hybridization between X and Y atoms [5, 6].

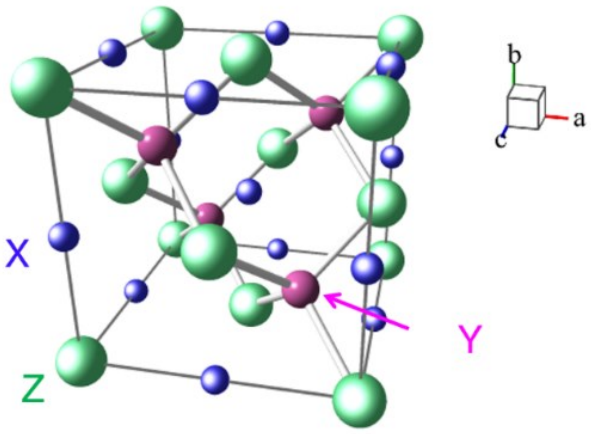

Figure 4.1 Crystal structure of half-Heusler XYZ, where X, Y, Z occupy the Wyckoff position 4b (1/2, 1/2, 1/2), 4c (1/4, 1/4, 1/4) and 4a (0, 0, 0), respectively.

4.1.2 Early work on p-type half-Heusler *M*CoSb

Good thermoelectric properties of half-Heusler (HH) compounds were first reported in the ZrNiSn-based n-type material by F.G. Aliev, *et al.* (1989, 1990), at USSR [7, 8]. Then in the late 1980s and early 1990s, good thermopower values were also discovered in the MCoSb-based (M=Hf, Zr, Ti) half-Heusler compounds [9]. Although the MCoSb-based half-Heusler is intrinsically n-type, better p-type properties were found with proper dopants, such as Sn at the Sb site, and Fe at the Co site [10, 11]. A power factor as high as ~30 μW cm^{-1} K^{-2} were realized with substitution of Sn at the Sb site [12]. However, the thermal conductivity of half-Heusler is much higher than other common thermoelectric materials. For example, the thermal conductivities at room temperature are ~10 W m^{-1} K^{-1} for $ZrCoSb_{1-x}Sn_x$ and ~4 W m^{-1} $K^{-1}$for $Hf_{0.5}Zr_{0.5}CoSb_{1-x}Sn_x$ [12, 13], while the thermal conductivities of Bi_2Te_3-based TE materials could be as low as ~1 W m^{-1} K^{-1} [14]. The high

thermal conductivity of half-Heusler hinders the improvement of *ZT*. One way to reduce the thermal conductivity is by using the isoelectronic substitution among Hf, Zr, and Ti [13, 15]. This approach enhances the point-defect phonon-scattering by the increased difference of atomic mass and radius. An improved *ZT* of ~0.5 was reported at 700 °C in $Hf_{0.5}Zr_{0.5}CoSb_{0.8}Sn_{0.2}$ [13].

Another way to decrease the thermal conductivity is by introducing secondary precipitates, usually the oxides MO_2 [11, 16-17], with M being Hf, Zr, and Ti. The oxides could be introduced either *ex-situ* or *in-situ*. For example, Wu *et al.* reported the *in-situ* formation of TiO_2 precipitates in $TiCo_{1-x}Fe_xSb$ by using partially oxidized Fe as the starting material [11]. During arc-melting, the following reaction occurred,

$$2Fe_2O_3+3Ti == 3TiO_2+4Fe$$

The TiO_2 nano precipitates were embedded in the half-Heusler matrix and scattered phonons. As a result, the thermal conductivity decreased significantly with increased nominal oxidized Fe. The peak *ZT* ~0.45 was obtained at ~850 K with 15% nominal Fe substitution at the Co site.

Except for TiO_2, the *in-situ* formed HfO_2 nano inclusions, and *ex-situ* introduced ZrO_2 nano powders were also reported as effective secondary phases in phonon scattering [16, 17]. These oxide inclusions suppressed the thermal conductivity and improved *ZT*. However, the oxides also deteriorated the electron transport and yielded lower electrical conductivity and power factor. Therefore, the improvements of *ZT* in these cases were not significant.

4.1.3 Nanostructuring

In 2011, the breakthrough in p-type half-Heusler was achieved in our group by using nanostructure [18]. In the compound, $Hf_{0.5}Zr_{0.5}CoSb_{0.8}Sn_{0.2}$, the thermal conductivity was significantly suppressed due to the enhanced grain-boundary scattering of phonons in the nanostructured compounds. This was done by applying a high-energy ball-milling technique to the alloy ingots that were obtained through arc-melting the raw elements, as shown in the last chapter. The nanostructure was confirmed by TEM characterization, as shown in Figures 4.2a and 4.2b, where the grain-sizes after ball-milling were in the order of ~10 nm. Then the powders were sintered into a dense sample at elevated temperatures (~1100 to 1150 °C) and external pressure (~80 MPa) by using a DC hot-pressing. The final products were well crystallized with an average grain-size of ~200 nm, as shown in Figures 4.2 c and 4.2d. The grain-size in the nanostructured samples was much smaller than samples prepared by other approaches, where the grain-size was usually in the order of 10 to 100 μm [19-20].

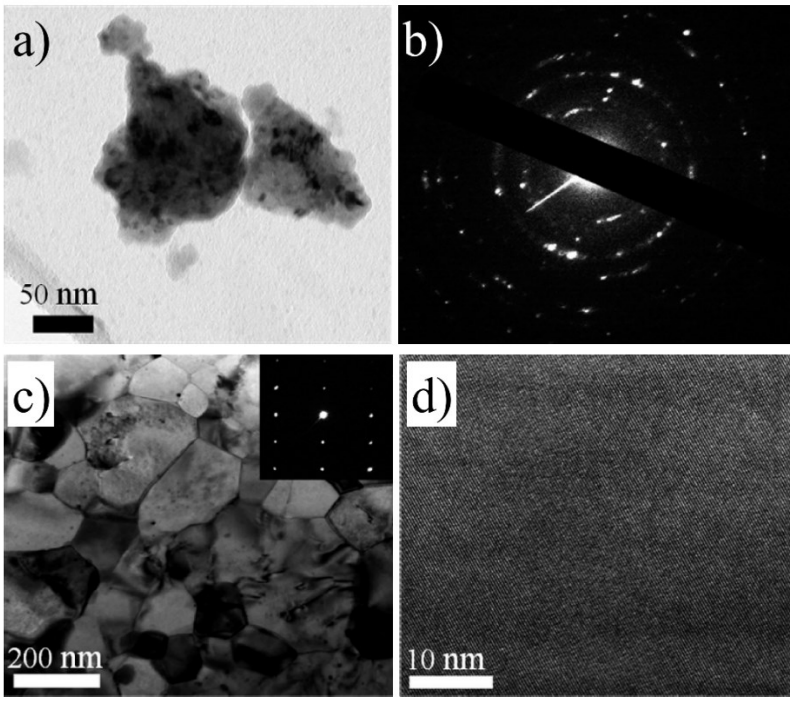

Figure 4.2 TEM characterizations of nanostructured HH [18]. a) TEM image of the powders of $Hf_{0.5}Zr_{0.5}CoSb_{0.8}Sn_{0.2}$ after ball-milling. B) A selected-area-electron-diffraction pattern showing the polycrystalline nature of an agglomerated cluster in a). c) low magnification of the hot-pressed $Hf_{0.5}Zr_{0.5}CoSb_{0.8}Sn_{0.2}$, showing the grain-size of ~200 nm. Inset: SAED of one grain showing single crystallization. d) High-resolution TEM image showing crystallinity at the atomic level.

The compared thermoelectric properties of bulk and nano structured $Hf_{0.5}Zr_{0.5}CoSb_{0.8}Sn_{0.2}$ are shown in Figure 4.3. Higher Seebeck-coefficient and lower electrical conductivity are seen in the nanostructured compounds, as shown in Figures 4.3a and 4.3b. The power factor of nanostructured compounds are slightly higher than the bulk counterpart, as shown in Figure 4.3c. On the other hand, a significant drop of the thermal conductivity occurs in the nanostructured sample, as shown in Figure 4.3d. Figure 4.3e shows a similar decrease of the lattice thermal conductivity (κ_L) after subtracting the

electronic thermal conductivity (κ_e) from the total thermal conductivity (κ_{tot}) using the Wiedemann-Franz relation,

$$\kappa_e = L\sigma T \tag{4.1}$$

where L, σ, and T are the Lorenz number, the electrical conductivity, and the absolute temperature, respectively. The Lorenz number is calculated based on the single parabolic band (SPB) model,

$$L = \left(\frac{k_B}{e}\right)^2 \left[\frac{3F_2(\eta)}{F_0(\eta)} - \left(\frac{2F_1(\eta)}{F_0(\eta)}\right)^2\right] \tag{4.2}$$

$$S = +\left(\frac{k_B}{e}\right)\left[\frac{2F_1(\eta)}{F_0(\eta)} - \eta\right] \tag{4.3}$$

where k_B, e, η, and S are the Boltzmann constant, the carrier charge, the reduced Fermi level, and the Seebeck-coefficient, respectively. The $F_n(\eta)$ are the Fermi integral of order n,

$$F_n(\eta) = \int_0^\infty \frac{\chi^n}{1+e^{\chi-\eta}}\, d\chi \tag{4.4}$$

As a result, Figure 4.3f shows an enhanced ZT from 0.5 to 0.8 by using nanostructuring, as a result of the decreased thermal conductivity.

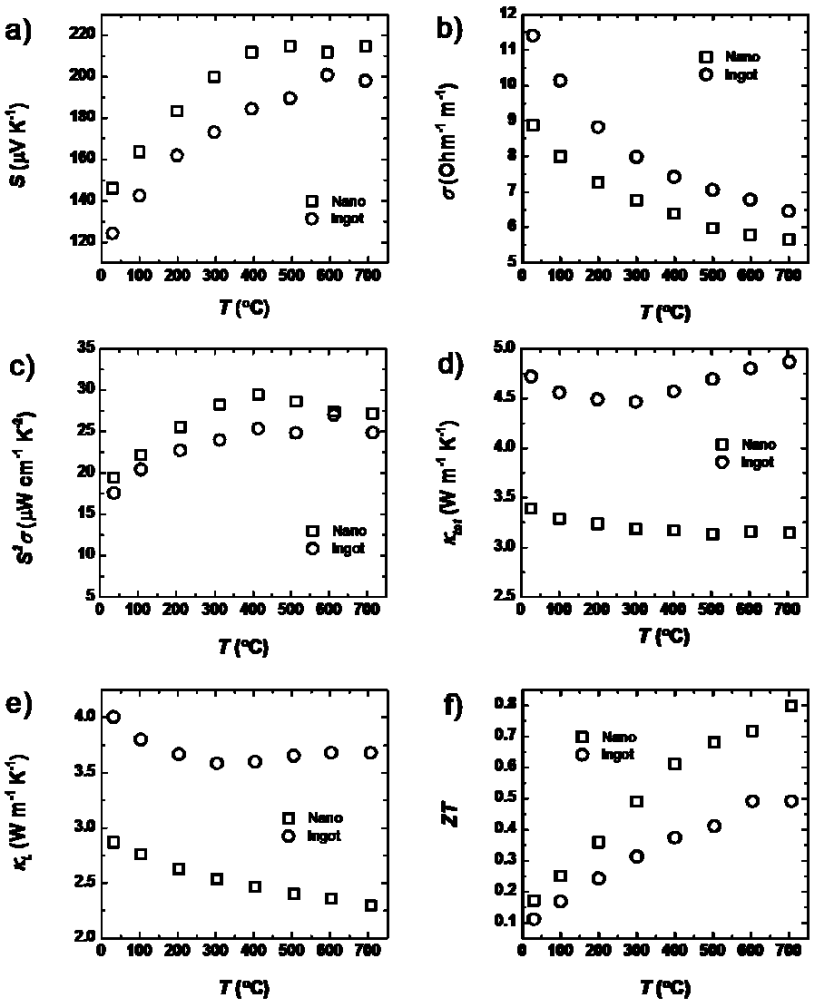

Figure 4.3 Temperature-dependent a) Seebeck-coefficient, b) electrical conductivity, c) power factor, d) total thermal conductivity, e) lattice part of thermal conductivity, and f) *ZT* of ball-milled and hot-pressed sample in comparison to that of the ingot [18].

Following this approach, the thermoelectric (TE) properties of the nanostructured binary $Hf_{1-x}Zr_xCoSb_{0.8}Sn_{0.2}$ and $Hf_{1-y}Ti_yCoSb_{0.8}Sn_{0.2}$, and ternary $Hf_{1-x-y}Zr_xTi_yCoSb_{0.8}Sn_{0.2}$ were subsequently investigated by our group [21, 22]. The peak *ZT* values of several nanostructured $MCoSb_{0.8}Sn_{0.2}$ are shown in Figure 4.4.

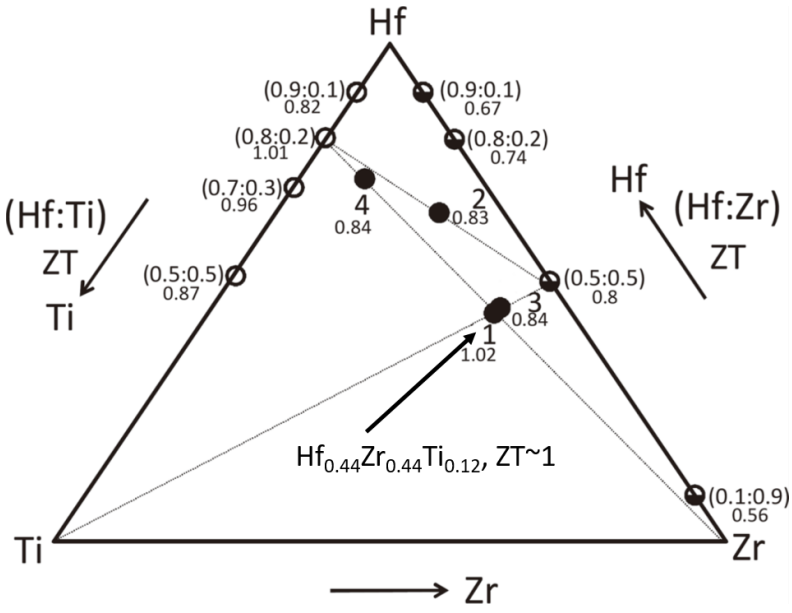

Figure 4.4 (Ti, Zr, Hf)$CoSb_{0.8}Sn_{0.2}$ ternary phase diagram [22]. The binary (Hf:Zr and Hf:Ti) are indicated in the figure and the ternary compositions are: $Hf_{0.44}Zr_{0.44}Ti_{0.12}CoSb_{0.8}Sn_{0.2}$ (1); $Hf_{0.65}Zr_{0.25}Ti_{0.1}CoSb_{0.8}Sn_{0.2}$ (2); $Hf_{0.45}Zr_{0.45}Ti_{0.1}CoSb_{0.8}Sn_{0.2}$ (3); and $Hf_{0.72}Zr_{0.1}Ti_{0.18}CoSb_{0.8}Sn_{0.2}$ (4). The maximum *ZT* value achieved for each composition is also shown underneath the ratio.

As mentioned in section 4.1, the usage of Hf is not preferable due to its low abundance and high price. For example, two compositions, $Hf_{0.8}Ti_{0.2}CoSb_{0.8}Sn_{0.2}$ and $Hf_{0.44}Zr_{0.44}Ti_{0.12}CoSb_{0.8}Sn_{0.2}$ have similar peak *ZT* values ~1. However, the suppressed usage of Hf in the latter yields a 32% drop in the material cost (from ~\$255 kg^{-1} of the former to ~\$174 kg^{-1} of the latter).

In this chapter, I will focus on investigating the TE properties of nanostructured p-type MCoSb by further suppressing Hf usage. As a result, I identified a new composition, $Hf_{0.19}Zr_{0.76}Ti_{0.05}CoSb_{0.8}Sn_{0.2}$, where the usage of Hf was below 0.2 while the *ZT* was kept at ~1.0 at 700 °C. The material cost of this composition dropped to ~\$106 kg^{-1}, a much more affordable cost [23].

4.2 Sample preparation

I kept the amount of Co, Sb, and Sn unchanged based on previously optimization [18, 21, 22] and focused on tuning the amount of Hf, Zr, and Ti with Hf concentration not exceeding 0.25. The previously reported composition, $Hf_{0.44}Zr_{0.44}Ti_{0.12}CoSb_{0.8}Sn_{0.2}$ was also prepared as a reference. The sample process procedures were similar to that of chapter 3. A total number of 25 grams of the elements were arc-melted under an Ar-flowing environment to form ingots. To guarantee the composition homogeneity, the ingots were melted 3-4 times and flipped over each time. The ingots were then milled to nanopowders by a high-energy ball-milling machine (SPEX 8000M Mixer/Mill) in Ar environment for 5 hours. The powders were compacted to disks by a direct current (DC) hot press at 1125 °C and 80 MPa for 2 min.

The thermal conductivity is a multiplication of the thermal diffusivity (D), bulk density, and specific heat (c_p), which were measured by a laser-flash system (LFA 457, Netzsch Instruments, Inc.), an Archimedes' kit, and a high-temperature differential-scanning-calorimetry (DSC) instrument (404 C, Netzsch Instruments, Inc.), respectively. The disks were then cut into bars with dimensions about 2 mm × 2 mm × 12 mm, which were measured by a ZEM-3 machine (ULVAC) to get the electrical resistivity (ρ) and Seebeck-coefficient (S). The uncertainties of the parameters were 2% on ρ, 4% on S, and 7% on κ. Hence the overall uncertainty of ZT was about 17%. Error bars were not used in the plots to increase readability. The best composition was repeated at least three times and the ZT variations were within 5% from run to run.

4.3 Structure characterization

X-ray diffraction (XRD) was employed to determine the phases. The XRD spectra of all the prepared samples in the chapter are shown in Figure 4.5a. Clearly, the formation of pure HH phases was successful.

Both scanning-electron microscope (SEM) (LEO 1525) and transmission-electron microscope (TEM) (JEOL 2100F) were used to check the grain-sizes and microstructures. The SEM and TEM images are shown in Figures 4.5b and 4.5c, respectively. The grain-size of the hot-pressed samples varied from 50 to 250 nm.

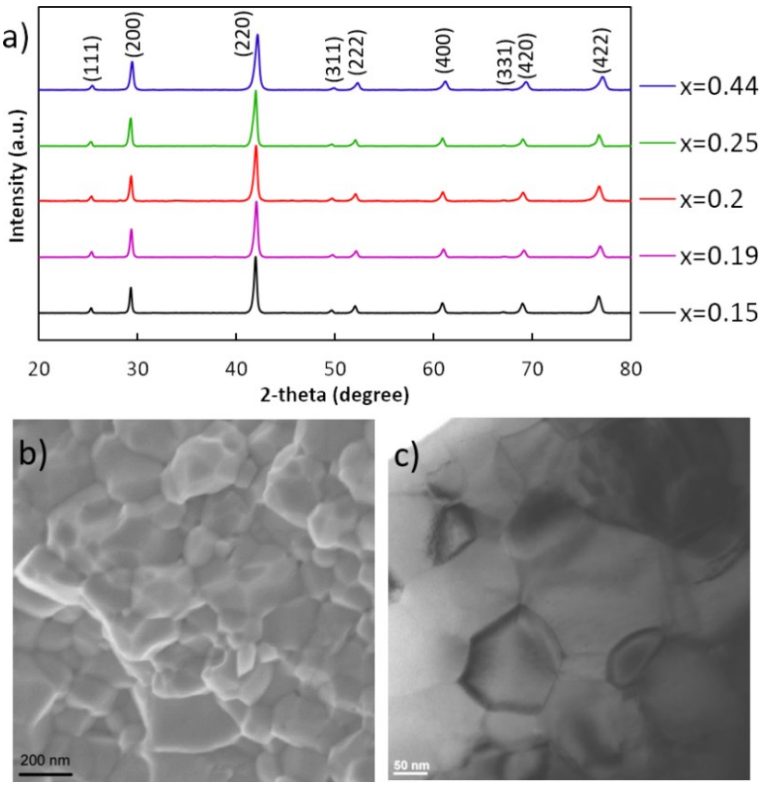

Figure 4.5 a) XRD of $Hf_x(ZrTi)_{1-x}CoSb_{0.8}Sn_{0.2}$, indicating the formation of pure HH phase, b) SEM, and c) TEM image of $Hf_{0.19}Zr_{0.76}Ti_{0.05}CoSb_{0.8}Sn_{0.2}$, which indicate the grain-size is 50–250 nm [23].

4.4 Thermoelectric properties

4.4.1 $Hf_{1-x}Zr_xCoSb_{0.8}Sn_{0.2}$

The temperature-dependent thermoelectric properties of $Hf_{1-x}Zr_xCoSb_{0.8}Sn_{0.2}$ (x=0.15, 0.2 and 0.25) are shown in Figure 4.6.

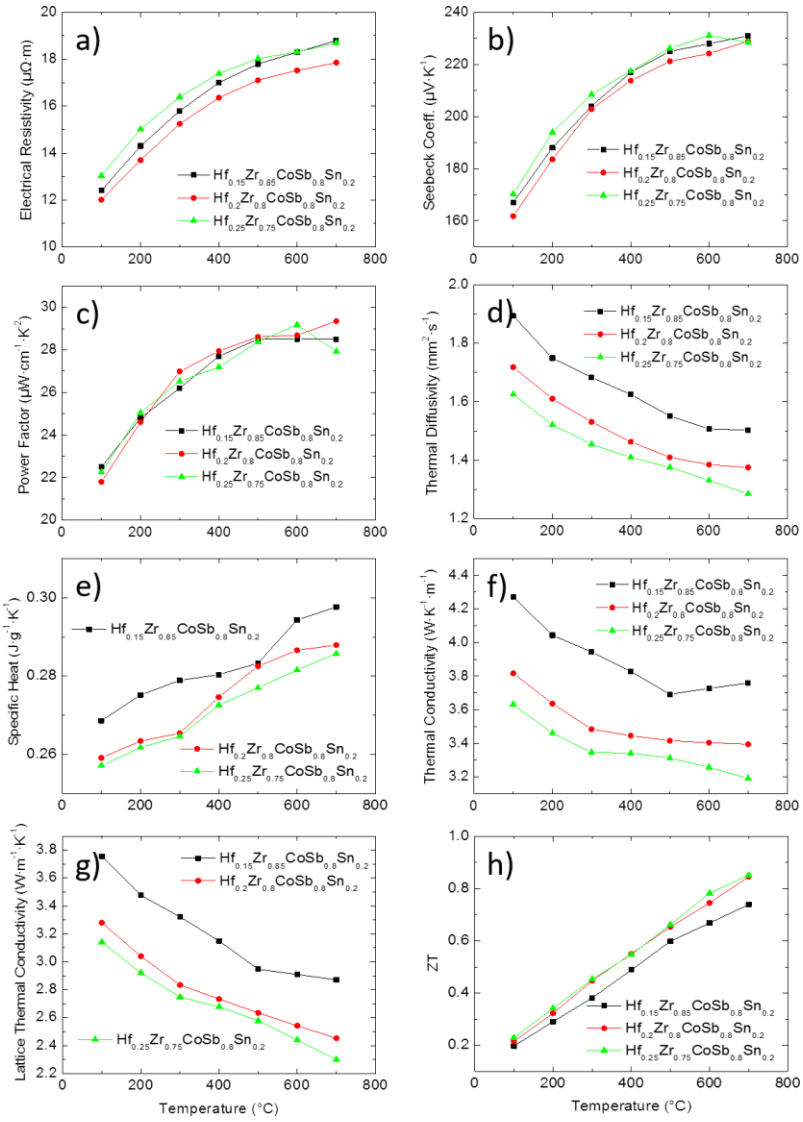

Figure 4.6 Temperature-dependent thermoelectric properties of $Hf_xZr_{1-x}CoSb_{0.8}Sn_{0.2}$ with x = 0.15, 0.2, and 0.25. a) electrical resistivity; b) Seebeck-coefficient; c) power factor; d) thermal diffusivity; e) specific heat, f) thermal conductivity, g) lattice thermal conductivity, and h) *ZT* [23].

Figures 4.6a and 4.6b show that the three compositions (x = 0.15, 0.2, and 0.25) have very similar electrical resistivity and Seebeck-coefficients in the entire temperature range. The result is reasonable since the heavily doped element Sn, at the Sb site, has a fixed concentration in all the compositions, leading to an almost identical nominal carrier concentrations, hence neither the resistivity nor the Seebeck-coefficient of each composition varied significantly from each other. Therefore, as shown in Figure 4.6c, similar power factors were observed for the three compositions. On the other hand, based on the thermal diffusivity and specific heat, as shown in Figures 4.6d and 4.6e, respectively, I found a lowest thermal conductivity with x = 0.25 among all the three compositions, which was the result of relatively stronger alloying effect by increased mass disorder. However, the attenuation of the alloying effect with increasing x was also observed since the thermal conductivity difference between x = 0.2 and x = 0.25 is much smaller than that between x = 0.15 and x = 0.2 (Figure 4.6f). I also estimated the lattice thermal conductivity by subtracting the electronic contribution using the Wiedemann-Franz relation (Eq. (4.1)). As shown in Figure 4.6g, the saturation of alloying effect was observed with x increase from 0.2 to 0.25, which was consistent with the calculated result by Shiomi *et al.* [24] using Green-Kubo method. Finally, I found a similar peak *ZT* reaching 0.85 with x = 0.2 and 0.25 at 700 °C (Figure 4.6h). Considering my purpose of decreasing the Hf usage, the composition $Hf_{0.2}Zr_{0.8}CoSb_{0.8}Sn_{0.2}$ was used for subsequent studies.

4.4.2 $Hf_{0.19}Zr_{0.76}Ti_{0.05}CoSb_{0.8}Sn_{0.2}$

Based on the results on $Hf_{0.2}Zr_{0.8}CoSb_{0.8}Sn_{0.2}$ and $Hf_{0.8}Ti_{0.2}CoSb_{0.8}Sn_{0.2}$, where the best *ZT*s appeared with Hf:Zr ratio of 1:4 and Hf:Ti of 4:1, I specifically came up with the

following composition where the Hf:Zr ratio is 1:4, and the Hf:Ti ratio is 4:1. This yielded $Hf_{0.19}Zr_{0.76}Ti_{0.05}CoSb_{0.8}Sn_{0.2}$. The corresponding results, along with the results of $Hf_{0.2}Zr_{0.8}CoSb_{0.8}Sn_{0.2}$ and $Hf_{0.44}Zr_{0.44}Ti_{0.12}CoSb_{0.8}Sn_{0.2}$ are shown in Figure 4.7.

Figure 4.7a shows that the electrical resistivity of the three compositions are quite different: the one with x = 0.19 had the lowest electrical resistivity and the one with x = 0.44 had the highest value. Moreover, the Seebeck-coefficients were similar, as shown in Figure 4.7b. As a result, $Hf_{0.19}Zr_{0.76}Ti_{0.05}CoSb_{0.8}Sn_{0.2}$ possessed a higher power factor than the others in the entire temperature range (Figure 4.7c). On the other hand, based on the diffusivity (Figure 4.7d) and specific heat (Figure 4.7e), the thermal conductivity of $Hf_{0.19}Zr_{0.76}Ti_{0.05}CoSb_{0.8}Sn_{0.2}$ was similar to that of $Hf_{0.2}Zr_{0.8}CoSb_{0.8}Sn_{0.2}$ (Figure 4.7f). In addition, due to the stronger alloying effect, the lattice thermal conductivity decreased with higher Ti concentration (Figure 4.7g). Although $Hf_{0.44}Zr_{0.44}Ti_{0.12}CoSb_{0.8}Sn_{0.2}$ possessed much lower thermal conductivity, as a result of heavier average atomic mass, its *ZT* did not show any advantages compared to $Hf_{0.19}Zr_{0.76}Ti_{0.05}CoSb_{0.8}Sn_{0.2}$ within the entire temperature range (Figure 4.7 h), due to the higher power factor of the latter (Figure 4.7c). For $Hf_{0.19}Zr_{0.76}Ti_{0.05}CoSb_{0.8}Sn_{0.2}$, the peak *ZT* was about 1.0 at 700 °C, which is similar to that of $Hf_{0.44}Zr_{0.44}Ti_{0.12}CoSb_{0.8}Sn_{0.2}$.

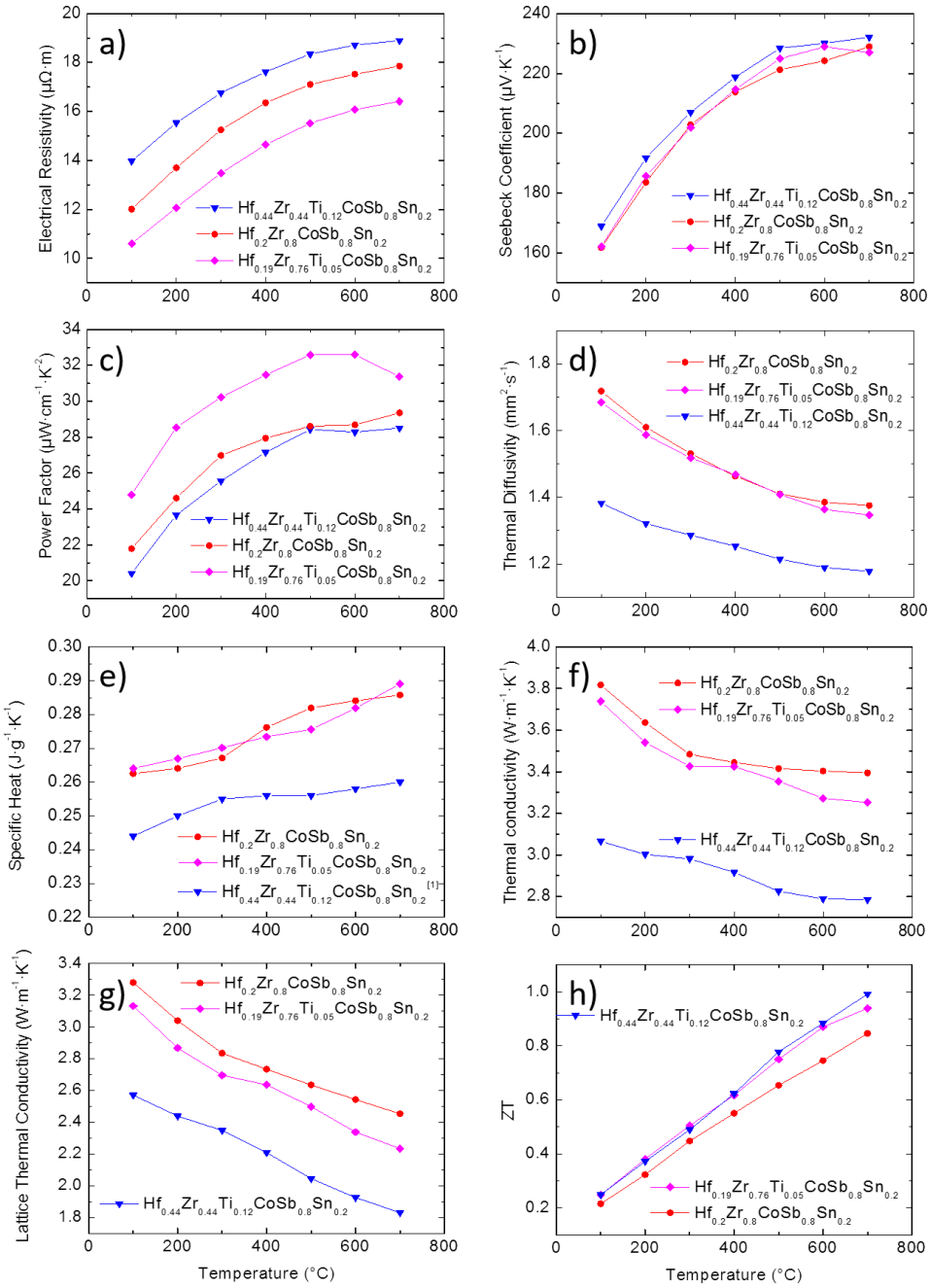

Figure 4.7 Temperature-dependent thermoelectric properties of $Hf_{0.44}Zr_{0.44}Ti_{0.12}CoSb_{0.8}Sn_{0.2}$, $Hf_{0.2}Zr_{0.8}CoSb_{0.8}Sn_{0.2}$ and $Hf_{0.19}Zr_{0.76}Ti_{0.05}CoSb_{0.8}Sn_{0.2}$. a) electrical resistivity; b) Seebeck-coefficient; c) power factor; d) thermal diffusivity; e) specific heat, f) thermal conductivity, g) lattice thermal conductivity, and h) *ZT* [23].

4.4.3 Comparison of thermoelectric properties of nanostructured $MCoSb_{0.8}Sn_{0.2}$

Figures 4.8a-f compare the thermoelectric properties of nanostructured binary (Hf/Zr)$CoSb_{0.8}Sn_{0.2}$ (red symbols), binary (Hf/Ti)$CoSb_{0.8}Sn_{0.2}$ (blue symbols), and ternary (Hf/Zr/Ti)$CoSb_{0.8}Sn_{0.2}$ (green symbols) that were prepared by our group. Figures 4.8a-b show the Seebeck-coefficient and the electrical conductivity. In a general trend, the more Hf usage, the lower Seebeck-coefficient in each of the three systems, as shown in Figure 4.8a. This suggested a higher carrier concentration with more Hf usage, as further experimentally observed in the (Hf/Ti)$CoSb_{0.85}Sb_{0.15}$ systems [25]. Thus, higher Hf concentrations yielded higher doping efficiency since the nominal dopant concentration was identical amongst all the compositions. On the other hand, as shown in Figure 4.8b, the lowest electrical conductivity was observed in the binary (Hf/Ti)$CoSb_{0.8}Sn_{0.2}$ system due to the larger mass difference between Hf and Ti. In addition, the ternary (Hf/Zr/Ti)$CoSb_{0.8}Sn_{0.2}$ system had relatively higher electrical conductivity. The combined electrical conductivity and the Seebeck-coefficient gave the power factor, as shown in Figure 4.8c. The power factor of the binary (Hf/Ti)$CoSb_{0.8}Sn_{0.2}$ was the lowest due to the low electrical conductivity. Similarly, both the total and lattice thermal conductivity of the binary (Hf/Ti)$CoSb_{0.8}Sn_{0.2}$ were also lower due to the large mass difference between Hf and Ti, as shown in Figures 4.8d and 4.8e. Consequently, peak *ZT* values ~1 were obtained at 700-800 °C in several compositions, such as $Hf_{0.8}Ti_{0.2}CoSb_{0.8}Sn_{0.2}$, $Hf_{0.44}Zr_{0.44}Ti_{0.12}CoSb_{0.8}Sn_{0.2}$ and $Hf_{0.19}Zr_{0.76}Ti_{0.05}CoSb_{0.8}Sn_{0.2}$ (Figure 4.8f).

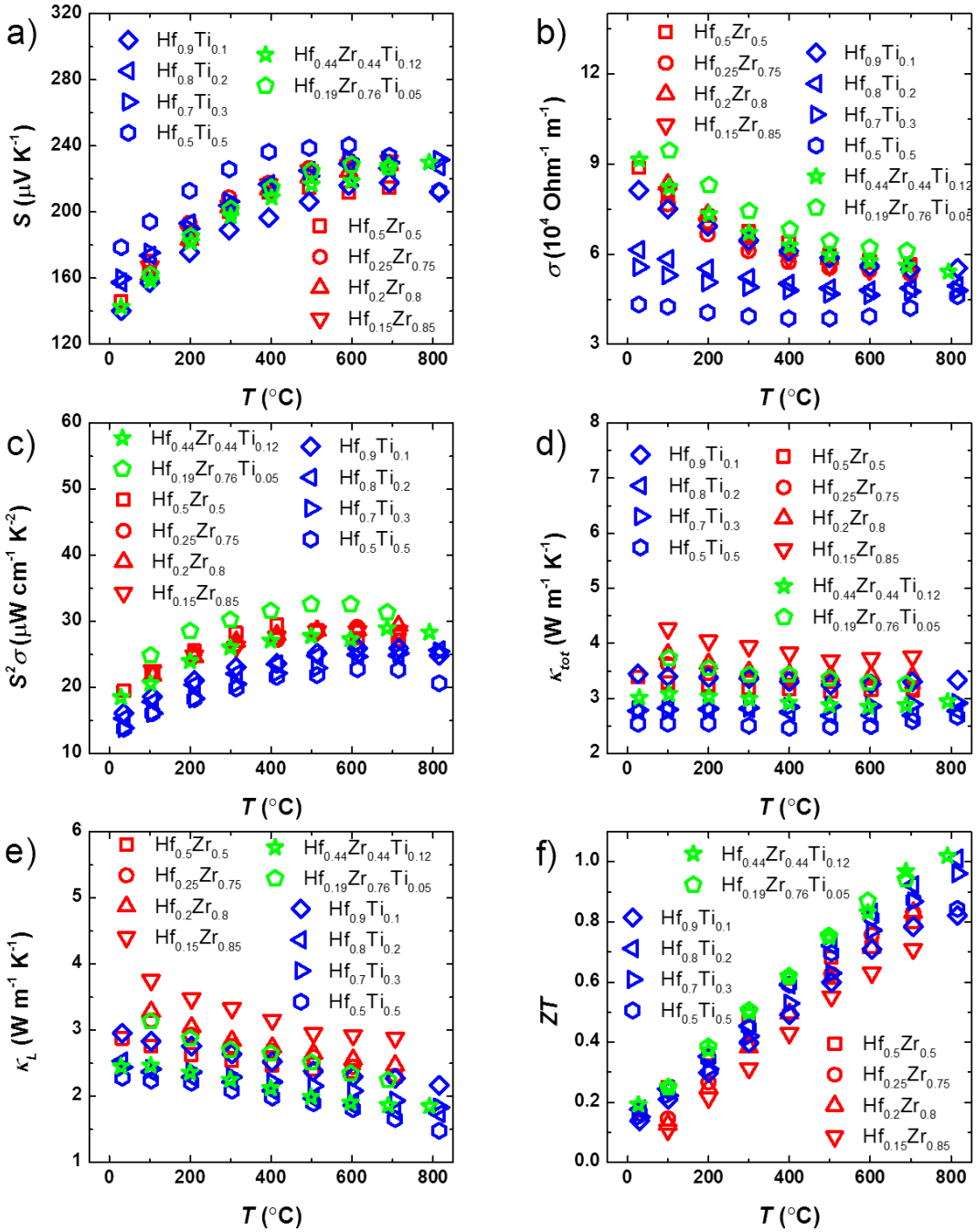

Figure 4.8 Temperature-dependent a) Seebeck-coefficient, b) electrical conductivity, c) power factor, d) total thermal conductivity, e) lattice part of thermal conductivity, and f) *ZT* of nanostructured *M*$CoSb_{0.8}Sn_{0.2}$ [18, 21-23].

4.4.4 Power generation

In order to compare the performance of TE materials, output power generation and its maximum conversion efficiency (η_{max}) were calculated by Eq. (4.5)

$$\eta = \frac{T_H - T_C}{T_H} \cdot \frac{\sqrt{1+\overline{ZT}}-1}{\sqrt{1+\overline{ZT}}+\frac{T_C}{T_H}} \quad (4.5)$$

where T_H, T_C, and $\overline{T}$ is the hot-side, the cold-side, and the average temperature, respectively. Eq. (4.5) is derived from temperature independent TE properties. However, this gave a reasonable agreement only when the temperature difference is moderate, meanwhile the nonlinearity of the TE properties with the temperature could generate large errors. The peak working temperature of HH is around 700 °C, which might generate temperature gradients as large as 600 °C/2 mm (or higher). Thus, Eq. (4.5) cannot predict its performance precisely. In this work, numerical analysis [26, 27] was carried out to obtain the power generation and efficiency according to temperature-dependent TE properties, where the Thomson effect is also taken into account.

A general form of energy balance of a TE leg at one-dimensional heat flow is

$$\frac{d}{dx}\left(\kappa(x)\frac{dT(x)}{dx}\right) + j^2\rho(x) - jT(x)\frac{dS(x)}{dx} = 0 \quad (4.6)$$

with j being the current density, the terms on the left-hand side of Eq. (4.6) represent heat conduction, Joule heat, and Thomson heat, respectively, and no heat loss is considered. In order to solve the differential equation by accounting the temperature dependence of TE properties, a finite difference method was used. A TE leg was divided into n nodes, and a

central difference scheme was applied to approximate a temperature and the TE properties at each node. This yielded a linear relation between nodes as shown in Eq. (4.7)

$$\frac{\kappa_{i+1}-\kappa_i}{2\delta x}\frac{T_{i+1}-T_i}{2\delta x}+\kappa_i\frac{T_{i+1}+T_{i-1}-2T_i}{(\delta x)^2}+j^2\rho_i-jT_i\frac{S_{i+1}-S_i}{2\delta x}=0 \qquad (4.7)$$

where, i = 2, 3, ..., n-1 since T_1 and T_n are known as T_H and T_C, respectively. By iterating until solutions converge, the numerical analysis was finalized in which the convergence condition of the temperature and electric current in this calculation was 10^{-10}.

Figures 4.9a and 4.9b show a validation of the numerical analysis and an effect based on TE properties as a function of temperature where T_H varied up to 700 °C (923 K) while T_C is kept at 50 °C (323 K). The analytically simplified calculation had an agreement with the numerical solutions within 2% when ΔT is smaller than 175 °C, but it was overestimated by more than 6% at ΔT = 650 °C. The output power generation of $Hf_{0.19}Zr_{0.76}Ti_{0.05}CoSb_{0.8}Sn_{0.2}$ was improved by 16.7% at ΔT = 650 °C and a = 2 mm as compared with $Hf_{0.44}Zr_{0.44}Ti_{0.12}CoSb_{0.8}Sn_{0.2}$, and it was linearly proportional to the cross-section area of TE leg (Figure 4.9a) while the conversion efficiency had less than 1% difference from each other through the entire temperature range (Figure 4.9b), where the maximum efficiency of each material is not a function of the leg dimension a.

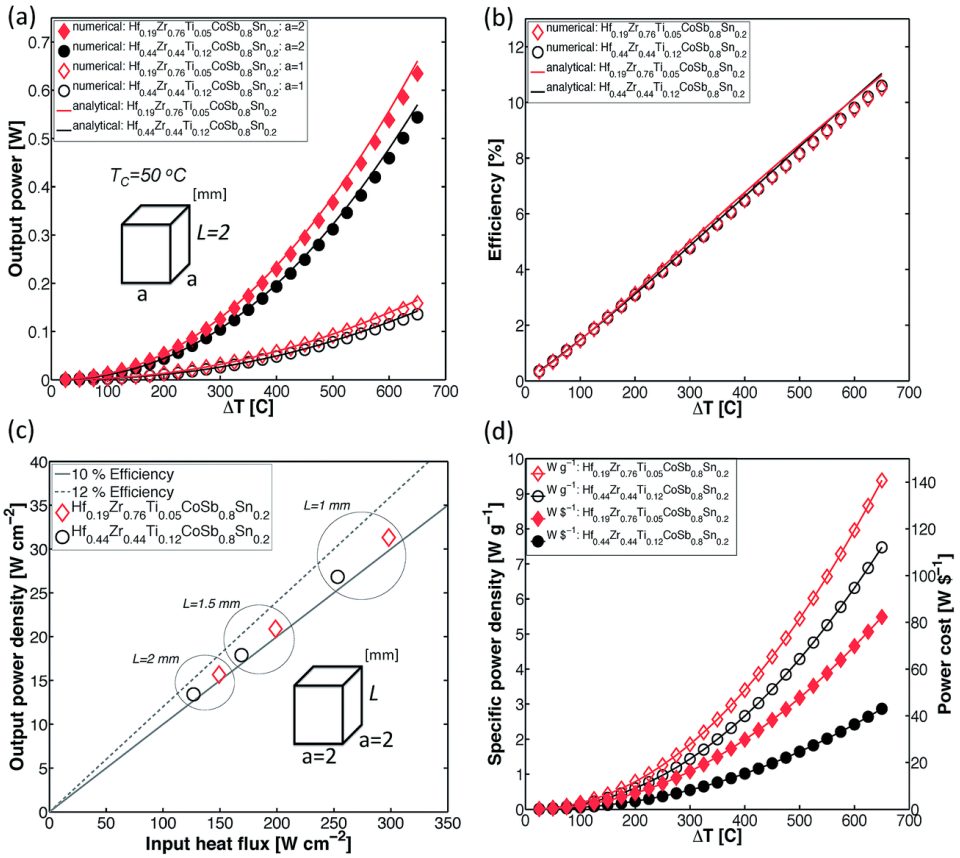

Figure 4.9 Calculated output-power density and conversion efficiency dependence of T_H (up to 700 °C) with T_C fixed at 50 °C of $Hf_{0.44}Zr_{0.44}Ti_{0.12}CoSb_{0.8}Sn_{0.2}$ and $Hf_{0.19}Zr_{0.76}Ti_{0.05}CoSb_{0.8}Sn_{0.2}$: comparison of temperature-dependent a) output-power density and b) efficiency; c) input and output power relation with the leg length; d) temperature-dependent specific power density, W g^{-1}, and power cost, W per $ [23].

The ratio of output power to input heat is plotted in Figure 4.9c according to various TE leg lengths. Shorter TE legs require more heat-flux to generate a certain temperature difference, and gives rise to larger amount of output power due to its lower electrical resistance of TE leg. In all cases, $Hf_{0.19}Zr_{0.76}Ti_{0.05}CoSb_{0.8}Sn_{0.2}$ required more heat across TE leg and generated larger electrical power as compared to $Hf_{0.44}Zr_{0.44}Ti_{0.12}CoSb_{0.8}Sn_{0.2}$ because the thermal and electrical conductivities of $Hf_{0.19}Zr_{0.76}Ti_{0.05}CoSb_{0.8}Sn_{0.2}$ was larger

through all temperature range. Figure 4.9d shows the effect of the Hf reduction on the output-power density and power cost. The use of less Hf element reduced mass density of the alloy as well as the material cost. The hollow marker represents the specific power density, W g^{-1}, and the solid symbols are for the power cost, W per $. As mentioned, output power of $Hf_{0.19}Zr_{0.76}Ti_{0.05}CoSb_{0.8}Sn_{0.2}$ was improved due to the higher power factor. In addition, The specific power density of $Hf_{0.19}Zr_{0.76}Ti_{0.05}CoSb_{0.8}Sn_{0.2}$ was increased by 25% along with 7% reduced mass density, and 40% reduction of total cost of $Hf_{0.19}Zr_{0.76}Ti_{0.05}CoSb_{0.8}Sn_{0.2}$, which resulted in an 91% increase of the electric power generation per dollar by $Hf_{0.19}Zr_{0.76}Ti_{0.05}CoSb_{0.8}Sn_{0.2}$. Therefore, the new composition $Hf_{0.19}Zr_{0.76}Ti_{0.05}CoSb_{0.8}Sn_{0.2}$ was much more favorable for practical applications due to the higher power factor.

4.5 Summary

Aiming at decreasing the amount of Hf, I found a good *ZT* ~0.85 at 700 °C in $Hf_{0.2}Zr_{0.8}CoSb_{0.8}Sn_{0.2}$. By further replacing some Ti at the Hf/Zr site, I established a new composition of $Hf_{0.19}Zr_{0.76}Ti_{0.05}CoSb_{0.8}Sn_{0.2}$ to reach a *ZT* of ~1.0 at 700 °C with the Hf:Ti ratio at 4:1 and Hf:Zr ratio at 1:4. The new composition exhibited similar *ZT* to the previously reported composition, $Hf_{0.44}Zr_{0.44}Ti_{0.12}CoSb_{0.8}Sn_{0.2}$, yielding similar heat-to-power conversion efficiency. On the other hand, the new compound used much less Hf which is an expensive, low-abundance element. These findings enabled us to significantly decrease the price of the materials and increase the output power without losing any TE-conversion efficiency compared to other reported good p-type compositions. This would

accelerate the commercialization of half-Heusler materials for large-scale applications in waste-heat recovery.

4.6 References

[1] R. He, *et al.*, Studies on mechanical properties of thermoelectric materials by nanoindentation, *Phys. Status Solidi A* **212**, 2191–2195 (2015).

[2] S. Chen and Z. F. Ren, Recent progress of half-Heusler for moderate temperature thermoelectric applications, *Mater. Today* **16**, 387-395 (2013).

[3] USGS, *Scientific Investigations Report* 2012–5188 (2013).

[4] T. Graf, *et al.*, Simple rules for the understanding of Heusler compounds, *Prog. in Solid State Chem.* **39**, 1-50 (2011).

[5] Serdar Öğüt and Karin M. Rabe, Band gap and stability in the ternary intermetallic compounds NiSnM (M=Ti,Zr,Hf): A first-principles study, *Phys. Rev. B* **51**, 10443 (1995).

[6] I. Galanakis and P. Mavropoulos, Spin-polarization and electronic properties of half-metallic Heusler alloys calculated from first principles. *J. Phys.: Condens. Matter* **19** 315213 (2007).

[7] F.G. Aliev, *et al.*, Gap at the Fermi level in the intermetallic vacancy system RBiSn(R=Ti,Zr,Hf), *Z. Phys. B: Condens. Matter* **75**, 167 (1989).

[8] F.G. Aliev, *et al.*, Narrow band in the intermetallic compounds MNiSn (M=Ti, Zr, Hf), *Z. Phys. B: Condens. Matter* **80**, 353 (1990).

[9] J. Pierre, *et al.*, Properties on request in semi-Heusler phases, *J. Alloys Comp.* **101**, 262-263 (1997).

[10] T. Sekimoto, *et al.*, Thermoelectric properties of Sn-doped TiCoSb half-Heusler compounds, *J. Alloys Compd.* 407, 326-329 (2006).

[11] T. Wu, *et al.*, Thermoelectric properties of p-type Fe-doped TiCoSb half-Heusler compounds, *J. Appl. Phys.* 102, 103705 (2007).

[12] T. Sekimoto, *et al.*, High-thermoelectric figure of merit realized in p-type half-Heusler compounds: $ZrCoSn_xSb_{1-x}$, *Jpn. J. Appl. Phys.* **46,** 673-675 (2007).

[13] S. R. Culp, *et al.*, (Zr,Hf)Co(Sb,Sn) half-Heusler phases as high-temperature (> 700 °C) p-type thermoelectric materials, *Appl. Phys. Lett.* **93**, 022105 (2008).

[14] B. Poudel, *et al.*, High-thermoelectric performance of nanostructured bismuth antimony telluride bulk alloys, *Science* **320**, 634-638 (2008).

[15] V. Ponnambalam, *et al.*, Thermoelectric properties of p-type half-Heusler alloys $Zr_{1-x}Ti_xCoSn_ySb_{1-y}$ ($0.0<x<0.5$; Y=0.15 and 0.3), *J. Appl. Phys.* **103**, 063716 (2008).

[16] S. J. Poon, *et al.*, Half-Heusler phases and nanocomposites as emerging high-ZT thermoelectric materials, *J. Mater. Res.* **26**, 2795–2802 (2011).

[17] C. C. Hsu, *et al.*, Effect of the $Zr_{0.5}Hf_{0.5}CoSb_{1-x}Sn_x/HfO_2$ half-Heusler nanocomposites on the ZT value, *J. Alloys Compd.* **597**, 217-222 (2014).

[18] X. Yan, *et al.*, Enhanced thermoelectric figure of merit of p-type half-Heuslers, *Nano Lett.* **11**, 556-560 (2011).

[19] T. Sekimoto, *et al.*, Annealing effect on thermoelectric properties of TiCoSb half-Heusler compound, *J. Alloy Compd.* **394**, 122-125 (2005).

[20] G. Joshi, *et al.*, Enhancement in thermoelectric figure-Of-Merit of an n-type half Heusler compound by the nanocomposite approach, *Adv. Energy. Mater.* **1**, 643-647 (2011).

[21] X. Yan, *et al.*, Stronger phonon scattering by larger differences in atomic mass and size in p-type half-Heuslers $Hf_{1-x}Ti_xCoSb_{0.8}Sn_{0.2}$, *Energy Environ. Sci.* **5,** 7543 (2012).

[22] X. Yan, *et al.*, Thermoelectric property study of nanostructured p-type half-Heuslers (Hf,Zr,Ti)$CoSb_{0.8}Sn_{0.2}$, *Adv. Energy Mater.* **3,** 1195–1200 (2013).

[23] R. He, *et al.*, Investigating the thermoelectric properties of p-type half-Heusler $Hf_x(ZrTi)_{1-x}CoSb_{0.8}Sn_{0.2}$ by reducing Hf concentration for power generation, *RSC Adv.* **4,** 64711–64716 (2014).

[24] J. Shiomi, K. Esfarjani and G. Chen, Thermal conductivity of half-Heusler compounds from first-principles calculations, *Phys. Rev. B* **84**, 104302 (2011).

[25] E. Rausch, *et al.*, Fine tuning of thermoelectric performance in phase-separated half-Heusler compounds, *J. Mater. Chem. C* **3,** 10409-10414 (2015).

[26] G. D. Mahan, Inhomogeneous thermoelectrics, *J. Appl. Phys.* **70**, 4551-4554 (1991).

[27] T. P. Hogan and T. Shih, in *Thermoelectrics Handbook: Macro to Nano,* ed. D. M. Rowe, CRC Press, (2006).

Chapter 5 Investigating the Thermoelectric Properties of NbCoSn-based Half-Heusler

A part of this chapter contains our previously published work

R. He, *et al.*, Enhanced thermoelectric properties of n-type NbCoSn half-Heusler by improving phase purity*, APL Mater.* **4**, 104804 (2016).

5.1 Introduction

Although the p-type $Hf_{0.19}Zr_{0.76}Ti_{0.05}CoSb_{0.8}Sn_{0.2}$ has improved cost performance, as I introduced in the last chapter, there are ~63% of the total material cost come from the usage of hafnium (Hf). Thus, it's important to find materials that completely eliminate Hf. There are hundreds of half-Heusler compounds, and their phase stabilities, band structures, and thermoelectric (TE) properties that were investigated through theoretical calculations [1, 2]. These calculations predicted many stable HH compounds with promising TE properties. However, as the TE technique is highly application orientated, the preferable TE materials should employ elements that are nontoxic and earth-abundant. Moreover, good TE materials are usually semiconductors, therefore, the valance-electron-count of undoped half-Heusler compounds has to be 8 or 18 to locate the Fermi level inside the band gap [3-5]. These requirements are satisfied by several half-Heusler compounds including the widely studied MCoSb and MNiSn (M=Hf, Zr, Ti), as well as some less studied compounds including NbCoSn, NbFeSb, *etc*. In this, and subsequent chapters, I will introduce the thermoelectric properties of the NbCoSn-based and NbFeSb-based half-Heusler compounds.

NbCoSn is a half-Heusler compound with 18 valance electrons, and its thermoelectric properties were studied by several groups. Undoped NbCoSn is intrinsically n-type. Kiruma *et al.* reported the effects of increasing Co concentration up to $NbCo_{1.1}Sn$ and obtained a Seebeck-coefficient of about -250 μV K^{-1} and peak *ZT* of 0.3 at ~1000 K in $NbCo_{1.05}Sn$ [6]. Kawaharada *et al.* reported the TE properties with partial substitution of Nb by Hf, Ti, and Mo; and substitution of Sn by Sb [7, 8]. They found Hf and Ti were weak p-type dopants and the resulting Seebeck-coefficients were very low. Meanwhile, Mo and Sb were strong n-type dopants. Similar study was also performed by Ono *et al*. and a *ZT* ~0.3 was reported for $NbCoSn_{0.9}Sb_{0.1}$ [9].

However, these reported compositions possessed many secondary phases such as $NbCo_2Sn$, Sn, Nb_3Sn, *etc.*, which deteriorated TE performance, especially the electron transport properties. To investigate the properties of compositions with better purity, I studied $NbCoSn_{1-x}Sb_x$ with x=0-0.15 using our arc-melting, ball-milling, and hot-pressing procedure. As a result, the purity was improved when comparing to other approaches. Electron transport significantly benefited from phase purification, leading to simultaneous enhancement of electrical conductivity and the Seebeck-coefficient. The highest power factor obtained by this method was ~34 μW cm^{-1} K^{-2}, which was 80% higher than that of Ono's report. As a result, the peak *ZT* reached ~0.6 in $NbCoSn_{0.9}Sb_{0.1}$ [10]. Even though the *ZT* was still lower than 1.0 like other good HfNiSn-based n-type HHs, the calculated specific power cost ($ W^{-1}) was much lower due to the elimination of Hf in the composition.

The band structure of NbCoSn indicated that the p-type NbCoSn could possibly possess better TE properties than the n-type compounds. Thus, the experimental attempts to synthesis p-type would also be discussed.

5.2 Experimental procedure

5.2.1 Sample preparation

The samples in this chapter were prepared similar to chapter 4. A total 10 grams of elements (Nb pieces 99.99% and Co shavings 99.9%, Atlantic Metals and Alloy; Sn granules 99.9% and Sb broken rod 99.9%, Alfa Aesar) for each batch were weighed according to the stoichiometry. In order to reduce Sb evaporation, I first melted Sb with Sn to form alloys, then the other elements were added and melted together 3-4 times, and the samples were flipped over each time to improve uniformity. The ingots were then crushed into nano-powders by the high-energy ball-milling (SPEX 8000M Mixer/Mill) machine for 2 hours. The powders were then consolidated into disks by hot-pressing at 1000 °C and 80 MPa for 2 minutes.

5.2.2 Structure characterization

A PANalytical multipurpose diffractometer with an X'celerator detector (PANalytical X'Pert Pro) was used to characterize the phases. Morphology and elemental distributions of the samples were characterized by a scanning-electron microscope (SEM, LEO 1525) and an energy dispersive x-ray spectroscope (EDS), respectively. An Electron Probe Micro-Analysis (EPMA, JXA-8600) was used to characterize the elemental ratio of

the final products. A transmission-electron microscope (TEM, JEOL 2010F) was used to observe the detailed microstructures.

Due to the similar atomic size and masses, all samples possessed similar densities (Table 5.1). Figure 5.1 shows the X-ray diffraction (XRD) spectrum of $NbCoSn_{1-x}Sb_x$ with x=0, 0.01, 0.02, 0.05, 0.1, and 0.15. All samples showed pure half-Heusler (HH) phase, indicating good solubility of Sb at the Sn site. Also, the energy-dispersive spectroscopy (EDS) mapping on a polished surface of $NbCoSn_{0.9}Sb_{0.1}$ indicated uniform elemental distribution (Figure 5.2), no phase segregation was observed. The Electron Probe Micro-Analysis (EPMA) results are shown in Table 5.1 with the actual composition of the final product close to the nominal composition.

Note that there were still some minor impurities that could not be detected by XRD or EDS. Figures 5.3b and 5.3c are the low and high-resolution TEM images of $NbCoSn_{0.9}Sb_{0.1}$, which showed some minor defects or precipitates. Thus, completely removing the impurities was unrealistic. However, the phase purity was much better than the previously reports. Figure 5.3d is the zoom-in high-resolution TEM image, which showed a lattice constant of ~5.94 Å. The inset in Figure 5.3d shows the Fast-Fourier-Transform (FFT) image.

Figure 5.3a shows the scanning electron microscopic (SEM) image of a sample with nominal composition $NbCoSn_{0.9}Sb_{0.1}$, demonstrating very good crystallinity with a grain-size varying between ~250 to ~800 nm.

Table 5.1 Nominal, actual compositions and measured mass densities of $NbCoSn_{1-x}Sb_x$ by Electron Probe Micro-Analysis (EPMA) [10].

Nominal	EPMA	Density (g cm^{-3})
NbCoSn	$NbCo_{1.02}Sn_{0.98}$	8.35
$NbCoSn_{0.99}Sb_{0.01}$	$NbCo_{1.01}Sn_{0.98}Sb_{0.01}$	8.48
$NbCoSn_{0.98}Sb_{0.02}$	$NbCo_{1.00}Sn_{0.97}Sb_{0.02}$	8.48
$NbCoSn_{0.95}Sb_{0.05}$	$NbCo_{1.02}Sn_{0.94}Sb_{0.04}$	8.48
$NbCoSn_{0.9}Sb_{0.1}$	$NbCo_{1.03}Sn_{0.88}Sb_{0.09}$	8.44
$NbCoSn_{0.85}Sb_{0.15}$	$NbCo_{1.01}Sn_{0.84}Sb_{0.14}$	8.52

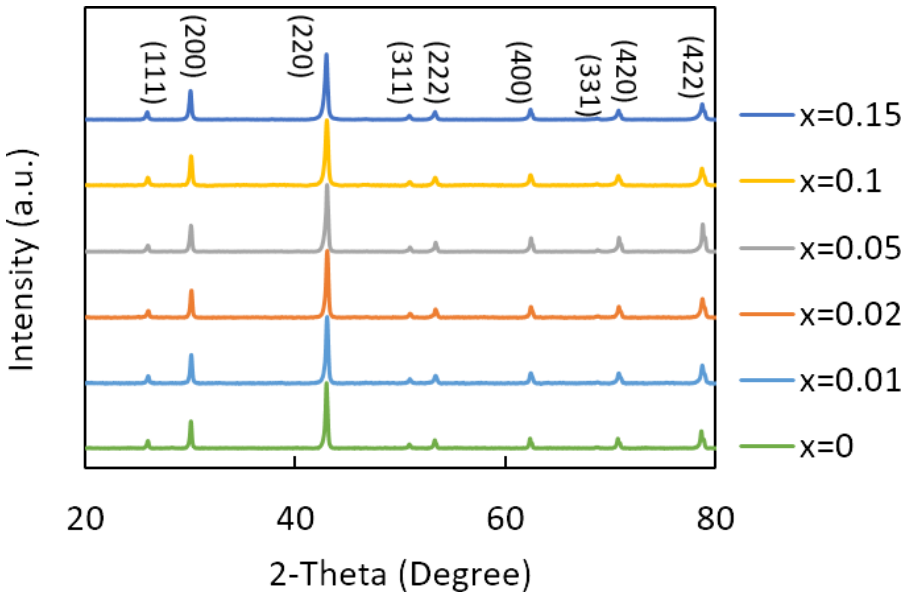

Figure 5.1 X-ray diffraction (XRD) spectra of $NbCoSn_{1-x}Sb_x$ with x = 0, 0.01, 0.02, 0.05, 0.1, and 0.15 [10].

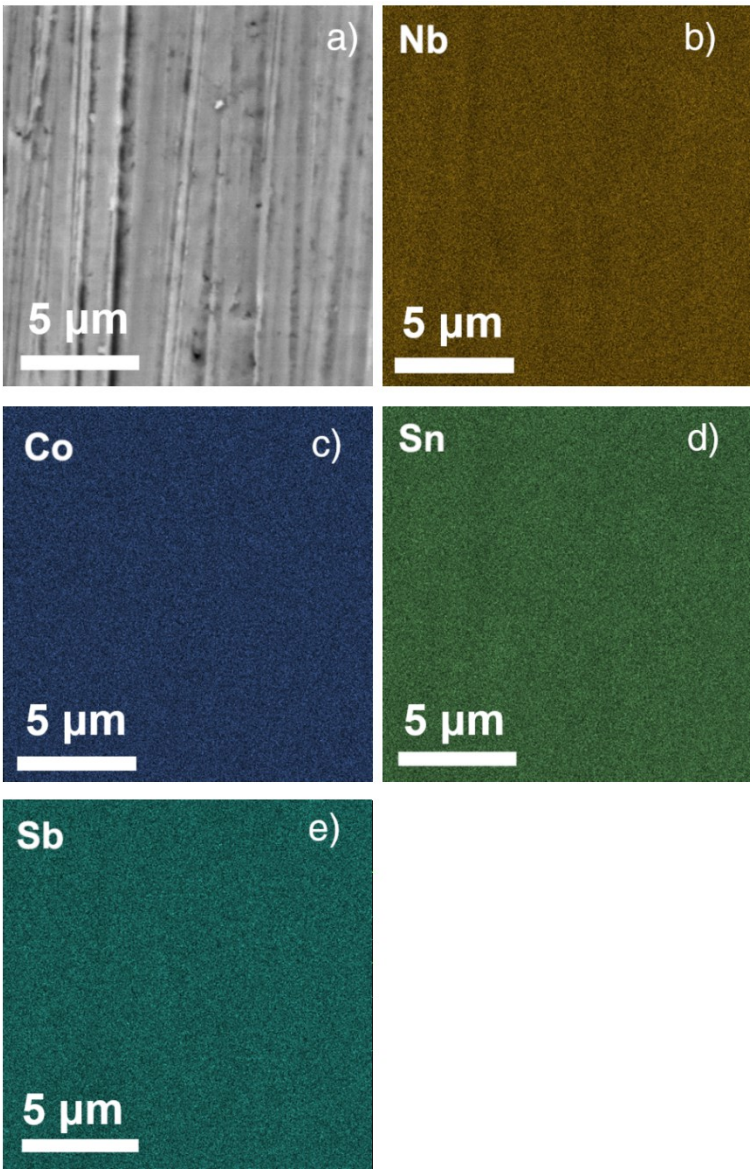

Figure 5.2 a) SEM image of polished surface of $NbCoSn_{0.9}Sb_{0.1}$ and elemental distribution of b) Nb, c) Co, d) Sn, and e) Sb [10].

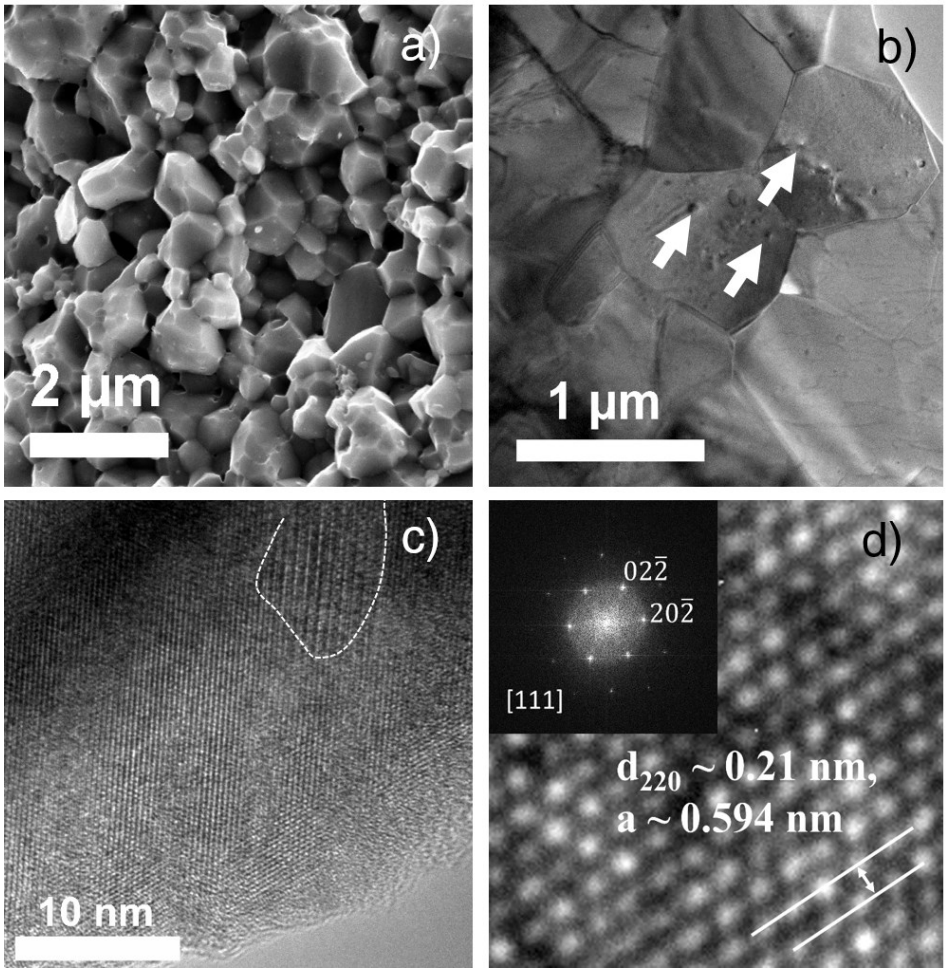

Figure 5.3 a) SEM image of $NbCoSn_{0.9}Sb_{0.1}$, indicating grain-size from ~250 to ~800 nm, b) low-resolution and c) high-resolution TEM image of $NbCoSn_{0.9}Sb_{0.1}$. The white arrows in b) and white curve in c) indicate there are still minor impurities. d) Lattice constant of ~5.94 Å is for $NbCoSn_{0.9}Sb_{0.1}$ and the inset in d) is its FFT image [10].

5.2.3 Thermoelectric properties measurement

The thermal conductivity is the multiplication of thermal diffusivity, (D), specific heat, (c_P), and density, which were measured by a laser-flash system (LFA457, Netzsch), a differential-scanning calorimeter (DSC, 404 C), and an Archimedes' kit, respectively. Bar shaped samples (~2 × 2 × 12 mm^3) were used to measure electrical conductivity and Seebeck-coefficient on a ZEM-3 machine (ULVAC). Carrier concentrations, (n_H), were

measured using a physical properties measurement system (PPMS, Quantum Design) under ±3 Tesla magnetic fields. The Hall mobility, μ_H, was calculated based on $\mu_H = \sigma R_H$, where R_H is the Hall coefficient. The uncertainties for electrical conductivity, the Seebeck-coefficient, and thermal conductivity were 2%, 4%, and 7%, respectively. The combined uncertainties for power factor and *ZT* were 10% and 17%, respectively. The best composition was repeated for at least three times, and the resulting *ZT* variations were within 5% from run to run. To increase the readability, I did not plot error bars on the curves.

5.3 Results and discussion

5.3.1 Thermoelectric properties

Figures 5.4a-h show the thermoelectric properties of $NbCoSn_{1-x}Sb_x$ with x up to 0.15. For comparison, I also plotted the literature data of $NbCoSn_{0.9}Sb_{0.1}$ [9] (thick black line) and NbCoSb [11] (dotted line), the latter is an unusual half-Heusler thermoelectric material that has 19 valance electrons. Figures 5.4a and 5.4b show the electric conductivity and the Seebeck-coefficient, respectively. Higher Sb concentration resulted in higher conductivity and lower Seebeck-coefficient. For $NbCoSn_{0.9}Sb_{0.1}$, both the conductivity and Seebeck-coefficient were higher than Ono's reported values [9], which resulted in higher power factors (Figure 5.4c) with a peak value of ~34 μW cm^{-1} K^{-2} in $NbCoSn_{0.9}Sb_{0.1}$ at 873 K, ~80% higher than Ono's result.

Figures 5.4d-f show the total thermal conductivity (κ_{tot}), specific heat (c_P), and thermal diffusivity (*D*), respectively. Note that the thermal conductivity of the base

composition NbCoSn is ~8.2 W m^{-1} K^{-1} at room temperature (Figure 3d), but even 1% Sb doping increased the value to ~9.7 W m^{-1} K^{-1}. The mechanism of the enhancement is not completely clear since the increased electronic contribution cannot account for all of the increase. For samples with more Sb doping, the thermal conductivity kept decreasing as a result of the decreased lattice thermal conductivity (κ_L) (Figure 5.4g).

Note that the decrease in κ_L was not due to point-defect scattering, because the κ_L of ternary NbCoSb [11] was smallest among all the $NbCoSn_{1-x}Sb_x$ samples. Possibly, the electron-phonon interaction dominates the phonon scattering because of the increased carrier concentration. Another possibility is a stronger phonon-phonon interaction with higher concentration of Sb. The phonon-phonon interaction is related to the chemical bonds. As analyzed by Graf, *et al.* [3], usually the 18 valance-electron-count (VEC) half-Heuslers are stable because of the full occupation of bonding states and the emptiness of anti-bonding states. Meanwhile, Sb doping introduced extra electrons that occupy the anti-bonding states, thus weakening the bonding interaction, and further leading to a decreased phonon group velocity (v) since phonon propagation relies on chemical bonds. Under the Umklapp process, the phonon relaxation time is related with phonon group velocity [12],

$$\tau_U \sim \frac{v^3}{T} \tag{5.1}$$

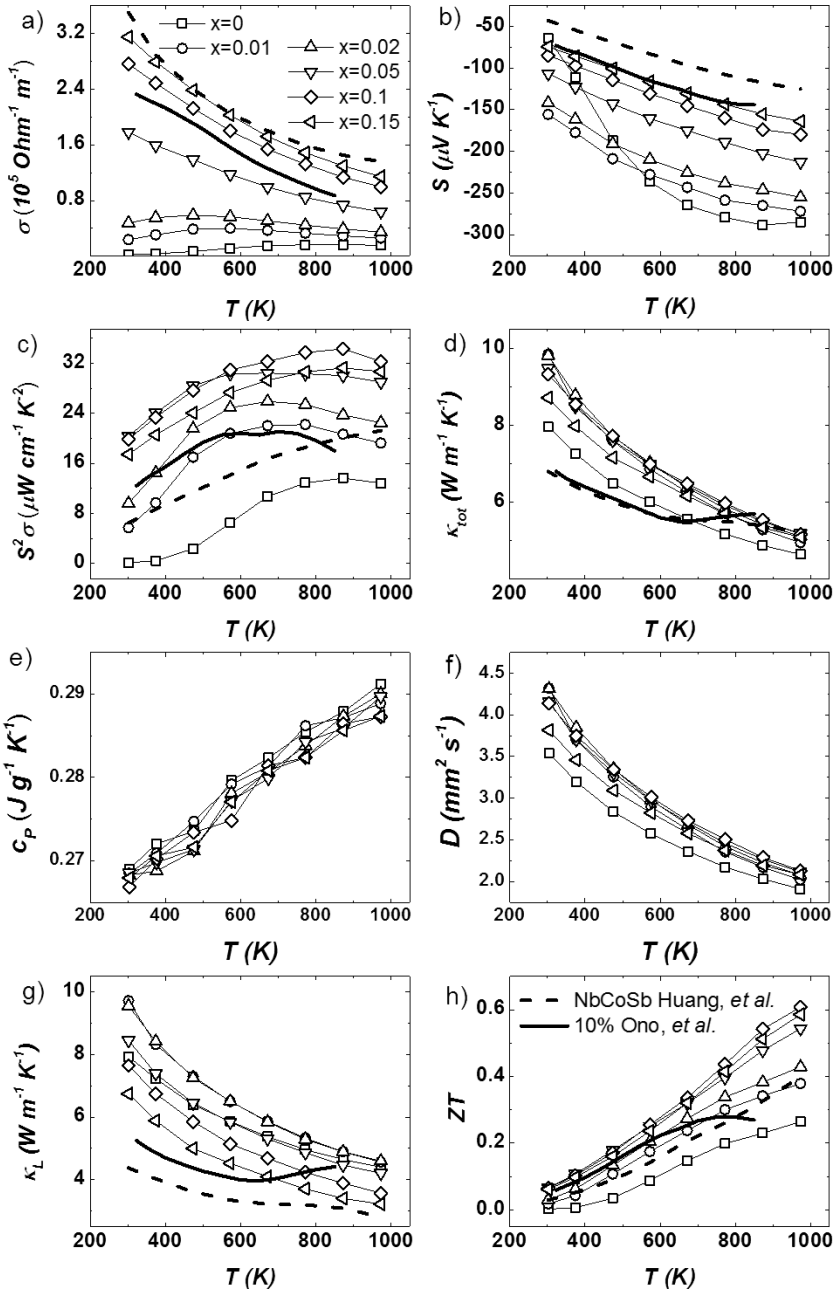

Figure 5.4 Thermoelectric properties: a) electrical conductivity, b) Seebeck-coefficient, c) power factor, d) total thermal conductivity, e) specific heat, f) thermal diffusivity, g) lattice thermal conductivity, and h) *ZT* of $NbCoSn_{1-x}Sb_x$ with x = 0, 0.01, 0.02, 0.05, 0.1, and 0.15. The reference data of $NbCoSn_{0.9}Sb_{0.1}$ and NbCoSb are taken from [9] (thick black line) and [11] (dashed line), respectively [10].

Therefore, phonon relaxation time would decrease due to stronger phonon-phonon interaction. As a result, the *ZT* values reached ~0.6 (Figure 5.4h) in $NbCoSn_{0.9}Sb_{0.1}$, which was about double of the *ZT* value reported by Ono *et al*. with the same composition [9].

5.3.2 Anisotropy thermoelectric properties

Usually in nanostructured half-Heusler compounds, there are no anisotropic transport properties for electrons and phonons considering the high-symmetry crystal structure and nano-sized polycrystalline microstructure. However the experimental confirmation of isotropic transport was scarce. Thus, I specifically tested the thermoelectric properties of $NbCoSn_{0.9}Sb_{0.1}$ along directions perpendicular and parallel to the hot-pressing direction. The TE properties are shown in Figure 5.5.

There were some minor differences along different measurement directions which, however, more likely originated from batch difference and measurement error. Therefore, the anisotropy was negligible when analyzing the transport properties in nanostructured half-Heusler compounds.

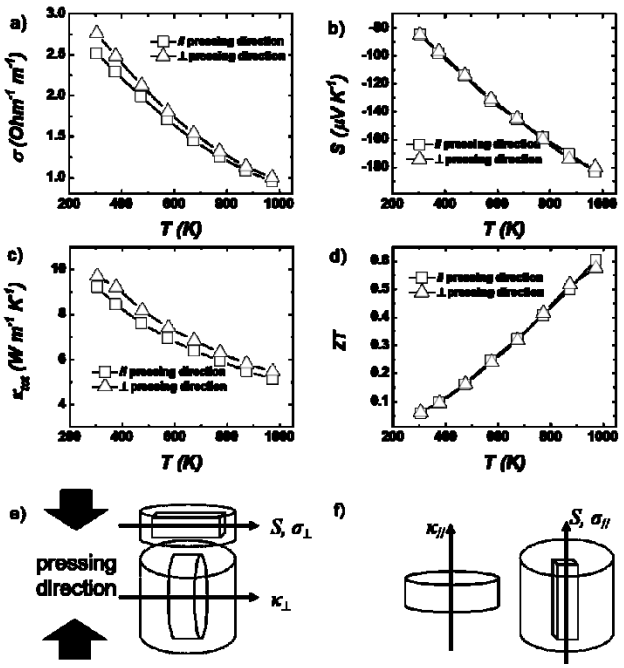

Figure 5.5 TE properties a) electrical conductivity, b) Seebeck-coefficient, c) thermal conductivity and d) *ZT* of $NbCoSn_{0.9}Sb_{0.1}$ parallel and perpendicular to the hot-pressing temperature. e) and f) schematically show the measurement direction perpendicular and parallel to the hot-pressing directions [10].

5.3.3 Hall measurement

The relation of the Hall concentration (n_H, solid square) and mobility (μ_H, open circle) with Sb concentration are shown in Figure 5.6a. The measured carrier concentration increased almost linearly with Sb concentration for all the Sb partially substituted compositions; however, the undoped composition had n_H value even higher than that of 2% Sb doping. This could be qualitatively explained by the two-band model [13], in which n_H could be written as,

$$n_H = \frac{1}{qR_H} \tag{5.2}$$

$$R_H = \frac{1}{q}\frac{p-nb^2}{(p+nb)^2} \quad (5.3)$$

where q is positive value of carrier charge, R_H is the Hall coefficient, p and n are the real concentration of holes and electrons, b is defined as the carrier mobility ratio between electrons and holes, usually in the order of unity. Thus,

$$n_H = \frac{(p+nb)^2}{p-nb^2} \quad (5.4)$$

For heavily doped semiconductors (SC), it satisfies $p >> n$ or $n >> p$, thus $n_H \approx p$ or n. However, for low level doping around the intrinsic region, the values of p and n are close to each other, thus the denominator in the expression of n_H are small, yielding an artificially large n_H.

With Sb concentrations increasing from 0.05 to 0.15, n_H increased almost linearly to > 2×10^{21} cm^{-3}, which was quite high for TE materials. Huang *et al.* reported an even higher carrier concentration of ~6×10^{21} cm^{-3} for NbCoSb [11]. On the other hand, the measured carrier mobility increased significantly from ~0.2 to ~11 cm^2 V^{-1} s^{-1} with Sb concentration up to 0.05, then it decreased to ~8.8 cm^2 V^{-1} s^{-1} with Sb concentration reached 0.15 (Figure 5.6a right). Note that the Hall mobility (μ_H) with Sb concentration below 0.05 was underestimated due to, as explained, the overestimation of Hall concentration (n_H). By fitting with the Pisarenko relation for the compositions with $x \geq 0.05$, the electron density-of-state (DOS) effective mass (m^*) gradually increased from 5.7 m_0 to 7.1 m_0 with Sb concentration up to 1.0 (Figure 5.6b). The enhanced effective mass accounted for the decreased carrier mobility when Sb concentration was higher than 0.05 (Figure 5.6a).

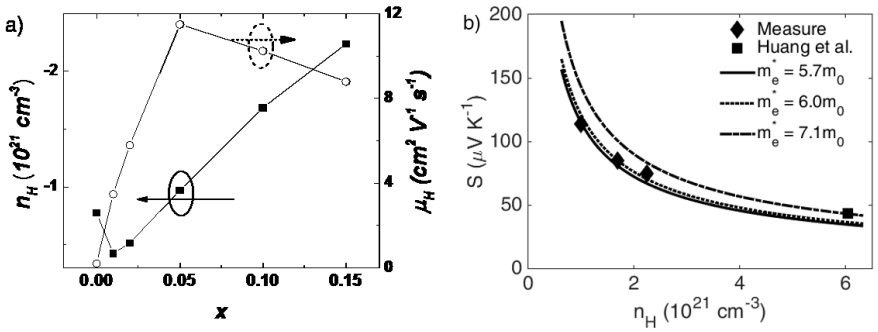

Figure 5.6 a) Carrier concentration (left vertical axis) and mobility (right vertical axis) of $NbCoSn_{1-x}Sb_x$. b) Seebeck-coefficient vs. carrier concentration, showing an increased effective mass from 5.7 m_0 to 7.1 m_0 with higher concentration of Sb [10].

5.3.4 Power generation

Even though the NbCoSn-based HH compounds did not have the same *ZT* as the HfNiSn-based n-type HHs, such as $Hf_{0.25}Zr_{0.75}NiSn_{0.99}Sb_{0.01}$ [14], it was more affordable due to the elimination of Hf. Based on the elemental prices listed in chapter 4 (Table 4.1), the calculated prices were \$126 kg^{-1} for $Hf_{0.25}Zr_{0.75}NiSn_{0.99}Sb_{0.01}$ but only \$26 kg^{-1} for $NbCoSn_{0.9}Sb_{0.1}$, which was only ~1/5, thus a much lower \$ W^{-1} was expected for NbCoSn.

Kim, *et al.* [15] proposed equations for calculating the output-power density (ω) and maximum conversion efficiency (η_{max}) of a TE material under a large temperature gradient,

$$\boldsymbol{\omega} = \frac{(PF)_{eng}(T_H - T_C)}{L}\frac{m_{opt}}{(1+m_{opt})^2} \tag{5.5}$$

$$\boldsymbol{\eta_{max}} = \eta_C \frac{\sqrt{1+(ZT)_{eng}(\alpha_1/\eta_C)}-1}{\alpha_0\sqrt{1+(ZT)_{eng}(\alpha_1/\eta_C)}+\alpha_2} \tag{5.6}$$

$$(PF)_{eng} = \frac{\left(\int_{T_C}^{T_H} S(T)dT\right)^2}{\int_{T_C}^{T_H} \rho(T)dT} \quad (5.7)$$

$$(ZT)_{eng} = \frac{(PF)_{eng}}{\int_{T_C}^{T_H} \kappa(T)dT}(T_H - T_C) \quad (5.8)$$

$$m_{opt} = \sqrt{1 + (ZT)_{eng}\alpha_1\eta_c^{-1}} \quad (5.9)$$

$$\eta_C = \frac{T_H - T_C}{T_H} \quad (5.10)$$

$$\alpha_i = \frac{S_{T_H}(T_H - T_C)}{\int_{T_C}^{T_H} S(T)dT} - \frac{\int_{T_C}^{T_H} \tau(T)dT}{\int_{T_C}^{T_H} S(T)dT} W_T\eta_C - iW_J\eta_C \quad (i = 0, 1, 2) \quad (5.11)$$

$$\tau = T\frac{dS(T)}{dT} \quad (5.12)$$

$$W_T = \frac{\int_{T_C}^{T_H}\int_{T}^{T_H} \tau(T)dTdT}{\Delta T \int_{T_C}^{T_H} \tau(T)dT} \quad (5.13)$$

$$W_J = \frac{\int_{T_C}^{T_H}\int_{T}^{T_H} \rho(T)dTdT}{\Delta T \int_{T_C}^{T_H} \rho(T)dT} \quad (5.14)$$

Based on Eqs. (5.5)-(5.14), I calculated the conversion efficiency and output-power density assuming a leg length of 2 mm and cold-side temperature of 323 K (Figure 5.7). Not surprisingly, both the power density (Figure 5.7a) and the conversion efficiency (Figure 5.7b) of $NbCoSn_{0.9}Sb_{0.1}$ were lower than $Hf_{0.25}Zr_{0.75}NiSn_{0.99}Sb_{0.01}$ [14], but the specific power cost ($ W^{-1}) was much lower as well (Figure 5.7c). When T_H is 873 K, the power cost was ~0.012 $ W^{-1} for $Hf_{0.25}Zr_{0.75}NiSn_{0.99}Sb_{0.01}$, but ~0.004 $ W^{-1} for $NbCoSn_{0.9}Sb_{0.1}$. The power cost of $NbCoSn_{0.9}Sb_{0.1}$ was also much lower than that of the MCoSb based p-type material introduced in chapter 4: the power costs were 0.024 $ W^{-1}

for $Hf_{0.44}Zr_{0.44}Ti_{0.12}CoSb_{0.8}Sn_{0.2}$, and 0.012 \$ W^{-1} for $Hf_{0.19}Zr_{0.76}Ti_{0.05}CoSb_{0.8}Sn_{0.2}$ (with T_H at 873 K), respectively. Thus, NbCoSn could be competitive with HfNiSn-based n-type half-Heusler for large-scale applications.

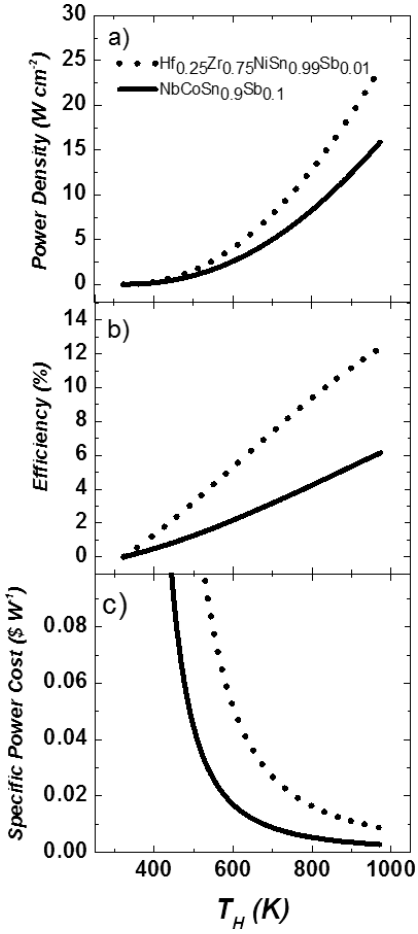

Figure 5.7 The calculated a) power density, b) efficiency, and c) specific power cost (\$ W^{-1}) of $Hf_{0.25}Zr_{0.75}NiSn_{0.99}Sb_{0.01}$ and $NbCoSn_{0.9}Sb_{0.1}$ [10].

5.3.5 Band structure of NbCoSn

The band structure of the ternary NbCoSn were also obtained from density-functional-theory (DFT) calculations within the generalized gradient approximation (GGA) in the Perdew-Burke-Ernzerhof (PBE) form for the exchange-correlation function [16].

The electronic transport coefficients were computed by solving the Boltzmann transport equation for electrons using the intrinsic contribution from the electron-phonon interaction to the electron-relaxation time calculated within the electron-phonon-averaged (EPA) approximation [17].

Figures 5.8a-b show the band structure and density of states (DOS) calculated using density functional theory (DFT). The base composition NbCoSn was semiconductor, but the samples $NbCoSn_{1-x}Sb_x$ behaved like metal due to heavy doping Sb on Sn site. The indirect band gap is around 1 eV with the conduction band minima (CBM) at X points and the valence band maxima (VBM) at L and W points. The CBM consists of two bands thus giving a high-valley degeneracy ($N_v = 6$). High-valley degeneracy was widely proven to be beneficial to thermoelectric performance [18-23].

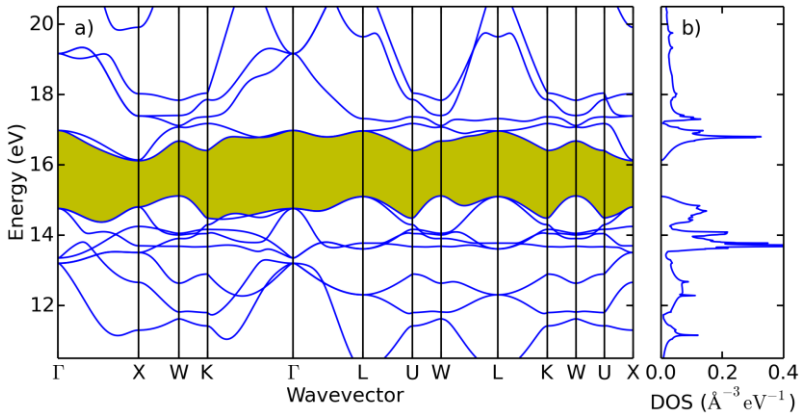

Figure 5.8 a) Band structure and b) density of states (DOS) of NbCoSn calculated within DFT using the PBE exchange-correlation function. The yellow region indicates the band gap [10].

More interestingly, I noticed an even higher valley degeneracy at the VBM, where the L and W points both contributed to the hole transport, thus higher TE performance of

p-type NbCoSn was expected. However, the experimental results showed that the p-type materials possessed much poorer TE properties than the n-type counterparts, as shown below.

5.3.6 P-type NbCoSn

With similar sample preparation procedures, several dopants were tried to make p-type NbCoSn, such as Ti substitution at the Nb site, and Fe substitution at the Co site. The TE properties were poor due to the low values of electrical conductivity and the Seebeck-coefficient. The thermoelectric properties of both Ti and Fe doped samples are shown in Figure 5.9.

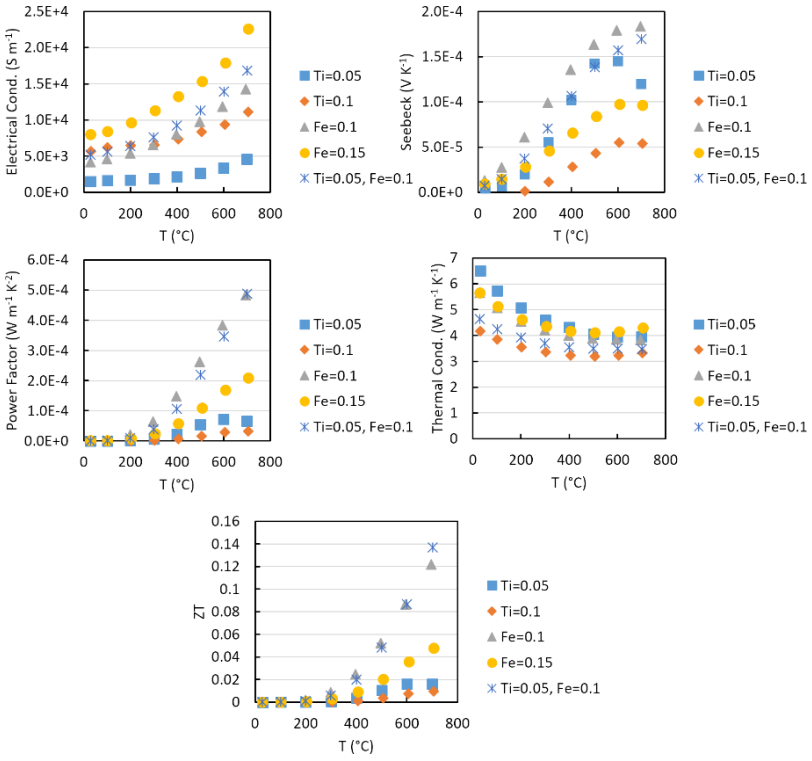

Figure 5.9 Thermoelectric properties of p-type NbCoSn with Ti and Fe substitution at Nb and Co sites.

For all the p-type compositions, the electrical conductivity were much lower than the n-type counterparts. Meanwhile, the increasing trend of the electrical conductivity with temperature indicated that the incomplete ionization of the dopants. Besides, the Seebeck-coefficient increased with temperature, indicating the gradual transition from the two-band transport to the single-band transport, which further confirmed the increased degree of dopant ionization. As a result, both the power factor and *ZT* values were very low.

Except for Ti and Fe, many other dopants were also attempted to get good p-type NbCoSn. Here is the list of elements I tried:

Dopants at the Nb site: Ti, Zr, Hf, Y, La, Yb, Eu, Ca, Mg, and Li.

Dopant at the Co site: Fe.

Dopants at the Sn site: B and Al.

However these elements failed in making good p-type NbCoSn. Some dopants yielded similar phenomena as Ti and Fe, and the others could not be doped into the lattice. Therefore, the NbCoSn compounds might not be a good p-type TE material.

5.4 Summary

With improved phase purity, Sb doping effectively enhanced the thermoelectric performance of NbCoSn-based n-type half-Heusler. Both the electrical conductivity and the Seebeck-coefficient were higher, so was the power factor. The peak power factor was ~34 μW cm^{-1} K^{-2} at 873 K in $NbCoSn_{0.9}Sb_{0.1}$, which was 80% higher than the previously reported data with the same composition. A peak *ZT* of ~0.6 was achieved at 973 K, which

was about double of the previously reported value with the same composition. Importantly, the specific power cost of NbCoSn-based HH was much lower than the HfNiSn-based HH.

5.5 References

[1] J. Carrete, *et al.*, Finding unprecedentedly low-thermal-conductivity half-Heusler semiconductors via high-throughput materials modeling, *Phys. Rev. X* **4**, 011019 (2014).

[2] J. Yang, *et al.*, Evaluation of half-Heusler compounds as thermoelectric materials based on the calculated electrical transport properties, *Adv. Energy. Mater.* **18**, 2880–2888 (2008).

[3] T. Graf, *et al.*, Simple rules for the understanding of Heusler compounds, *Prog. in Solid State Chem.* **39**, 1-50 (2011).

[4] F. Casper, *et al.*, Half-Heusler compounds: novel materials for energy and spintronic applications, *Semicond. Sci. Technol.* **27**, 063001 (2012).

[5] J. W. Simonson and S. J. Poon, Electronic structure of transition metal-doped XNiSn and XCoSb (X= Hf, Zr) phases in the vicinity of the band gap, *J. Phys.: Condens. Matter* **20**, 255220 (2008).

[6] Y. Kimura, Y. Tamura and T. Kita, Thermoelectric properties of directionally solidified half-Heusler compound NbCoSn alloys, *Appl. Phys. Lett.* **92**, 012105 (2008).

[7] Y. Kawaharada, *et al.*, High temperature thermoelectric properties of $CoNb_{1-x}Hf_xSn_{1-y}Sb_y$ half-Heusler compounds, *J. Alloys Compd.* **377**, 312-315 (2004).

[8] Y. Kawaharada, *et al.*, High temperature thermoelectric properties of $CoNb_{1-x}M_xSn$ half-Heusler compounds, *J. Alloys Compd.* **384**, 303-307 (2004).

[9] Y. Ono, *et al.*, Thermoelectric properties of NbCoSn-based half-Heusler alloys, *In 25th International Conference on Thermoelectrics*, IEEE 124-127 (2006).

[10] R. He, *et al.*, Enhanced thermoelectric properties of n-type NbCoSn half-Heusler by improving phase purity, *APL Mater.* **4**, 104804 (2016).

[11] L. Huang, *et al.*, A new n-type half-Heusler thermoelectric material NbCoSb, *Mater. Res. Bull.* **70**, 773-778 (2015).

[12] M. Roufosse and P. Klemens, Thermal conductivity of complex dielectric crystals, *Phys. Rev. B.* **7**, 5379-5386 (1973).

[13] V. M. Tuchkevich and V. Y. Frenkel, *Semiconductor Physics*, New York : Consultants Bureau, (1986).

[14] S. Chen, *et al.*, Effect of Hf concentration on thermoelectric properties of nanostructured n-type half-Heusler materials $Hf_xZr_{1-x}NiSn_{0.99}Sb_{0.01}$, *Adv. Energy Mater.* **3**, 1210-1214 (2013).

[15] H. S. Kim, *et al.*, Relationship between thermoelectric figure of merit and energy conversion efficiency, *Proc. Natl. Acad. Sci.*, **112**, 8205-8210 (2015).

[16] J. P. Perdew, K. Burke, and M. Ernzerhof, Generalized gradient approximation made simple, *Phys. Rev. Lett.* **78**, 1396 (1997).

[17] G. Samsonidze and B. Kozinsky, Role of energy dependence of intrinsic electron relaxation time in semiconductors, *arXiv:1511.08115v1* (2015).

[18] C. Fu, *et al.*, Band engineering of high performance p-type FeNbSb based half-Heusler thermoelectric materials for figure of merit zT>1, *Energy Environ. Sci.*, **8**, 216-220 (2015).

[19] W. Liu, *et al.*, Convergence of conduction bands as a means of enhancing thermoelectric performance of n-type $Mg_2Si_{1-x}Sn_x$ solid solutions, *Phys. Rev. Lett.* **108**, 166601 (2012).

[20] Y. Pei, *et al.*, Convergence of electronic bands for high performance bulk thermoelectrics, *Nature* **473**, 66-69 (2011).

[21] L. Zhao, *et al.*, All-scale hierarchical thermoelectrics: MgTe in PbTe facilitates valence band convergence and suppresses bipolar thermal transport for high performance, *Energy & Environ. Sci.* **6**, 3346 (2013).

[22] Y. Pei, H. Wang and G. Snyder, Band engineering of thermoelectric materials, *Adv. Mater.* **24**, 6125-6135 (2012).

[23] L. Zhao, *et al.*, Ultrahigh power factor and thermoelectric performance in hole-doped single-crystal SnSe, *Science*, **351**, 141-144 (2015).

Chapter 6 High Power Factor and Output-power density in P-type NbFeSb-based Half-Heusler

A part of this chapter contains our submitted work

R. He, *et al*., Achieving high power factor and output power density in p-type half-Heuslers $Nb_{1-x}Ti_xFeSb$, *PNAS*, accepted, doi: 10.1073/pnas.1617663113.

6.1 Introduction

Higher power factor is important in yielding higher output-power density, as theoretically analyzed [1-2]. Thus, pursuing high-power-factor TE materials is important for power generation applications. In the constant-transport-property model, where all the thermoelectric parameters S, σ, and κ are assumed to be temperature independent, the output-power density of a TE leg is written as,

$$\omega = \frac{(T_H - T_C)^2}{4L} \overline{PF} \qquad (6.1)$$

where L is the leg length of the TE material and $\overline{PF}$ is the averaged power factor over the leg. Clearly, higher power factor favors higher power density when heat can be efficiently supplied and removed.

Recently the NbFeSb-based p-type half-Heusler compounds were reported exhibiting promising TE performances. High ZT values ~1 and ~1.5 were reported with Ti and Hf substitution, respectively [3-5]. These work mark the NbFeSb-based HH compounds as one of the most promising candidates for TE conversion in the mid-to-high temperature range.

Another distinguishing character of the NbFeSb-based HH compounds is the high power factor. Previous studies showed that HH compounds possess high power factors. Joshi *et al*. reported that the p-type half-Heusler $Nb_{0.6}Ti_{0.4}FeSb_{0.95}Sn_{0.05}$ had a power factor of ~23 μW cm^{-1} K^{-2} at room temperature and ~38 μW cm^{-1} K^{-2} at 973 K [3]. However, the composition with 40% Ti substitution strongly scattered the electrons as well. A subsequent work by Fu *et al*. reported a higher power factor of ~62 μW cm^{-1} K^{-2} at 400 K in $Nb_{0.92}Ti_{0.08}FeSb$ that was attributed to less electron scattering [4].

However, the work done by Fu *et al.* only studied one sintering temperature at 1123 K [4]. Since high temperature heat treatment for TE materials could be beneficial to TE performance [6], further optimization may be achieved in the NbFeSb system. Here, I studied the thermoelectric properties of $Nb_{1-x}Ti_xFeSb$ system with x = 0.04, 0.05, 0.06, 0.07, 0.1, 0.2, and 0.3 prepared by using arc-melting, ball-milling, and hot-pressing (HP) at 1123, 1173, 1273, and 1373 K. I found that higher HP temperature enhanced the carrier mobility, leading to a high power factor of ~106 μW cm^{-1} K^{-2} at 300 K in $Nb_{0.95}Ti_{0.05}FeSb$ [7]. Such an unusually high power factor at above room temperature was only observed in metallic systems with ultra-high electrical conductivity such as $YbAl_3$ and constantan [8, 9]. The similarly high power factor was never achieved in semiconductors at above room temperature. Furthermore, a record output-power density of ~22 W cm^{-2} with a leg length ~2 mm was experimentally obtained with T_C = 293 K and T_H = 868 K. I also observed that the lattice thermal conductivity hardly changed within the range of grain-sizes studied in this work. Thus, by using a higher HP temperature of 1373 K and changing the Ti

concentration, I obtained higher power factor and *ZT* than the previously reported results for the same compositions [4].

6.2 Experimental procedure

6.2.1 Sample preparation

The samples in this chapter were prepared in almost the same way as in chapters 4 and 5. The differences were the mass of each batch (15 grams in this chapter), and the ball-milling time (3 hours).

6.2.2 Structure characterization

A PANalytical multipurpose diffractometer with an X'celerator detector (PANalytical X'Pert Pro) was used to characterize the phases. The XRD spectra are shown in Figure 6.1. All samples possessed pure half-Heusler phase.

Morphologies of the freshly broken surface were characterized by a scanning electron microscopy (SEM, LEO 1525). The SEM images will be shown in section 6.3.1.

The elemental ratios of the samples were measured by an Electron Probe Micro-Analysis (EPMA, JXA-8600), and the results are shown in Table 6.1. A transmission-electron microscopy (TEM, JEOL 2100F) machine was used to observe the detailed microstructures, as shown in Figure 6.2.

Table 6.1 Electron Probe Micro-Analysis (EPMA) measurements on $Nb_{1-x}Ti_xFeSb$ [7].

Nominal	EPMA
$Nb_{0.96}Ti_{0.04}FeSb$	$Nb_{0.95}Ti_{0.04}Fe_{1.03}Sb_{0.98}$
$Nb_{0.95}Ti_{0.05}FeSb$	$Nb_{0.94}Ti_{0.05}Fe_{1.01}Sb_{0.99}$
$Nb_{0.94}Ti_{0.06}FeSb$	$Nb_{0.93}Ti_{0.06}Fe_{1.01}Sb_{0.99}$
$Nb_{0.93}Ti_{0.07}FeSb$	$Nb_{0.92}Ti_{0.07}Fe_{0.99}Sb_{1.01}$
$Nb_{0.9}Ti_{0.1}FeSb$	$Nb_{0.89}Ti_{0.1}Fe_{1.00}Sb_{0.99}$
$Nb_{0.8}Ti_{0.2}FeSb$	$Nb_{0.8}Ti_{0.2}Fe_{1.02}Sb_{0.99}$
$Nb_{0.7}Ti_{0.3}FeSb$	$Nb_{0.69}Ti_{0.3}Fe_{1.02}Sb_{0.98}$

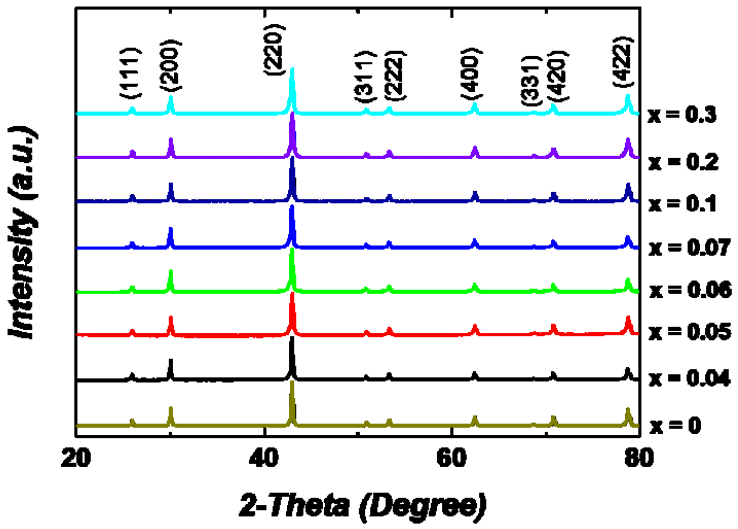

Figure 6.1 X-ray diffraction (XRD) patterns of $Nb_{1-x}Ti_xFeSb$. All of the compositions possess pure half-Heusler phase [7].

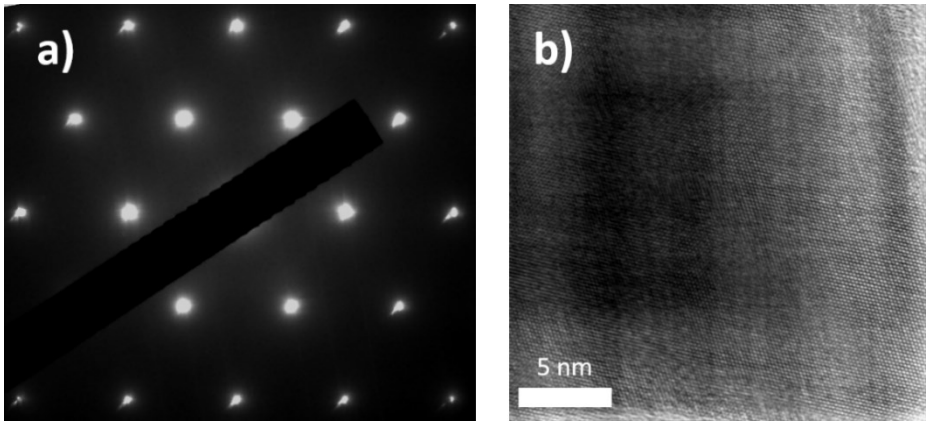

Figure 6.2 TEM observations. a) Selected-area-electron-diffraction pattern and b) High-resolution TEM image of $Nb_{0.95}Ti_{0.05}FeSb$ [7].

6.2.3 Thermoelectric properties measurement

The thermal conductivity is the multiplication as a product of thermal diffusivity (D), specific heat (c_P), and mass density, which were measured by a laser-flash system (LFA457, Netzsch), a differential-scanning calorimeter (DSC, 404 C), and an Archimedes' kit, respectively. Bar shaped samples (~2 × 2 × 12 mm^3) were used to measure electrical conductivity and Seebeck-coefficient on a ZEM-3 machine (ULVAC). Carrier concentrations, (n_H), were measured using a physical properties measurement system (PPMS, Quantum Design) under ±3 Tesla magnetic fields. The Hall mobility, μ_H, was calculated based on $\mu_H = \sigma R_H$, where R_H is the Hall coefficient. The uncertainty for electrical conductivity was 2%, Seebeck-coefficient 4%, and thermal conductivity 7%, so the combined uncertainty for power factor and ZT were 10% and 17%, respectively. The best composition was repeated at least three times, and the ZT variations were within 5% from run to run. To increase the readability, we did not plot error bars on some of the curves.

6.3 Results and discussion

6.3.1 Enhanced power factor with higher hot-pressing temperature

Figures 6.3a-f show the thermoelectric properties of $Nb_{0.95}Ti_{0.05}FeSb$ with hot-pressing temperatures of 1123, 1173, 1273, and 1373 K. As shown in Figure 1a, the power factor (*PF*) improved significantly at below 573 K. The peak value reached ~106 μW cm^{-1} K^{-2} at room temperature and is the highest in half-Heusler compounds. When the temperature was higher than 873 K, the power factor values converged.

Figure 6.3b shows that the high power factor mainly comes from the improved electrical conductivity. Above 673 K, the electrical conductivity values converged and followed the $T^{-3/2}$ law, suggesting that acoustic phonons dominate carrier scattering [10]. In contrast, Figure 1c shows the Seebeck-coefficient changes little regardless of the hot-pressing temperature. The dashed line in Figure 1c is the calculated Seebeck-coefficient using the single parabolic band (SPB) model [11] (taking the scattering parameter r=-0.5 since acoustic phonons scattering dominates),

$$S = +\left(\frac{k_B}{e}\right)\left[\frac{2F_1(\eta)}{F_0(\eta)} - \eta\right] \tag{6.2}$$

$$F_n(\eta) = \int_0^\infty \frac{\chi^n}{1+e^{\chi-\eta}}\, d\chi \tag{6.3}$$

where η is related with n_H through

$$n_H = 4\pi\left(\frac{2m_h^* k_B T}{h^2}\right)^{3/2} \frac{F_{1/2}(\eta)}{r_H} \tag{6.4}$$

$$r_H = \frac{3}{2}\frac{F_{-1/2}(\eta)F_{1/2}(\eta)}{2F_0^2(\eta)} \tag{6.5}$$

where η, n_H, m_h^*, and r_H are the reduced Fermi energy, the Hall carrier concentration, the density-of-states (DOS) effective mass of holes, and the Hall factor, respectively. The n_H values were obtained through the Hall measurement and are presented in Table 6.2. The DOS hole effective mass (m_h^*) was obtained by fitting the Pisarenko relation (see section 6.3.3). $F_n(\eta)$ is the Fermi integral of order n. The good agreement between the calculated result and experimental data showed the adequacy of the SPB model in describing the hole transport.

As shown in Figure 6.3d, the thermal conductivity was slightly lower for samples hot-pressed at lower hot-pressing temperature. This was mainly due to the difference in the electronic thermal conductivity originating from the difference in the electrical conductivity

$$\kappa_e = L\sigma T \tag{6.6}$$

$$L = \left(\frac{k_B}{e}\right)^2 \left[\frac{3F_2(\eta)}{F_0(\eta)} - \left(\frac{2F_1(\eta)}{F_0(\eta)}\right)^2\right] \tag{6.7}$$

where L is the Lorenz number. By subtracting the κ_e from κ_{tot}, I plotted the sum $\kappa_L + \kappa_{bip}$ in Figure 6.3e. The combined lattice and bipolar thermal conductivities were barely affected by the hot-pressing temperature. Furthermore, at temperatures above 773 K, the thermal conductivity trend deviated slightly from the T^{-1} behavior, indicating some minor bipolar effects even though the Seebeck-coefficient seemed not to show such an effect. The κ_{bip}, as shown in Figure 6.3f, was calculated using a three-band model [12] (see Appendix 6.5.1 for calculation details). The highest bipolar thermal conductivity reached ~0.4 W m^{-1} K^{-1} at 973 K, a small value compared to the κ_L.

Table 6.2 Room temperature Hall carrier concentration (n_H), Hall mobility (μ_H), Hall factor (r_H), deformation potential (E_{def}), relative density, and EPMA composition of $Nb_{1-x}Ti_xFeSb$ at different Ti concentrations and hot-pressing temperatures [7].

	n_H (10^{20} cm^{-3})	μ_H (cm^2 V^{-1} s^{-1})	r_H	E_{def} (eV)	relative density (%)
x = 0.04, 1373 K	6.3	25.2	1.12	12.5	99.1
x = 0.05, 1123 K	7.2	15.2	1.12	--*	99.4
x = 0.05, 1173 K	7.7	20.2	1.12	--*	98.9
x = 0.05, 1273 K	7.7	24.3	1.12	11.8	98.6
x = 0.05, 1373 K	8.1	26.3	1.12	11.5	99.0
x = 0.06, 1373 K	9.3	27.3	1.11	11.6	99.3
x = 0.07, 1373 K	10.7	26.7	1.10	11.6	98.9
x = 0.10, 1373 K	15.2	24.0	1.08	12.7	99.3
x = 0.20, 1373 K	25.7	15.2	1.06	13.7	99.1
x = 0.30, 1373 K	30.3	9.3	1.06	17.6	98.9

**Data are not shown since the mobility is strongly affected by grain-boundary scattering.*

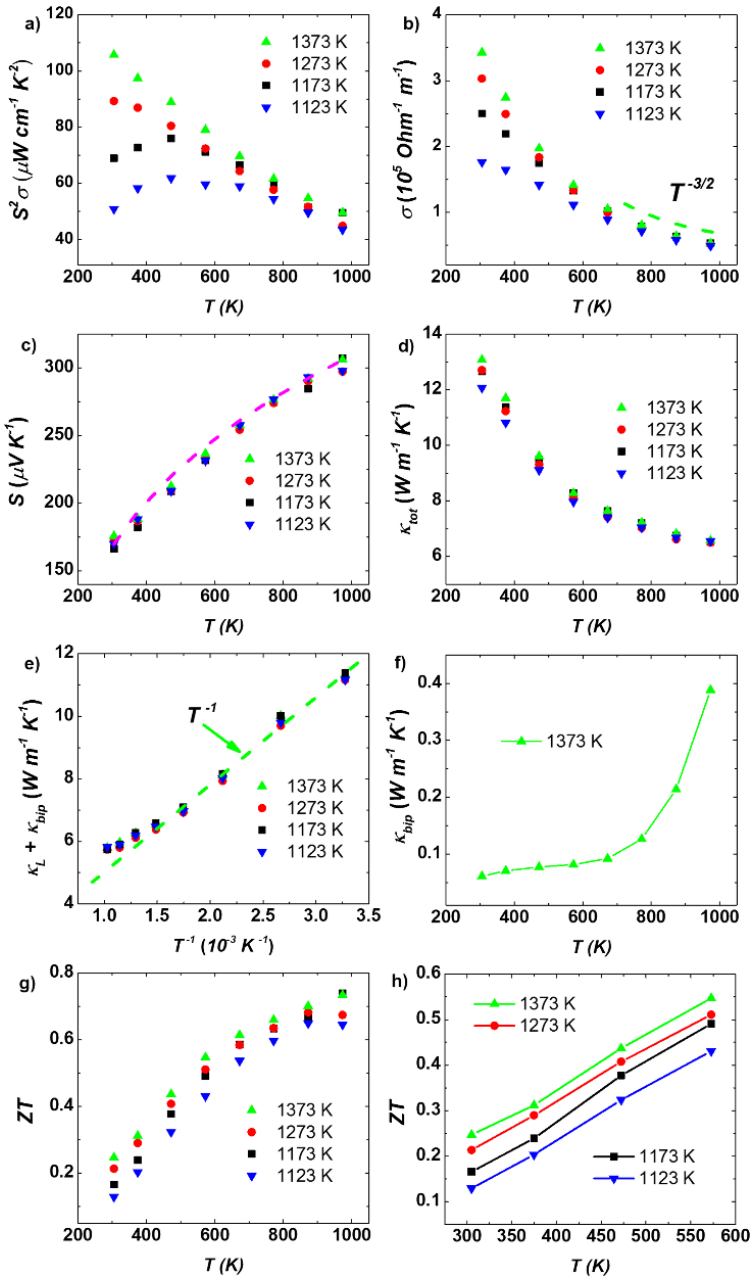

Figure 6.3 Thermoelectric-property dependence on temperature for the half-Heusler $Nb_{0.95}Ti_{0.05}FeSb$ hot-pressed at 1123, 1173, 1273, and 1373 K. a) power factor, b) electrical conductivity, c) Seebeck-coefficient, d) total thermal conductivity, e) lattice plus bipolar thermal conductivity, f) bipolar thermal conductivity, g) *ZT*, and h) *ZT* with *T* from 300 to 573 K. The green dashed lines in b) and e) represent the $T^{-3/2}$ and T^{-1} relations, respectively. The magenta dashed line in c) shows the calculated Seebeck-coefficient using the SPB model [7].

Because of the enhanced power factor and almost unaffected thermal conductivity, the *ZT* improved with elevated hot-pressing temperatures, as shown in Figure 6.3g. This was especially obvious at temperatures below 573 K, as shown in Figure 6.3h, where the power factor showed larger differences (see Figure 6.3a).

Scanning electron microscopy (SEM) images showed significant enlargement of the grains with higher hot-pressing temperatures, as shown in Figures 6.4a-d. The average grain-sizes were found to be ~0.3, ~0.5, ~3.0, and ~4.5 μm for samples pressed at 1123, 1173, 1273, and 1373 K, respectively (see Appendix 6.5.2).

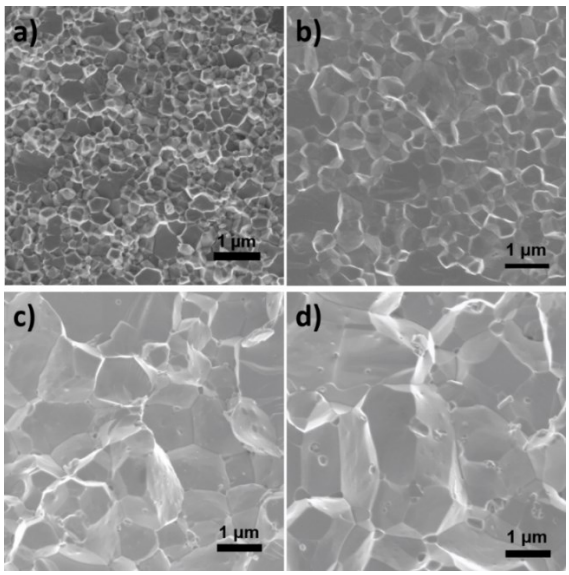

Figure 6.4 SEM images of $Nb_{0.95}Ti_{0.05}FeSb$ hot-pressed at a) 1123, b) 1173, c) 1273, and d) 1373 K [7].

Meanwhile, the room temperature (RT) Hall measurement (Table 6.2) showed a ~73% enhancement of Hall mobility (μ_H) of samples pressed at 1373 K over those pressed at 1123 K. Since the lattice thermal conductivity, as shown in Figure 6.3e, changed little

with the grain-size, it is interesting to investigate why the enlarged grain-size performs so differently on the electron transport.

6.3.2 Effect of grain-size on lattice thermal conductivity and carrier mobility

6.3.2.1 Effect of grain-size on lattice thermal conductivity

The lattice thermal conductivity (κ_L) of samples pressed at 1373 K was obtained by subtracting the electronic (κ_e) and bipolar (κ_{bip}) contribution from the measured total thermal conductivity (κ_{tot}). To describe the lattice thermal conductivity, I used the Klemens model [13] and splitted the phonon scattering into four different sources: three-phonon processes (3P), grain-boundary scattering (GB), point-defects scattering (PD), and electron-phonon interaction (EP). The calculation details and the fitting parameters are given in Appendix 6.5.3, the complete fitting results are given in section 6.3.3. Here, in Figure 6.5a, I show only the effect of grain-boundary scattering. Clearly, the calculated reduction in the lattice thermal conductivity was small with decrease grain-size, only ~9% when the grain-size decreases by more than one order of magnitude from 4.5 μm to 0.3 μm. A similarly small decrease in κ_L was seen experimentally (~2%). The insensitivity of the phonon transport to the grain-size might indicate that the dominant thermal phonon mean-free-paths (MFP) that contribute to the thermal conductivity of $Nb_{0.95}Ti_{0.05}FeSb$ were less than 0.3 μm. We measured the phonon MFP [14-16] distributions for $Nb_{0.95}Ti_{0.05}FeSb$. As shown in Appendix 6.5.4, the phonon-measurement results suggested that the dominant thermal phonon MFPs contributing to $Nb_{0.95}Ti_{0.05}FeSb$'s thermal conductivity were in a few tens to a few hundreds of nanometers. In particular, phonons with MFPs shorter than 300 nm contributed approximately 70% to the total $Nb_{0.95}Ti_{0.05}FeSb$ thermal conductivity

at room temperature. This supported our experimental observation that the thermal conductivity of $Nb_{0.95}Ti_{0.05}FeSb$ had a weak dependence on grain-sizes since the studied grain-size range in our measurement was significantly larger than the dominant thermal phonon MFPs.

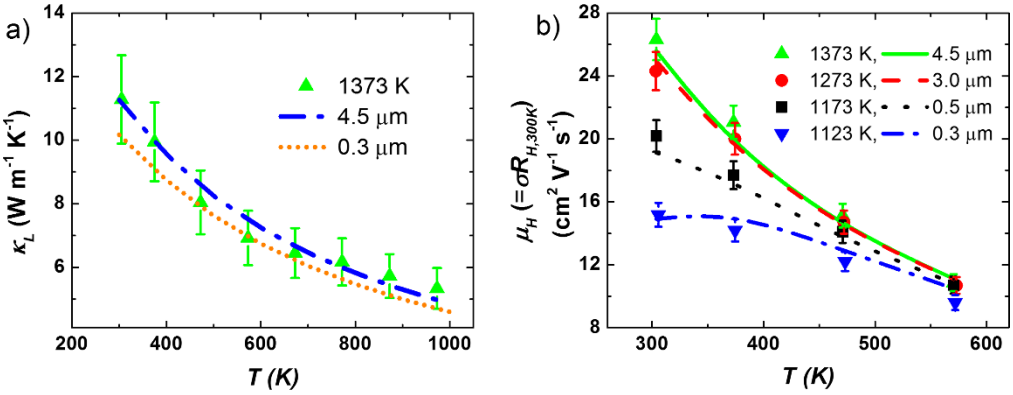

Figure 6.5 Effect of grain-size on a) lattice thermal conductivity and b) hole mobility. The symbols are measurement data and the lines are calculated values. The error bars in a) and b) show 12% and 4% relative error, respectively [7].

6.3.2.2 Effect of grain-size on carrier mobility

To analyze the measured carrier mobility, we assumed a constant n_H from room temperature through 573 K. This assumption is reasonable within the temperature region where the bipolar effect does not occur. A similar effect was also reported in other half-Heusler materials [11]. Thus, the carrier mobility (μ_H) varied in the same trend as the conductivity (σ) through

$$\sigma = qn_H\mu_H \tag{6.8}$$

with n_H being constant and q being the carrier charge. At high temperatures, the dominant electron scattering was from acoustic phonons (AP), thus the mobility can be expressed as

$$\mu_{AP} = \frac{F_0(\eta)}{2F_{1/2}(\eta)}\mu_0 \tag{6.9}$$

where,

$$\mu_0 = \frac{2\sqrt{2}e\pi\hbar^4}{3(k_BT)^{3/2}}\frac{v_l^2 d}{E_{def}^2\left(m_b^*\right)^{5/2}} \tag{6.10}$$

$$m_b^* = m_h^* \times (N_v)^{-2/3} \tag{6.11}$$

v_l is the longitudinal phonon velocity and calculated from the elastic constants [17], d is the mass density, m_h^* is the density-of-states (DOS) effective mass for holes, and N_v is the valley degeneracy. E_{def} is the deformation potential that was obtained by extrapolating the high temperature mobility back to room temperature using the $T^{3/2}$ law. E_{def} was found to be ~12 eV for $Nb_{0.95}Ti_{0.05}FeSb$, a relatively small value compared to other TE systems like InSb (~33 eV) [18], PbTe (~22.5 eV) [19], and Bi_2Te_3 (~20 eV) [20]. This smaller deformation potential in $Nb_{0.95}Ti_{0.05}FeSb$ suggested weaker electron-phonon interaction in the HH systems [11] that benefitted the electron transport and lead to a high power factor.

For mobility below 573 K, we considered the effect of the grain-boundary scattering [21, 22],

$$\mu_{GB} = De\left(\frac{1}{2\pi m_b^* k_B T}\right)^{1/2} exp\left(-\frac{E_B}{k_B T}\right) \tag{6.12}$$

where D is the grain-size and E_B is the barrier energy of the grain boundary. The barrier energy E_B was set as a common fitting parameter for $Nb_{0.95}Ti_{0.05}FeSb$. Combining the two scattering mechanisms according to the Matthiessen's rule yielded the expression for Hall mobility:

$$\mu_H^{-1} = \mu_{AP}^{-1} + \mu_{GB}^{-1} \quad (6.13)$$

The calculated mobility with E_B ~0.1 eV together with experimental data are shown in Figure 6.5b. The good fitting demonstrated the importance of the grain boundaries in scattering carriers, especially at below 573 K. In addition, Figure 6.5b shows that the grain-boundary scattering became stronger when the grain-size was smaller, for a decreasing size from 0.5 to 0.3 μm, the mobility decreased by ~30%, but when decreasing from 4.5 to 3.0 μm, the mobility dropped by only 5%.

6.3.3 TE properties of p-type $Nb_{1-x}Ti_xFeSb$

Figure 6.6 shows the TE properties of $Nb_{1-x}Ti_xFeSb$ pressed at 1373 K with x = 0, 0.04, 0.05, 0.06, 0.07, 0.1, 0.2, and 0.3 as a function of temperature. The electrical conductivity (σ) of undoped NbFeSb (*i.e.* x = 0) increased with temperature, consistent with typical semiconductor behavior (see inset in Figure 6.6a). The band gap was estimated from the high-temperature electrical conductivity using the following relation:

$$ln(\sigma) \propto E_g \times \frac{-1}{2k_BT} \quad (6.14)$$

The estimated band gap was ~0.51 eV, very close to 0.53 eV obtained from the density functional theory (DFT) calculation (see supporting information).

For the highly doped samples, σ obeyed the $T^{-3/2}$ law, suggesting dominant acoustic-phonon scattering of charge carriers [10]. Meanwhile, σ increased with increasing x up to 0.2 because of the increased n_H; upon further increase of x to 0.3, σ decreased due to the decreased μ_H because of the stronger alloy scattering (see Table 6.1). The Seebeck-

coefficient varied with n_H (see Figure 6.6b) in a good agreement with the Pisarenko relation using a density-of-states (DOS) effective mass $m_h^* = 7.5\, m_0$ [23] (Figure 6.7a),

$$S = \frac{8\pi k_B^2}{3eh^2} m_h^* T \left(\frac{\pi}{3n_H}\right)^{\frac{2}{3}} \tag{6.15}$$

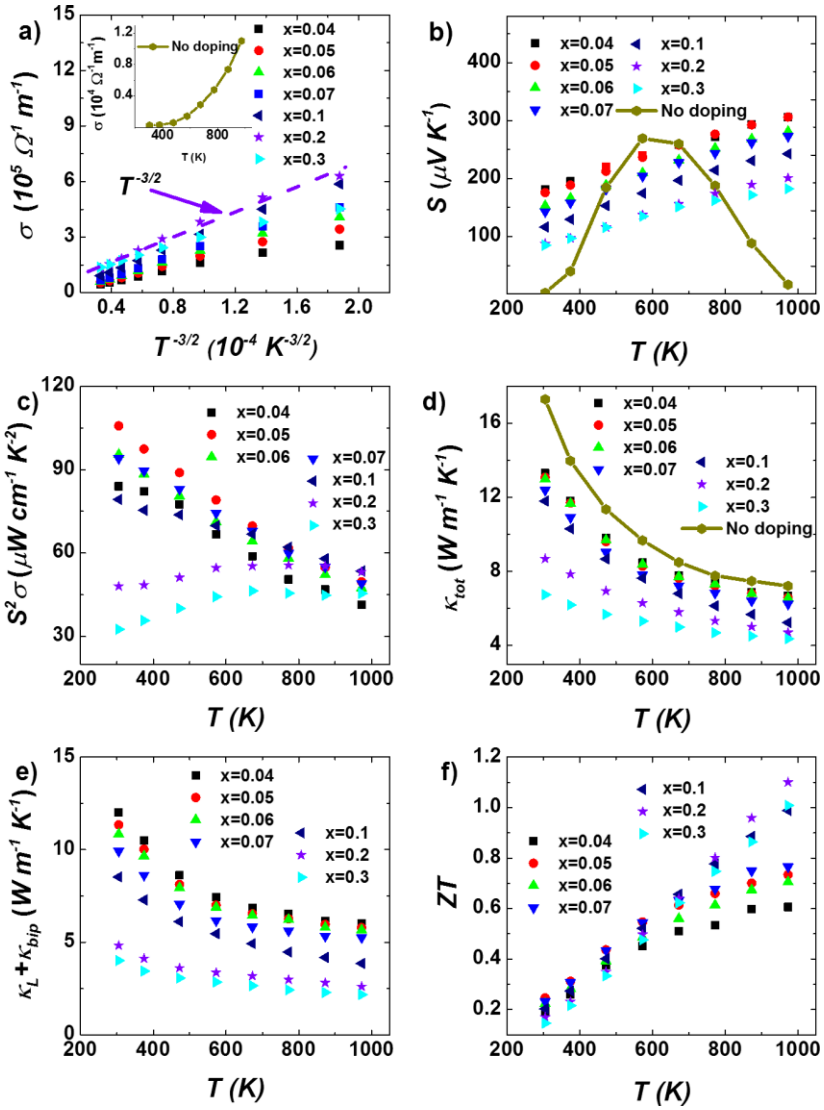

Figure 6.6 Thermoelectric-property dependence on temperature for $Nb_{1-x}Ti_xFeSb$ with x = 0, 0.04, 0.05, 0.06, 0.07, 0.1, 0.2, and 0.3. a) Electrical conductivity, b) Seebeck-coefficient, c) power factor, d) total thermal conductivity, e) lattice and bipolar thermal conductivity, and f) *ZT*. In a), the purple dashed line and the inset show the $\sim T^{-3/2}$ relation and the measured conductivity of undoped NbFeSb, respectively [7].

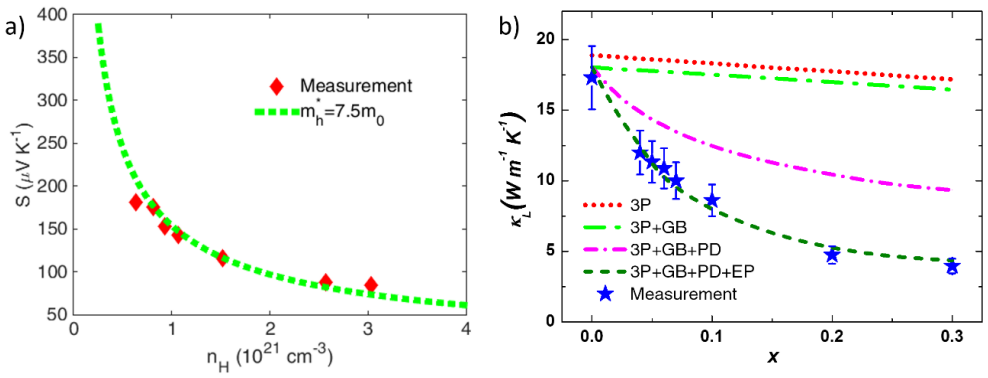

Figure 6.7 a) Pisarenko plot at 300 K, with DOS effective mass $m_h^* = 7.5\, m_0$ for holes, showing the validity of the single parabolic band (SPB) model in describing hole transport. b) The contribution of different phonon scattering mechanisms to the lattice thermal conductivity of $Nb_{1-x}Ti_xFeSb$ at room temperature. 3P, GB, PD, and EP represent three-phonon scattering, grain-boundary scattering, point-defect scattering, and electron-phonon interaction, respectively. For grain-boundary scattering, the grain-size is set as 4.5 μm. The error bars show 12% relative error [7].

The p-type $Nb_{1-x}Ti_xFeSb$ possessed conductivity and Seebeck-coefficient that were both very high, yielding high power factors at a wide temperature range (~100 μW cm^{-1} K^{-2} at room temperature and ~50 μW cm^{-1} K^{-2} at 973 K) for $Nb_{0.95}Ti_{0.05}FeSb$, $Nb_{0.94}Ti_{0.06}FeSb$, and $Nb_{0.93}Ti_{0.07}FeSb$, as shown in Figure 6.6c. These values were much higher than those reported by Fu *et al.*, where a temperature of 1123 K was used for sintering [4]. As shown in Figure 6.8a, higher pressing temperature accounted for the higher power factor. Moreover, even when comparing the samples pressed at 1123 K, our work also obtained higher power factor, with the probable reason being higher sample densities (~99%) compared to Fu's samples (~95%).

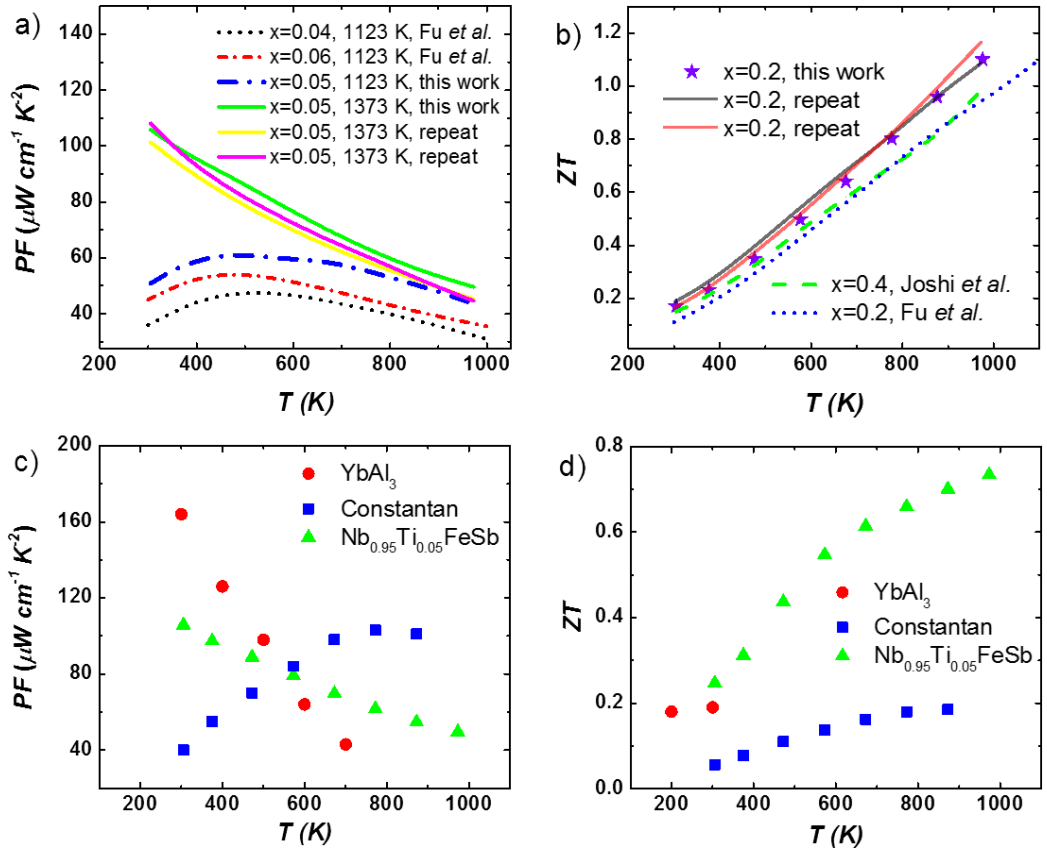

Figure 6.8 TE property comparison. a) Power factor and b) *ZT* of the $Nb_{1-x}Ti_xFeSb$ systems from different reports. c) Power factor and d) *ZT* among $Nb_{0.95}Ti_{0.05}FeSb$, constantan, and $YbAl_3$, with peak power factor exceeding 100 μW cm^{-1} K^{-2} [7].

The total thermal conductivities (κ_{tot}) are shown in Figure 6.6d. For the undoped sample, the thermal conductivity was ~17.3 W m^{-1} K^{-1} at RT and 7.2 W m^{-1} K^{-1} at 973 K. Ti doping effectively suppressed the thermal conductivity, especially the lattice part, as shown in Figure 6.6e. As a result, the peak *ZT* reached 1.1 for $Nb_{0.8}Ti_{0.2}FeSb$ (see Figure 6.6f) at 973 K with a linear upward trend suggesting even higher *ZT* at higher operating temperatures (see Figures 6.6f and 6.8b). In addition, the $Nb_{0.9}Ti_{0.1}FeSb$ and $Nb_{0.7}Ti_{0.3}FeSb$ material compositions also reached a promising *ZT* of ~1.0 at 973 K.

To analyze the room-temperature lattice thermal conductivity, we used the Klemens model incorporating different scattering mechanisms including the 3P, GB, PD, and EP processes, as mentioned in the previous section [13]. The fitting parameters used in this model are listed in the supporting information. The result is shown in Figure 6.7b. Indeed, the grain-boundary scattering was much weaker compared to the other scattering processes. Note that the electron-phonon (EP) interaction was quite important in this system. Similar results were also reported by Fu *et al.* with Zr and Hf doping [5].

Figures 6.8c and 6.8d compare the power factor and *ZT*, respectively, of a few materials with very high power factors, including $YbAl_3$ single crystal [8], $Nb_{0.95}Ti_{0.05}FeSb$ (this work), and constantan [9]. These materials possess peak power factors of at least 100 $\mu W\ cm^{-1}\ K^{-2}$. Notice that the other two materials are essentially metals where the anomalous Seebeck-coefficients for $YbAl_3$ and constantan are due to Kondo resonance [24] and virtual bound states [25], respectively. To the best of our knowledge, such a high power factor above room temperature was never realized before in semiconductor-based TE materials. On the other hand, the thermal conductivities of the other two materials are very high since they are essentially metals. Although the power factor of $Nb_{0.95}Ti_{0.05}FeSb$ is not the highest, its *ZT* is much higher than those of the other two materials.

6.3.4 Output-power density and conversion efficiency

6.3.4.1 Calculation of output-power density and conversion efficiency

Due to the higher power factor, higher power output is expected. Following the approach of Kim *et al.* [2], the output-power density (ω) and efficiency (η_{max}) under a large temperature gradient were calculated (Eq. 6.16 through Eq. 6.25).

$$\boldsymbol{\omega} = \frac{(PF)_{eng}(T_H - T_C)}{L} \frac{m_{opt}}{\left(1+m_{opt}\right)^2} \tag{6.16}$$

$$\boldsymbol{\eta_{max}} = \eta_C \frac{\sqrt{1+(ZT)_{eng}(\alpha_1/\eta_C)}-1}{\alpha_0\sqrt{1+(ZT)_{eng}(\alpha_1/\eta_C)}+\alpha_2} \tag{6.17}$$

$$(PF)_{eng} = \frac{\left(\int_{T_C}^{T_H} S(T)dT\right)^2}{\int_{T_C}^{T_H} \rho(T)dT} \tag{6.18}$$

$$(ZT)_{eng} = \frac{(PF)_{eng}}{\int_{T_C}^{T_H} \kappa(T)dT}(T_H - T_C) \tag{6.19}$$

$$m_{opt} = \sqrt{1 + (ZT)_{eng}\alpha_1\eta_c^{-1}} \tag{6.20}$$

$$\eta_C = \frac{T_H - T_C}{T_H} \tag{6.21}$$

$$\alpha_i = \frac{S_{T_H}(T_H - T_C)}{\int_{T_C}^{T_H} S(T)dT} - \frac{\int_{T_C}^{T_H} \tau(T)dT}{\int_{T_C}^{T_H} S(T)dT} W_T\eta_C - iW_J\eta_C \quad (i = 0, 1, 2) \tag{6.22}$$

$$\tau = T\frac{dS(T)}{dT} \tag{6.23}$$

$$W_T = \frac{\int_{T_C}^{T_H}\int_{T}^{T_H} \tau(T)dTdT}{\Delta T \int_{T_C}^{T_H} \tau(T)dT} \tag{6.24}$$

$$W_J = \frac{\int_{T_C}^{T_H}\int_{T}^{T_H} \rho(T)dTdT}{\Delta T \int_{T_C}^{T_H} \rho(T)dT} \tag{6.25}$$

The calculated output-power density and efficiency are shown in Figures 6.10a and 6.10b, respectively. With T_C = 293 K and a leg length L = 2 mm, the calculated ω and η_{max} were ~28 W cm^{-2} and 8.8%, respectively, for $Nb_{0.95}Ti_{0.05}FeSb$ when T_H was 868 K.

6.3.4.2 Measurements of output-power density and conversion efficiency

The efficiency and output-power measurements on single legs were performed using an established approach [26]. In this work, the $Nb_{0.95}Ti_{0.05}FeSb$ and $Nb_{0.8}Ti_{0.2}FeSb$ were cut and polished to a size of ~1.3 × 1.3 mm^2 in cross section and ~2 mm in height. The TE leg was directly brazed ($Ag_{0.45}Cu_{0.15}Zn_{16}Cd_{24}$, liquidus 618 °C) to the copper enclosure of the hot-junction heater assembly (Figure 6.9a). The cold side of the TE leg was first electroplated with copper, nickel, and gold and then soldered ($In_{52}Sn_{48}$, melting point 118 °C) onto the cold-junction copper electrode (Figure 6.9b). The hot- and cold-junction braze/solder joints were mechanically strong and showed insignificant electrical contact resistance at room temperature. However, due to the excellent braze wettability of the samples, it was difficult to prevent sidewall wetting completely. Due to the nature of the single TE leg experiment, the electric current needed to be supplied at the hot-junction of the TE leg. Thus, the hot-junction heater assembly also functioned as the electrical hot-junction for the TE leg. The large thermoelectric current due to the low electrical conductance of the samples could be a significant challenge due to joule heating in the hot-junction current leads. These were minimized by choosing a large-diameter copper current wire. The single TE leg device was surrounded by an electrically heated copper-guard heater to which the leads of the heater assembly (electric current, voltage, and thermocouple leads) were thermally grounded to minimize parasitic heat losses. The experiments were performed under high vacuum (below 10^{-4} mbar) to eliminate convection and air conduction losses. The copper cold-junction electrode was soldered onto a thermoelectric cooler (TEC) that was soldered onto a liquid-cooled cold plate to enable

accurate cold-junction temperature control. The cold-junction temperature was measured with a T-type thermocouple that was embedded in the cold-junction copper electrode. The hot-junction temperature was measured with a K-type thermocouple embedded inside the copper enclosure of the heater assembly. During the experiments, the guard-heater temperature (measured with a K-type thermocouple) was maintained close to the temperature of the hot-junction heater to minimize parasitic heat losses. The single TE-leg power output (density) and efficiency experiments were performed by measuring the thermoelectric voltage (V_{TE}) as a function of the thermoelectric current (I_{TE}) and recording the electrical input power to the hot-junction heater at various hot-junction temperatures (T_H) while the cold-junction temperature (T_C) was maintained at 293 K. Figure 6.9c shows an example of a current-voltage and current-power curve for the single TE-leg device operating with a hot-junction temperature of 773 K. Due to the large conductance of the measured TE samples, the radiative thermal shunting between the hot-side and cold-side was conservatively estimated to be below 0.5% in the measured temperature range. The effect of radiative heat transfer between the TE-leg and its surroundings on the measurement was similarly insignificant.

The measured values were ~22 W cm^{-2} and 5.6% for the output-power density and the conversion efficiency, respectively (Figures 6.10a-b). These values were lower than the calculated results, probably due to imperfect device fabrication and possible parasitic heat losses during the device measurement. To the best of our knowledge, this work obtained the highest power density for bulk thermoelectric materials, which could be important for power generation applications [3, 5, 27, 28].

Figures 6.10c and 6.10d show the power factor and *ZT*, respectively, of $Nb_{0.95}Ti_{0.05}FeSb$ and $Nb_{0.8}Ti_{0.2}FeSb$. Clearly, from Figures 6.10a and 6.10c, higher power factor led to higher output-power density with the same leg length. Similarly, higher *ZT* resulted in higher efficiency, as shown in Figures 6.10b and 6.10d.

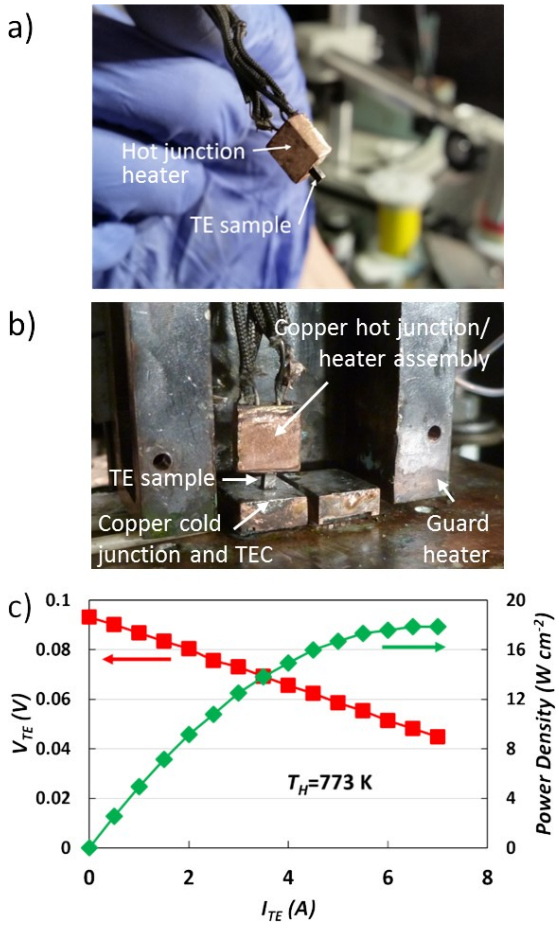

Figure 6.9 a) A TE sample brazed to the copper hot-junction heater assembly. b) TE single-leg device mounted to the test rig and surrounded by a guard heater to minimize parasitic heat losses from the hot-junction heater. The cold-junction temperature was maintained with a thermoelectric cooler (TEC) mounted onto a liquid cooled cold stage. c) Thermoelectric voltage (V_{TE}) and output-power density as functions of thermoelectric current (I_{TE}) at constant hot-side and cold-side temperatures of 773 K and 293 K, respectively [7].

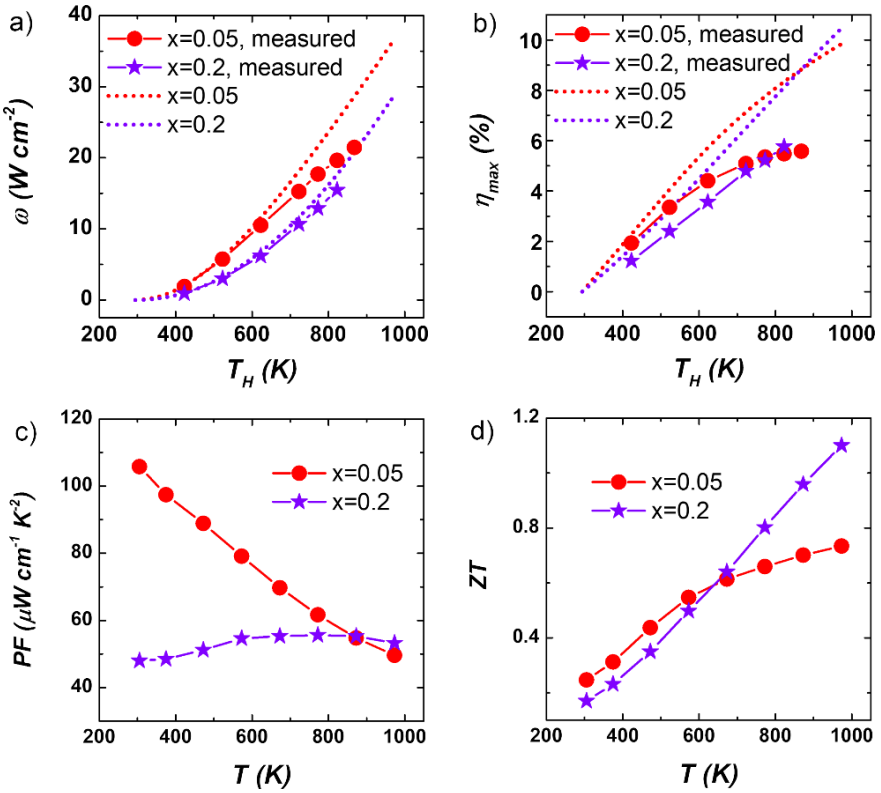

Figure 6.10 Calculated (dotted lines) and measured (symbols) a) output-power density and b) conversion efficiency of $Nb_{1-x}Ti_xFeSb$ (x = 0.05 and 0.2) samples with the cold side temperature at ~293 K and the leg length ~2 mm. Comparison of c) power factor and d) *ZT* of $Nb_{0.95}Ti_{0.05}FeSb$ and $Nb_{0.8}Ti_{0.2}FeSb$ [7].

6.4 Summary

A higher hot-pressing temperature up to 1373 K was found to be beneficial for higher carrier mobility due to larger grain-sizes. The resulting increase in electrical conductivity led to a much higher power factor of ~106 μW cm^{-1} K^{-2} in the p-type half-Heusler $Nb_{0.95}Ti_{0.05}FeSb$. With the high power factor, a record output-power density of ~22 W cm^{-2} was experimentally achieved, which could be important for power-generation applications.

6.5 Appendices

6.5.1 Three-band model for calculating bipolar thermal conductivity

6.5.1.1 Band structure of NbFeSb

The DFT band structure of the base composition NbFeSb is shown in Figure 6.11a. Two software packages were used, *Quantum Espresso* (*QE*, grey curves) and *elk* (red curves); the latter used the full electron approach and gave almost identical results as *QE*. It showed an indirect gap of 0.53 eV between the conduction band minima (CBM) X point (with valley degeneracy $N_c = 3$) and valance band maxima (VBM) L point (valley degeneracy $N_v = 4$). In addition, there was a light band (V_L) and a heavy band (V_H) at the VBM, and the total $N_v = 8$.

6.5.1.2 Reduced Fermi level for each band

The Fermi-Dirac integral is defined as follows:

$$F_n(\eta) = \int_0^\infty \frac{\chi^n}{1+e^{\chi-\eta}} d\chi \tag{6.26}$$

where η is the reduced Fermi energy.

The calculated carrier concentrations for the three bands are

$$n_c = 4\pi \left(\frac{2m_C^* k_B T}{h^2}\right)^{3/2} \frac{F_{1/2}(\eta_C)}{r_H(\eta_C)} \tag{6.27}$$

$$p_{VL} = 4\pi \left(\frac{2m_{VL}^* k_B T}{h^2}\right)^{3/2} \frac{F_{1/2}(\eta_{VL})}{r_H(\eta_{VL})} \tag{6.28}$$

$$p_{VH} = 4\pi \left(\frac{2m_{VH}^* k_B T}{h^2}\right)^{3/2} \frac{F_{1/2}(\eta_{VH})}{r_H(\eta_{VH})} \tag{6.29}$$

where k_B is the Boltzmann constant, r_H is the Hall factor, and h is the Planck constant.

The carrier concentration of each band obeys the neutrality equation as follows:

$$N_{exp} = p_{VL} + p_{VH} - n_C \tag{6.30}$$

In this work, we assumed that N_{exp} remains constant throughout the entire temperature range.

The relationship between the reduced Fermi energies of each band is:

$$\eta_{VH} = -\eta_C - E/k_BT \tag{6.31}$$

$$\eta_{VL} = -\eta_C - (E + H)/k_BT \tag{6.32}$$

where η_C, η_{VH}, and η_{VL} are the reduced Fermi energy for the conduction band, heavy valence band, and light valence band, respectively. E is the band gap and H is the band offset between the two valence bands.

Eqs. (6.26) through (6.32) were used to solve for the reduced Fermi energy for each band.

6.5.1.3 Temperature-dependent band gap and band offset

The temperature dependence of band gap E on temperature can be expressed as follows:

$$dE/dT = a_1 \times 10^{-4} \text{ eV/K} \tag{6.33}$$

where a_1 could be estimated in the following way:

For undoped NbFeSb, the conductivity at high temperature satisfied

$$ln(\sigma) \propto E \times \frac{-1}{2k_BT} \quad (6.34)$$

and E is ~0.51 eV using the data between 673 K to 973 K (Figure 6.11b). Therefore, a_1 varied between 0.2 and 0.4. In the calculation, a value of 0.3 was used.

The band gap, E, can be expressed as follows:

$$E = E_0 + (dE/dT) \times T \quad (6.35)$$

where E_0 is the bandgap at 0 K. The E_0 of NbFeSb was taken from the DFT calculation, ~0.53 eV.

6.5.1.4 Temperature-dependent band offset between two valance bands

H_0 is the band offset at 0 K. In our case, the H_0 of NbFeSb was estimated to be ~0.003 eV (Figure 6.11c) by low temperature Hall measurement, as [29]

$$\beta \propto exp\left(-\frac{H_0}{k_BT}\right) \quad (6.36)$$

$$|log(\beta)| \propto \frac{H_0}{k_BT} \quad (6.37)$$

where

$$\beta = \frac{R_T - R_0}{R_0} \quad (6.38)$$

R_T is the Hall coefficient at temperature T.

The dependence of the band offset H on temperature can be expressed as follows:

$$dH/dT = a_2 \times 10^{-4} \text{ eV/K}; \quad (6.39)$$

where a_2 needs to be fitted. The fitted value of a_2 equals -1.

The calculated carrier mobility of each band includes scattering by acoustic phonons within the deformation potential approximation.

The mobility for acoustic phonon scattering μ_{ph} can be expressed as:

$$\mu_{AP} = \frac{\sqrt{2}e\pi\hbar^4}{3(k_BT)^{3/2}} \frac{v_l^2 d}{E_{def}^2 \left(m_b^*\right)^{5/2}} \frac{F_0(\eta)}{F_{1/2}(\eta)} \tag{6.40}$$

where v_l is the longitudinal sound wave, ρ is the density, and E_{ph} is the deformation potential due to the phonons wave.

The electrical conductivity for each band can be calculated as follows:

$$\sigma_C = en_C\mu_C \tag{6.41}$$

$$\sigma_{VH} = en_{VH}\mu_{VH} \tag{6.42}$$

$$\sigma_{VL} = en_{VL}\mu_{VL} \tag{6.43}$$

The total electrical conductivity can be calculated as follows:

$$\sigma_{tot} = \sigma_C + \sigma_{VL} + \sigma_{VH} \tag{6.44}$$

The Lorenz number for each band can be calculated as follows. Assuming that the acoustic phonon scattering is the dominant scattering mechanism for electrons in each band, the scattering parameter is therefore, r = -1/2.

$$L_C = \left(\frac{k_B}{e}\right)^2 \left\{ \frac{(r+7/2)F_{r+5/2}(\eta_C)}{(r+3/2)F_{r+1/2}(\eta_C)} - \left[\frac{(r+5/2)F_{r+3/2}(\eta_C)}{(r+3/2)F_{r+1/2}(\eta_C)}\right]^2 \right\} \tag{6.45}$$

$$L_{VH} = \left(\frac{k_B}{e}\right)^2 \left\{ \frac{(r+7/2)F_{r+5/2}(\eta_{VH})}{(r+3/2)F_{r+1/2}(\eta_{VH})} - \left[\frac{(r+5/2)F_{r+3/2}(\eta_{VH})}{(r+3/2)F_{r+1/2}(\eta_{VH})}\right]^2 \right\} \tag{6.46}$$

$$L_{VL} = \left(\frac{k_B}{e}\right)^2 \left\{\frac{(r+7/2)F_{r+5/2}(\eta_{VL})}{(r+3/2)F_{r+1/2}(\eta_{VL})} - \left[\frac{(r+5/2)F_{r+3/2}(\eta_{VL})}{(r+3/2)F_{r+1/2}(\eta_{VL})}\right]^2\right\} \quad (6.47)$$

The total Lorenz number L_{tot} is the weighted value of the Lorenz number for each band [30],

$$L_{tot} = \frac{L_C\sigma_C + L_{VH}\sigma_{VH} + L_{VL}\sigma_{VL}}{\sigma_C + \sigma_{VH} + \sigma_{VL}} \quad (6.48)$$

The Seebeck-coefficient can also be calculated for each band as follows,

$$S_C = -\frac{k_B}{e}\left[\frac{(r+5/2)F_{r+3/2}(\eta_C)}{(r+3/2)F_{r+1/2}(\eta_C)} - \eta_C\right] \quad (6.49)$$

$$S_{VH} = +\frac{k_B}{e}\left[\frac{(r+5/2)F_{r+3/2}(\eta_{VH})}{(r+3/2)F_{r+1/2}(\eta_{VH})} - \eta_{VH}\right] \quad (6.50)$$

$$S_{VL} = +\frac{k_B}{e}\left[\frac{(r+5/2)F_{r+3/2}(\eta_{VL})}{(r+3/2)F_{r+1/2}(\eta_{VL})} - \eta_{VL}\right] \quad (6.51)$$

Note that the Seebeck-coefficient for the conduction band is negative while it is positive for the valence band.

The total Seebeck-coefficient is the weighted value of the Seebeck-coefficient of each band [31],

$$S_{tot} = \frac{S_C\sigma_C + S_{VH}\sigma_{VH} + S_{VL}\sigma_{VL}}{\sigma_C + \sigma_{VH} + \sigma_{VL}} \quad (6.52)$$

The measured Seebeck-coefficient in conjunction with electrical resistivity could be used to fit the value of a_2.

To complete the analysis, the knowledge of electron mobility of n-type NbFeSb was necessary. With the same sample process routine, I found Co doping effectively makes n-type materials. The required carrier mobility values are listed in Table 6.3.

Table 6.3 n_H and μ_H of $NbFe_{1-y}Co_ySb$ at room temperature [7].

y	n_H (10^{20} cm^{-3})	μ_H (cm^2 V^{-1} s^{-1})
0.02	-2.0	26.3
0.04	-3.6	22.3
0.06	-8.5	23.3

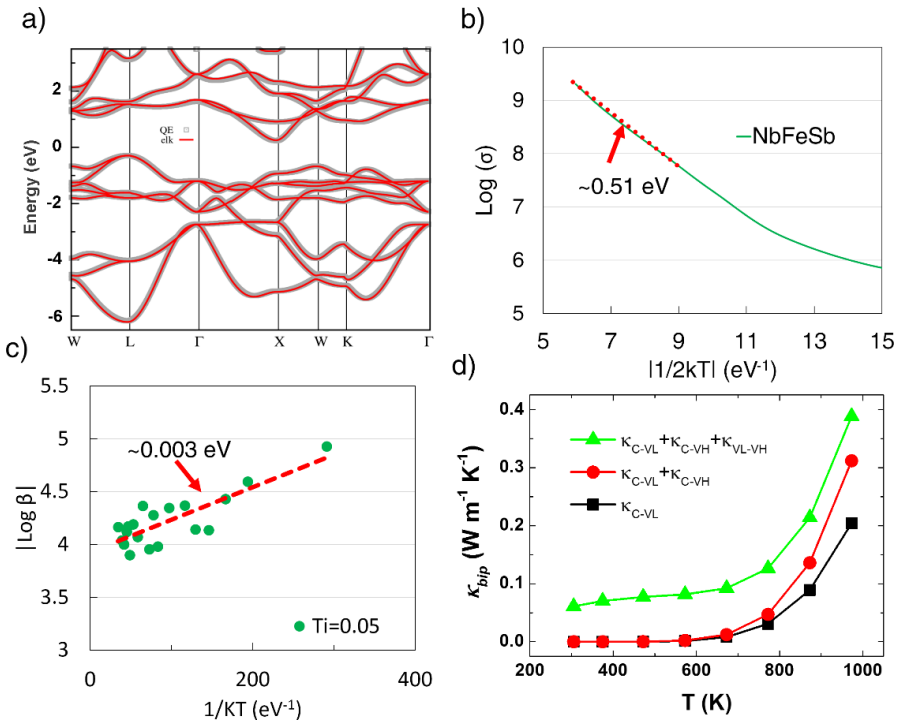

Figure 6.11 a) DFT-band structures calculated by *Quantum Expresso* (grey, squares) and *elk* (red, solid line) with full-electron approach. b) Estimated band gap using the conductivity of intrinsic (undoped) NbFeSb. c) Estimated band offset between the two valence bands. d) Bipolar thermal conductivity among different bands. $\kappa_{C\text{-}VL}$, $\kappa_{C\text{-}VH}$, and $\kappa_{VL\text{-}VH}$ are the bipolar thermal conductivity values between the conduction-V_L band, the conduction-V_H band, and the V_L band-V_H band, respectively [7].

The bipolar thermal conductivity of each band can be calculated as follows:

$$\kappa_{C\_VL} = \frac{\sigma_C \sigma_{VL}}{\sigma_{tot}} (S_C - S_{VL})^2 T \quad (6.53)$$

$$\kappa_{C\_VH} = \frac{\sigma_C \sigma_{VH}}{\sigma_{tot}} (S_C - S_{VH})^2 T \quad (6.54)$$

$$\kappa_{VL\_VH} = \frac{\sigma_{VL} \sigma_{VH}}{\sigma_{tot}} (S_{VL} - S_{VH})^2 T \quad (6.55)$$

Total bipolar thermal conductivity is the sum of the above-mentioned three components.

$$\kappa_{bip} = \kappa_{C\_VL} + \kappa_{C\_VH} + \kappa_{VL\_VH} \quad (6.56)$$

The calculated results are shown in Figure 6.11d,

6.5.2 Grain-size analysis

I etched the fine polished sample surfaces for analyzing the grain-size distribution. The sample surfaces were first mechanically polished by alumina sandpaper with particle-size of ~1 μm, following diamond suspension polishing with a particle-size ~0.25 μm, finishing with ~50 nm SiO_2 suspension on a VibroMet machine, usually resulting in a surface roughness on the order of ~10 nm [32]. The smooth surfaces were then chemically etched for 10 to 15 seconds using etchant containing 50 ml distilled water, 1 ml HF acid (38%), 2 ml H_2O_2 (35%), similar to the reported work [33]. As an example, Figure 6.12 shows the etched surface of a sample pressed at 1373 K. The statistical analysis of grain-size is shown in Figure 6.13 and 6.14, where Figure 6.13 presents the normalized cumulative size distribution and Figure 6.14 shows the raw data.

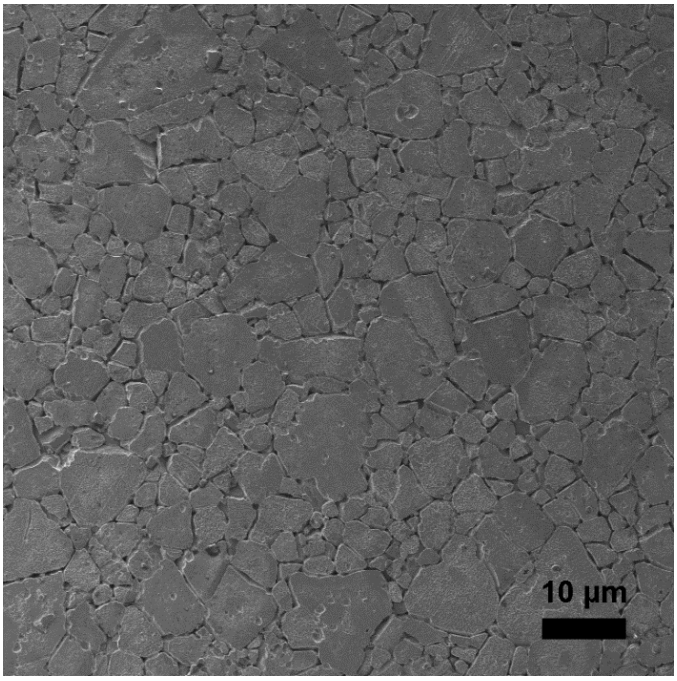

Figure 6.12 The etched surface of $Nb_{0.95}Ti_{0.05}FeSb$ pressed at 1373 K [7].

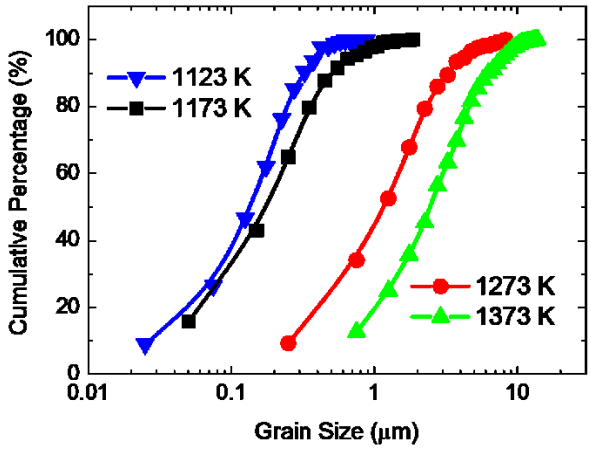

Figure 6.13 Normalized cumulative grain-size distribution of $Nb_{0.95}Ti_{0.05}FeSb$ pressed at 1123, 1173, 1273, and 1373 K [7].

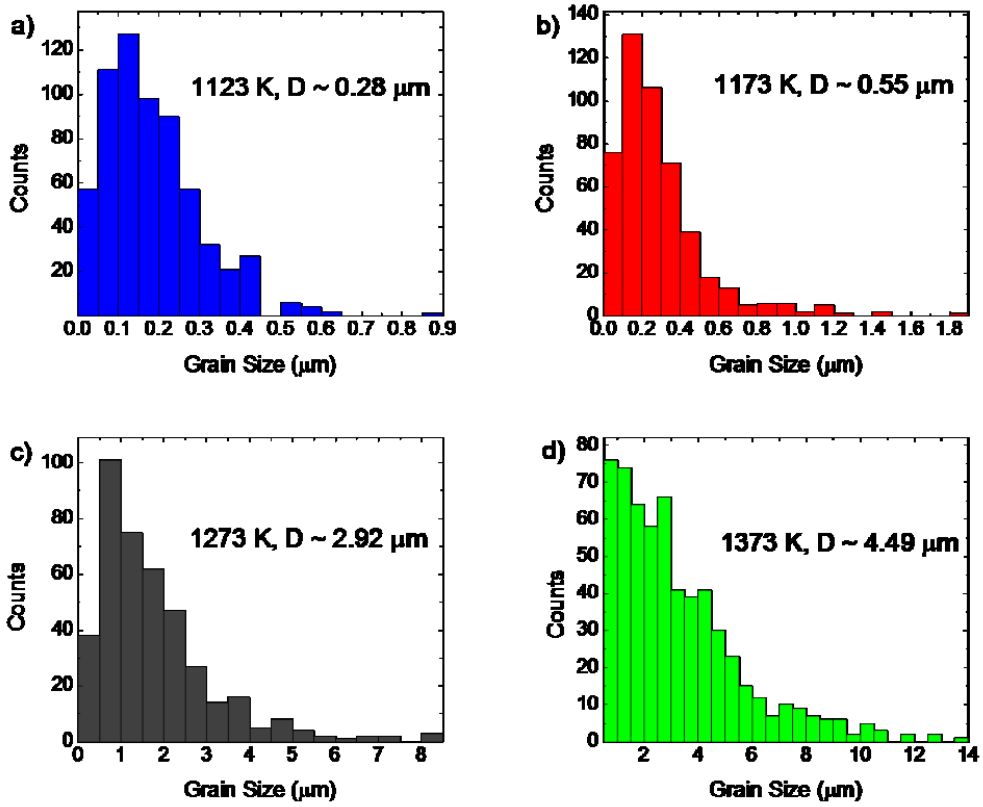

Figure 6.14 Statistical grain-sizes analysis of $Nb_{0.95}Ti_{0.05}FeSb$ pressed at 1123, 1173, 1273, and 1373 K. The average size is area weighted; and thus larger grains have larger weight when averaging [7].

6.5.3 Klemens model for lattice thermal conductivity

In the Klemens model [13] the lattice thermal conductivity is:

$$\kappa_L = \frac{k_B}{2\pi^2 v}\left(\frac{k_B}{\hbar}\right)^3 T^3 \int_0^{\theta_D/T} \tau(x) \frac{x^4 e^x}{(e^x-1)^2} dx \qquad (6.57)$$

where k_B, v, $\hbar$, T, θ_D, and τ are the Boltzmann constant, the phonon velocity, the Planck constant, the absolute temperature, the Debye temperature, and the phonon relaxation time,

respectively. x is defined as $x = \hbar\omega/k_B T$ (ω is the phonon frequency). It is important to evaluate the phonon relaxation time as a function of frequency, *i.e.* $\tau(x)$.

The Debye temperature and phonon velocity are related to each other by,

$$k_B \theta_D = \hbar v (6\pi^2 n)^{1/3} \tag{6.58}$$

where n is the number of atoms per unit volume.

The evaluation of phonon relaxation time follows the Matthiessen's rule [34],

$$\tau^{-1} = \tau_{PD}^{-1} + \tau_{3P}^{-1} + \tau_{EP}^{-1} + \tau_{GB}^{-1} \tag{6.59}$$

where the subscripts PD, 3P, EP, and GB represent the point-defect scattering, three-phonon processing, phonon-electron interaction, and grain-boundary scattering, respectively.

6.5.3.1 Point-defect scattering

The relaxation time for point-defects is [35],

$$\tau_{PD}^{-1} = Ax^4, \quad A = \left(\frac{k_B T}{\hbar}\right)^4 \frac{V_{atom}\Gamma}{4\pi v^3} \tag{6.60}$$

V_{atom} is the volume occupied per atom (not the volume of an atom), which is inversely proportional to the density ρ,

$$\rho V_{atom} = \bar{M} \tag{6.61}$$

$\bar{M}$ is the average atomic mass.

Γ is an important parameter that is called the scattering parameter. It could be written as [36, 37],

$$\Gamma = \frac{1}{3}\left(\frac{\bar{m}}{\bar{M}}\right)^2 \left[\sum_i f_i \left(1 - \frac{m_i}{\bar{m}}\right)^2 + \varepsilon \sum_i f_i \left(1 - \frac{r_i}{\bar{r}}\right)^2\right] \quad (6.62)$$

$\bar{m}$ and $\bar{r}$ are the average atomic mass and average radius of the substituted sites, respectively. f_i, m_i, and r_i are the fractional concentration, atomic mass, and atomic radius of the *i-th* substitution atom, respectively, and ε is a phenomenological parameter for fitting.

6.5.3.2 Phonon-phonon interaction

Roufosse and Klemens [38] studied the relaxation time of three-phonon processing of monatomic cubic crystals. Due to its higher complexity, the phonon relaxation time of half-Heuslers (HH) should be lower than that following the routine by Roufosse and Klemens. As pointed out by Geng *et al.* [39], by introducing a reduced anharmonicity constant γ_1, the phonon relaxation time of HH due to three-phonon processing could be written as

$$\tau_{3P}^{-1} = Bx^2, \quad B = \frac{4\pi}{\sqrt{2}} \frac{k_B \gamma_1^2 V_{atom}^{1/3}}{m\bar{M}v^3} T \left(\frac{k_B T}{\hbar}\right)^2 \quad (6.63)$$

m is the unit atomic mass and γ_1 is taken as the fitting parameter. Here, we use a linear interpolation when changing the compositions; thus *B* is not a constant value.

6.5.3.3 Electron-phonon interaction

Phonon relaxation time under electron-phonon interaction satisfies,

$$\tau_{EP}^{-1} = Cx^2 \tag{6.64}$$

As pointed out by Shi *et al.* [40], C is proportional to the four-thirds power of the carrier concentration ($C \sim n_H^{4/3}$).

6.5.3.4 Grain-boundary scattering

$$\tau_{GB}^{-1} = v/D \tag{6.65}$$

D is the grain-size, which is set as 4.5 μm. v is the averaged phonon velocity of one longitudinal branch (v_L) and two transverse branches ($v_{T1}\ and\ v_{T2}$),

$$\frac{1}{v^3} = \frac{1}{3}\left(\frac{1}{v_L^3} + \frac{1}{v_{T1}^3} + \frac{1}{v_{T2}^3}\right) \tag{6.66}$$

The three speed branches are estimated through the elastic constants (C_{11}, C_{12}, and C_{44}). For $Nb_{1-x}Ti_xFeSb$, I assume their phonon velocities can be linearly interpolated between NbFeSb to TiFeSb. Therefore, I only need to know the elastic constants of the compositions at the two ends. The elastic constants of NbFeSb were previously calculated by Hong *et al.* [17]. However, I cannot find any previous report on the elastic properties of ternary TiFeSb, and thus the values of TiCoSb were used because the elastic constants barely changed in the $TiCo_{1-\delta}Fe_\delta Sb$ systems [41]. Table 6.4 lists the fitting parameters.

Table 6.4 Important parameters in Klemens model for $Nb_{1-x}Ti_xFeSb$ [7].

x	*PD*		*3P*		*EP*	v (m s^{-1})
	$\Gamma(10^{-3})$	ε	B (10^{11} s^{-1})	γ_I	$C \times n_H^{-4/3}$ (m^4 s^{-1})	
0	0	80	8.06	0.69	3.86×10^{-25}	3879
0.04	4.5		8.16			3871
0.05	5.6		8.19			3869
0.06	6.6		8.22			3867
0.07	7.6		8.24			3865
0.1	10.6		8.32			3859
0.2	19.0		8.59			3838
0.3	25.4		8.90			3818

6.5.4 Phonon mean-free-path (MFP) measurement

We used a recently developed phonon mean-free-path (MFP) spectroscopy technique [14-16, 42, 43] to approximately measure the room temperature distribution of phonon MFPs that contributed to thermal transport in $Nb_{0.95}Ti_{0.05}FeSb$ hot-pressed at 1273 K. Briefly, the spectroscopy technique is based upon observing non-diffusive thermal transport at length scales comparable with or smaller than the dominant thermal phonon MFPs [44]. To access the non-diffusive transport regime, nanoscale metallic gratings of variable line widths were microfabricated on top of the $Nb_{0.95}Ti_{0.05}FeSb$ samples that had been fine polished to achieve a root-mean-square roughness ~5 nm before microfabrication. Figure 6.15a shows a representative scanning electron microscopy (SEM) image of the

fabricated metallic grating on top of the sample. The metallic gratings served as both heaters and thermometers in the time-domain thermoreflectance (TDTR) measurements that were used to measure the size-dependent thermal conductivities. When the heater size (i.e. grating line width) was much larger than the phonon MFPs, phonons experienced sufficient scattering to establish a local thermodynamic equilibrium after they traversed the metal-substrate interface, resulting in a diffusive transport regime that could be accurately described by the Fourier's law. However, when the heater size became comparable with the dominant thermal-phonon MFPs, some long-MFP phonons did not scatter as inherently assumed by the heat diffusion theory, leading to a non-diffusive transport regime where the measured thermal conductivity became size-dependent [44].

An in-house two-tint TDTR setup was used to probe the size-dependent thermal transport in the fabricated material system [15, 45, 46]. Details of the measurement technique were described in Ref. 15. Briefly, the two-tint TDTR utilized a ~791 nm pump beam to heat the sample and used another time-delayed ~780 nm probe beam to monitor the reflectance change at the sample surface. The delay time was regulated by a mechanical delay line on the laser table. Since the system was in the linear response regime, measuring the reflectance change was equivalent to measuring the temperature change at the sample surface. To avoid carrier excitation in the substrate, the microfabricated metallic gratings were designed with subwavelength gaps between neighboring metal lines that prevented the pump and probe light from transmitting through the grating when the laser beams were polarized parallel to the grating [14]. We used a combination of a quarter waveplate and a linear polarizer to align the laser beams with the metallic gratings during the measurement.

The size-dependent effective thermal conductivities were extracted by matching the measured reflectance signals with the prediction from the heat-diffusion theory.

Figure 6.15b shows the measured size-dependent thermal conductivities of $Nb_{0.95}Ti_{0.05}FeSb$ (hot-pressed at 1273K) at room temperature. As shown in Figure 6.15b, the transport transitions from the near-diffusive regime to the non-diffusive regime when the heater size was systematically reduced from ~500 nm to ~100 nm, consistent with our understanding of non-diffusive thermal transport. The size-dependent thermal conductivities were utilized to approximately extract the phonon MFP distribution in $Nb_{0.95}Ti_{0.05}FeSb$ via a MFP-reconstruction algorithm that was described in detail in Ref. 15. Figure 6.15c shows the reconstructed phonon MFP spectra of $Nb_{0.95}Ti_{0.05}FeSb$ at room temperature. The dominant thermal phonon MFPs at room temperature were in the range of a few tens to a few hundreds of nanometers. In particular, phonons with MFPs shorter than 300 nm contributed approximately 70% to the total thermal conductivity. Due to increasing three-phonon scattering processes with increasing temperatures, the dominant thermal phonon MFPs were typically further suppressed at elevated temperatures. Consequently, the grain-size dependence of the thermal conductivity of $Nb_{0.95}Ti_{0.05}FeSb$ at elevated temperatures was expected to be much weaker than that at room temperature when the studied grain-sizes were larger than 0.3 μm, consistent with our experimental observation shown in Figures 6.3d-e.

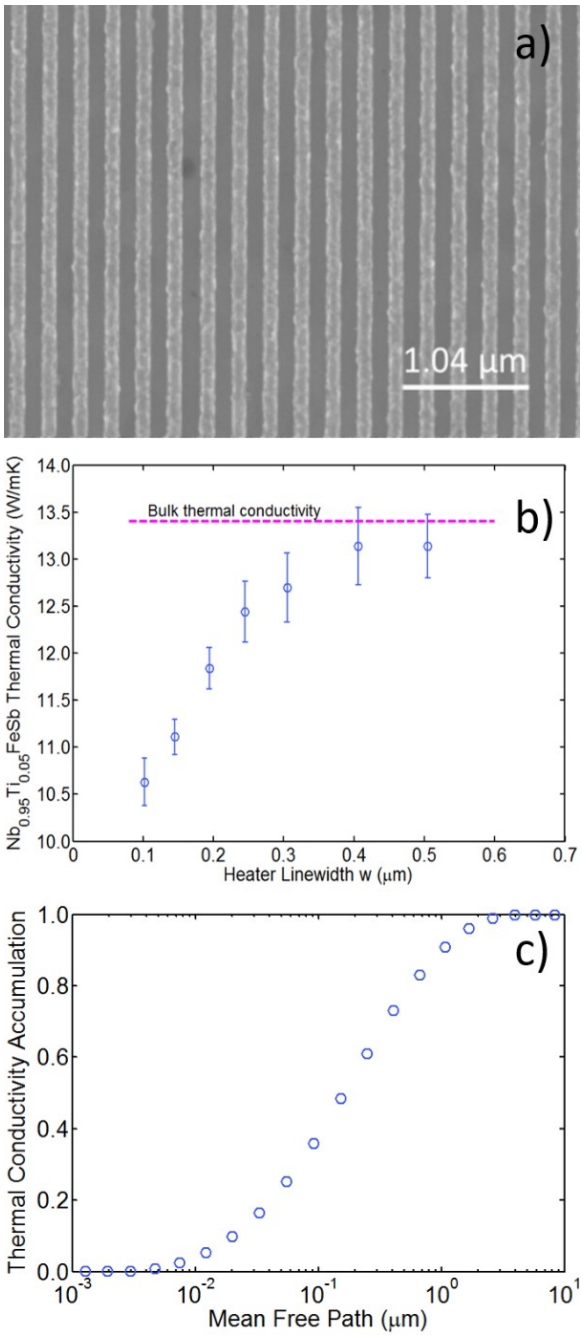

Figure 6.15 a) A representative SEM image of the micro-fabricated metallic grating on the $Nb_{0.95}Ti_{0.05}FeSb$ substrate. b) TDTR measured size-dependent $Nb_{0.95}Ti_{0.05}FeSb$ thermal conductivities at room temperature. The error bars represent the standard deviation of the measurement uncertainty. c) Reconstructed phonon MFP distribution of $Nb_{0.95}Ti_{0.05}FeSb$ at room temperature [7].

6.6 References

[1] D. Narducci, Do we really need high thermoelectric figures of merit? A critical appraisal to the power conversion efficiency of thermoelectric materials, *Appl. Phys. Lett.* **99**, 102104 (2011).

[2] H. S. Kim, *et al.*, Relationship between thermoelectric figure of merit and energy conversion efficiency, *Proc. Natl. Acad. Sci.* **112**, 8205-8210 (2015).

[3] G. Joshi, *et al.*, NbFeSb-based p-type half-Heuslers for power generation applications, *Energy Environ. Sci.* **7**, 4070-4076 (2014).

[4] C. G. Fu, *et al.*, Band engineering of high performance p-type FeNbSb based half-Heusler thermoelectric materials for figure of merit zT> 1, *Energy Environ. Sci.* **8**, 216-220 (2015).

[5] C. G. Fu, *et al.*, Realizing high figure of merit in heavy-band p-type half-Heusler thermoelectric materials, *Nat. Comm.* **6**, 8144 (2015).

[6] L. Chen, *et al.*, Uncovering high thermoelectric figure of merit in (Hf,Zr)NiSn half-Heusler alloys, *Appl. Phys. Lett.* **107**, 041902 (2015).

[7] R. He, *et al.*, Achieving high power factor and output power density in p-type half-Heuslers $Nb_{1-x}Ti_xFeSb$, *Proc. Natl. Acad. Sci.* doi: 10.1073/pnas.1617663113 (2016).

[8] D. M. Rowe, *et al.*, Electrical and thermal transport properties of intermediate-valence $YbAl_3$, *J. Phys. D: Appl. Phys.* **35**, 2183-2186 (2002).

[9] J. Mao, *et al.*, High thermoelectric power factor in Cu-Ni alloy originate from potential barrier scattering of twin boundaries, *Nano Energy* **17**, 279-289 (2015).

[10] H. Brooks, *Advances in electronics and electron physics*, Academic Press, New York (1955).

[11] H. H. Xie, *et al.*, Beneficial contribution of alloy disorder to electron and phonon transport in half-Heusler thermoelectric materials, *Adv. Energy. Mater.* **23**, 5123-5130 (2013).

[12] J. Mao, *et al.*, Carrier distribution in multi-band materials and its effect on thermoelectric properties, *Journal of Materiomics* **2**, 203–211 (2016).

[13] P. Klemens, The thermal conductivity of dielectric solids at low temperatures (theoretical), *Proc. R. Soc. A.* **208**, 108-133 (1951).

[14] Y. Hu, *et al.*, Spectral mapping of thermal conductivity through nanoscale ballistic transport, *Nat. Nanotechnol.* **10**, 701-706 (2015).

[15] L. P. Zeng, *et al.*, Measuring phonon mean-free-path distributions by probing quasiballistic phonon transport in grating nanostructures, *Sci. Rep.* **5**, 17131 (2015).

[16] L. P. Zeng, *et al.*, Disparate quasiballistic heat conduction regimes from periodic heat sources on a substrate, *J. Appl. Phys.* **116**, 064307 (2014).

[17] A. J. Hong, *et al.*, Full-scale computation for all the thermoelectric property parameters of half-Heusler compounds, *Sci. Rep.* **6**, 22778 (2016).

[18] K. Tukioka, The determination of the deformation potential constant of the conduction band in InSb by the electron mobility in the intrinsic range, *Jpn. J. Appl. Phys.* **30**, 212-217 (1991).

[19] Y. Z. Pei, *et al.*, Optimum carrier concentration in n-type PbTe thermoelectrics, *Adv. Energy. Mater.* **4**, 1400486 (2014).

[20] K. Koumoto, and T. Mori, *Thermoelectric nanomaterials*, Springer, Berlin (2013).

[21] J. Seto, The electrical properties of polycrystalline silicon films, *J. Appl. Phys.* **46**, 5247-5254 (1975).

[22] J. de Boor, *et al.*, Microstructural effects on thermoelectric efficiency: A case study on magnesium silicide, *Acta Mater.* **77**, 68-75 (2014).

[23] M. Cutler, R. L. Fitzpatrick, and J. F. Leavy, The conduction band of cerium sulfide $Ce_{3-x}S_4$, *J. Phys. Chem. Solids* **24**, 319-327 (1963).

[24] U. Walter, E. Holland-Moritz, and Z. Fisk, Kondo resonance in the neutron spectra of intermediate-valent $YbAl_3$, *Phys. Rev. B* **43**, 320-325 (1991).

[25] C. L. Foiles, Thermoelectric power of dilute Cu-Ni alloys in a magnetic field, *Phys. Rev.* **169**, 471-476 (1968).

[26] D. Kraemer, *et al.*, High thermoelectric conversion efficiency of MgAgSb-based material with hot-pressed contacts, *Energy Environ. Sci.* **8**, 1299-1308 (2015).

[27] X. Hu, *et al.*, Power generation from nanostructured PbTe-based thermoelectrics: comprehensive development from materials to modules, *Energy. Environ. Sci.* **9**, 517-529 (2016).

[28] J. R. Salvador, *et al.*, Conversion efficiency of skutterudite-based thermoelectric modules, *Phys. Chem. Chem. Phys.* **16**, 12510-12520 (2014).

[29] L. Aukerman, and R. Willardson, High-temperature Hall coefficient in GaAs, *J. Appl. Phys.* **31**, 939-940 (1960).

[30] W. S. Liu, *et al.*, New insight into the material parameter B to understand the enhanced thermoelectric performance of $Mg_2Sn_{1-x-y}Ge_xSb_y$, *Energy Environ. Sci.* **9**, 530-539 (2016).

[31] Y. L. Tang, *et al.*, Convergence of multi-valley bands as the electronic origin of high thermoelectric performance in $CoSb_3$ skutterudites, *Nat. Mater.* **14**, 1223–1228 (2015).

[32] R. He, *et al.*, Studies on mechanical properties of thermoelectric materials by nanoindentation, *Phys. Status Solidi A* **212**, 2191-2195 (2015).

[33] T. M. Tritt, *et al.*, In *Thermoelectrics, 2001. Proceedings ICT 2001. XX International Conference on.* IEEE (2001).

[34] N. Ashcroft, and N. Mermin, *Solid-state physics*, Thomson Learning (1976).

[35] P. Klemens, The scattering of low-frequency lattice waves by static imperfections, *Proc. Phys. Soc. A* **68**, 1113-1128 (1955).

[36] B. Abeles, Lattice thermal conductivity of disordered semiconductor alloys at high temperatures, *Phys. Rev.* **131**, 1906-1911 (1963).

[37] G. Slack, Thermal conductivity of MgO, Al_2O_3, $MgAl_2O_4$, and Fe_3O_4 crystals from 3 to 300 K, *Phys. Rev.* **126**, 427-441 (1962).

[38] M. Roufosse, and P. Klemens, Thermal conductivity of complex dielectric crystals, *Phys. Rev. B* **7**, 5379-5386 (1973).

[39] H. Geng, *et al.*, Lattice thermal conductivity of nanograined half-Heusler solid solutions, *Appl. Phys. Lett.* **104**, 202104 (2014).

[40] X. Shi, *et al.*, Optimized thermoelectric properties of $Mo_3Sb_{7-x}Te_x$ with significant phonon scattering by electrons, *Energy Environ. Sci.* **4**, 4086-4095 (2011).

[41] G. Rogl, *et al.*, Mechanical properties of half-Heusler alloys, *Acta Materialia*. **107**, 178-195 (2016).

[42] A. J. Minnich, *et al.*, Thermal conductivity spectroscopy technique to measure phonon mean-free-paths, *Phys. Rev. Lett.* **107**, 095901 (2011).

[43] A. J. Minnich, Determining phonon mean-free-paths from observations of quasiballistic thermal transport, *Phys. Rev. Lett.* **109**, 205901 (2012).

[44] G. Chen, Nonlocal and nonequilibrium heat conduction in the vicinity of nanoparticles, *J. Heat Transfer* **118**, 539–545 (1996).

[45] K. Kang, *et al.*, Two-tint pump-probe measurements using a femtosecond laser oscillator and sharp-edged optical filters, *Rev. Sci. Instrum.* **79**, 114901 (2008).

[46] A. J. Schmidt, X. Y. Chen, and G. Chen, Pulse accumulation, radial heat conduction, and anisotropic thermal conductivity in pump-probe transient thermoreflectance, *Rev. Sci. Instrum.* **79**, 114902 (2008).

Chapter 7 Summary

The thermoelectric (TE) effects are the coupled transport between electrons and phonons in solids. It includes three intertwined effects: the Seebeck effect that allows the generation of current from heat flow; the Peltier effect that generates a temperature gradient from electric current; and the Thomson effect that describe the heating or cooling of a conductor that simultaneously possess a current and a temperature difference. These effects have been studied extensively due to their application potentials. In this dissertation, I measured the mechanical properties of various TE materials using nanoindentation technique; then I improved the TE performances of half-Heusler compounds by suppressing the material cost, boosting the figure-of-merit (*ZT*) and the power factor.

Firstly I tested the hardness and modulus of the commonly studied thermoelectric materials using nanoindentation. The tested materials included half-Heusler, skutterudite, bismuth-telluride, silicon-germanium, and lead-selenide. To incorporate the contact-edge pile-ups, I used the AFM corrections by adding average pile-up heights to the penetration depth. The results showed that the hardness/modulus are 12.8 GPa/221 GPa, and 9.1 GPa/186 GPa, for p-type and n-type half-Heusler compounds with composition $Hf_{0.44}Zr_{0.44}Ti_{0.12}CoSb_{0.8}Sn_{0.2}$, and $Hf_{0.25}Zr_{0.75}NiSn_{0.99}Sb_{0.01}$, respectively. Admittedly, hardness and modulus are not complete design parameters for choosing TE materials due to the complexity of application environments. However, as higher hardness indicates higher resistance to deformation, and high modulus affects the fracture strength and the thermal-shock resistance of a material, we might conclude that half-Heusler ranks well above competitive materials for use in thermoelectric power generators, where the

demands for mechanical stability are equally important as the energy conversion efficiency. These results offered a first-order ranking to consider further detailed studies of these TE materials.

Next, I investigated the thermoelectric performance of nanostructured p-type half-Heusler $MCoSb_{0.8}Sb_{0.2}$ (M = Hf, Zr, and Ti) by decreasing the usage of Hf to suppress the material cost. I started from the TE properties of binary (Hf, Zr)$CoSb_{0.8}Sb_{0.2}$ system with Hf concentration less than 0.25. A peak *ZT* of ~0.85 was realized in $Hf_{0.2}Zr_{0.8}CoSb_{0.8}Sb_{0.2}$ at 700 °C. Besides, previous report showed that the peak *ZT* of the binary (Hf, Ti)$CoSb_{0.8}Sb_{0.2}$ system is ~1 at 700 °C when the composition is $Hf_{0.8}Ti_{0.2}CoSb_{0.8}Sb_{0.2}$, in which the Hf:Ti ratio is 4:1. Thus, by keeping the optimized atomic ratio of Hf:Ti=4:1, and Hf:Zr=1:4, I obtained a new composition $Hf_{0.19}Zr_{0.76}Ti_{0.05}CoSb_{0.8}Sn_{0.2}$. Comparing to the previously optimized ternary compound $Hf_{0.44}Zr_{0.44}Ti_{0.12}CoSb_{0.8}Sn_{0.2}$, the new composition I obtained possessed similar *ZT* and much less amount of Hf. As a result, the calculated specific power cost ($\$ W^{-1}$) was suppressed by 48%. This work could accelerate the large-scale applications of half-Heusler materials for waste-heat recovery.

To further decrease the material cost, I focused on finding HH compounds that are Hf-free. One interesting material is the NbCoSn-based compounds. Although the band-structure indicated promising p-type TE properties of NbCoSn, the experimental results favored the n-type properties. With 10% Sb substitution at Sn site, the peak power factor and *ZT* of ~34 $\mu W\ cm^{-1}\ K^{-2}$ and ~0.6 were obtained at 600 °C and 700 °C, respectively. The *ZT* was improved by 100% comparing to the previously reports as a result of improved phase purity. In terms of *ZT*, the NbCoSn-based n-type HH cannot compete with the

HfNiSn-based HH. However, due to the elimination of Hf, the specific power cost ($ W^{-1}) of the NbCoSn-based HH was ~68% lower than the HfNiSn-based HH.

The NbFeSb-based HH compound is another Hf-free system. Previous reports showed promising *ZT* ~1 at 973 K with Ti substitution at Nb sites. For this system I emphasized on the power factor enhancement by improving the carrier mobility. This was realized by increasing the average grain-size from 0.3 to 4.5 μm through elevating the hot-pressing temperature from 1123 to 1373 K. Larger grains were weaker in scattering charge carriers. On the other hand, the phonon transport was insensitive to the grain-sizes since the majority phonons had mean-free-path shorter than the smallest grain-size (0.3 μm) in this system. Therefore, the peak *ZT* was improved to ~1.1 at 973 K in this study. Notably, the obtained peak power factor was ~106 μW cm^{-1} K^{-2}, which is the highest comparing to all other half-Heusler compounds, and also higher than most other thermoelectric materials. The high power factor subsequently yielded a record output-power density of ~22 W cm^{-2} based upon a single-leg device operating at between 293 and 868 K. Such a high output-power density can greatly facilitate the large-scale power generation applications.